MEASUREMENT OF THE Λ_b^0 LIFETIME IN $\Lambda_b^0 \to \Lambda_c^+ \pi^-$ DECAYS

AT THE

COLLIDER DETECTOR AT FERMILAB

by

Jonathan Reid Mumford

A dissertation submitted to The Johns Hopkins University in conformity with the requirements for the degree of Doctor of Philosophy.

Baltimore, Maryland

September, 2008

Abstract

The lifetime of the Λ_b^0 baryon (consisting of *u*, *d* and *b* quarks) is the theoretically most interesting of all *b*-hadron lifetimes. The lifetime of Λ_b^0 probes our understanding of how baryons with one heavy quark are put together and how they decay. Experimentally however, measurements of the Λ_b^0 lifetime have either lacked precision or have been inconsistent with one another.

This thesis describes the measurement of Λ_b^0 lifetime in proton-antiproton collisions with center of mass energy of 1.96 TeV at Fermilab's Tevatron collider. Using $1070 \pm 60 pb^{-1}$ of data collected by the Collider Detector at Fermilab (CDF), a clean sample of about $3,000$ fully-reconstructed $\Lambda_b^0 \to \Lambda_c^+ \pi^-$ decays (with Λ_c^+ subsequently decaying via $\Lambda_c^+ \to p^+ K^- \pi^+$) is used to extract the lifetime of the Λ_b^0 baryon, which is found to be

$$c\tau(\Lambda_b^0) = 422.8 \pm 13.8(stat) \pm 8.8(syst)\mu\text{m}.$$

This is the most precise measurement of its kind, and is even better than the current world average. It also settles the recent controversy regarding the apparent inconsistency between CDF's other measurement and the rest of the world.

ABSTRACT

Author: Jonathan Reid Mumford

Advisor: Petar Maksimović

Acknowledgements

I would like to thank first my parents for their patience, love, and encouragement in all of my adventures and interests. Besides being great parents and giving me life, they have helped me to grow and have taught me to love and appreciate the world around me. Thanks to Jason, my brother, for breaking the way for me and for setting the bar high. The most thanks to my wife Jenni with all her beauties. Your encouragement, love, and support has been the life-blood for this work, and more importantly, for my general happiness. I would like to thank Petar for his continuous supply of enthusiasm and optimism in the face of discouragement. Without his help, suggestions, and pushing, this measurement would have never been made. Thanks also to Satyajit for not only sharing 085F with me but also the burden of the analysis work. I've learned to be more patient and careful from your example. I'd also like to thank Mat Martin for his realism, encouragement, and coding expertise. Thanks to Jen Pursley for her help and example. This measurement couldn't have been made without the countless people who spend many lunch-less days and sleepless nights at CDF. In particular I'd like to thank Mat Herndon for taking the time to get me started when I arrived at CDF. Thank you Rob Napora for your work in the early

days of Run II and for documenting the silicon power supplies so well. Thanks also to the Silicon SPL's under whom I had the privilege of working especially; Gino Bolla for his unique approach to life, the art of the smoke break, and for solidifying my appreciation of Jonny Cash. Steve Nahn for patiently educating me on the complicated world of the Silicon DAQ. Rainer Wallny for taking me sailing on Lake Michigan and for trusting me with the welfare of the Si DAQ. Marcel Stanitzki for the spätzle and for sharing many laughs – our bond formed early in the bore. I'd also like to thank Julia Thom and David Clark who helped to make my time in the silicon group one of the most rewarding parts of my work at CDF. I'd also like to thank Professor Bruce Barnett at Johns Hopkins, my first advisor, for sending me to Fermilab in the first place. A big thanks to my roommates while I was living in Baltimore. 2714 Maryland Avenue was "off the hook" from the get go. Marin, Michele, Dan, and Tiny you were all great roommates and all the family that I could have hoped for. To my fellow Hopkins Physics and Astronomy graduate students, thank you for making my two years at Homewood the best of my educational career. Thank you; Kyoungsoo for the late-night Papermoon dessert runs, Xuemei for Snowball and for making me learn English, Sundar for always being ready when "...at that point we should do something", Leslie for sharing the best office that I'll probably ever occupy, Adrian for spending late nights down the hall from me on the 4th floor, and James for skateboarding Baltimore with me. Finally I'd like to thank Jonas Carney, Charles Aaron, and John Kelly. You have taught me a lot about hard work. Your faith in me has made it possible for me to pursue my dream.

Dedication

To Justin and Pepito.

Contents

List of Tables

List of Figures

Chapter 1

Theoretical Motivation

The lifetime of the Λ_b^0 baryon is a topic of considerable recent interest. For years there has been a long-standing discrepancy between experimental measurements of the Λ_b^0 lifetime and theoretical predictions. This thesis describes a measurement of the Λ_b^0 lifetime that leverages a large sample of fully-reconstructed $\Lambda_b^0 \to \Lambda_c^+ \pi^-$ decays. The data were collected by the Collider Detector at Fermilab (CDF) using a Two displaced Track Trigger (TTT). The TTT produces a very clean sample that offers several times larger statistics than other triggers for the same integrated luminosity. However, because the trigger selects events based on the presence of displaced tracks, the lifetime distribution is biased. The effect of the trigger selection bias on lifetime measurements has been extensively studied [1] and is well understood. The measurement described here uses sophisticated Monte Carlo techniques to correct for the trigger bias so that the lifetime can be accurately extracted.

This thesis is organized as follows. The theoretical background and motivation for

measuring the lifetime of Λ_b^0 are presented in this Chapter. A description of the accelerator and particle detector – the experimental apparatus used for the measurement is given in Chapter 2. The general issues and formalism for the lifetime measurement are explained in Chapter 3. The data samples are described in Chapter 4. Chapter 5 describes the details of the fit that is used to extract the Λ_b^0 lifetime from the data. The result of the fit is given in Chapter 6. Chapter 7 describes the estimated systematic uncertainties for the measurement. Finally, the results are summarized and discussed in Chapter 8.

By taking advantage of a higher statistics sample and refined trigger bias corrections, this analysis is the most accurate measure of the Λ_b^0 lifetime to date, shedding light on the long standing discrepancy between the world average of the measured Λ_b^0 lifetime and its theoretical predictions.

1.1 Standard Model of Particle Physics

Before moving on to the details involved in a lifetime measurement, a brief introduction to the Standard Model of particle physics is in order. More comprehensive introductions can be found in most particle physics texts (for example, References [2] - [5]).

The Standard Model of Particle Physics is the most successful theory to date for describing fundamental particles and their interactions. According to the Standard Model, all matter is built from a small number of fundamental, $spin$[1]$= 1/2$, particles called fermions. Fermions interact via the exchange of, integral spin, gauge bosons. The fundamental

[1]Spin is a quantum number that describes the intrinsic angular momenutum of a particle.

fermions consist of only six *quarks* and six *leptons* (and their anti-particles)[2]. Fermions are grouped together in three generations with corresponding particles exhibiting similar physical properties and behavior. Table 1.1 summarizes the fermions included in the Standard Model.

1.1.1 Fundamental Particles

Leptons include three charged particles; the lightest is the familiar electron (e), followed by the muon (μ), and the heaviest, the tau (τ). Each lepton has -1 electric charge and the same spin of $1/2$.

In addition to the electrically charged leptons, there are also three neutral leptons called neutrinos (denoted by ν). First postulated by Pauli in 1930 to account for the missing energy and momentum being carried away in nuclear β-decay (*i.e.* the radioactive decay: $n \rightarrow p^+ + e^- + \bar{\nu_e}$), neutrinos weren't measured directly until 1956 by Cowan and Reines [10]. Each of the charged leptons has an associated neutrino of the same "flavor" (*i.e.* ν_e, ν_μ, and ν_τ).

In contrast to leptons, quarks all have fractional electric charges of either $+2/3$ or $-1/3$. In addition to spin and electric charge, quarks also have an extra degree of freedom that is referred to as *color* or *color charge*. Quarks come in one of three *colors*; red,

[2]In addition to matter, the Standard Model also includes antimatter. Antimatter particles are identical to matter particles in all respects save charge. For example, the antimatter version of the electron is called the positron, which has the same properties as the electron but with a charge of $+1$ (*i.e.* e^+). With the exception of the positron, antiparticles are generally denoted by a line over the particle symbol. For example the antiparticle equivalent of the bottom quark, *b*, is denoted $\bar{b}$ and pronounced "*b*-bar".

Quarks	**Symbol**	**Charge**	**Mass (MeV/c^2)**
up	u	$+\frac{2}{3}$	$1.5-3$
down	d	$-\frac{1}{3}$	$3-7$
charm	c	$+\frac{2}{3}$	$(1.25\pm0.09)\times10^3$
strange	s	$-\frac{1}{3}$	95 ± 25
top	t	$+\frac{2}{3}$	$(174\pm3.3)\times10^3$
bottom	b	$-\frac{1}{3}$	$(4.20\pm0.07)\times10^3$
Leptons			
electron	e	-1	0.511
electron neutrino	ν_e	0	$<2\times10^{-6}$
muon	μ	-1	105.7
muon neutrino	ν_μ	0	<0.19
tau	τ	-1	1776.90 ± 0.20
tau neutrino	ν_τ	0	<18.2

Table 1.1: The fundamental fermions. Charges are in units of the absolute electron charge. Masses listed are taken from Reference [8]. Because of Einstein's famous equation relating energy to mass, $E=mc^2$, particle masses are generally quoted in units of energy divided by the speed of light squared. An electron volt, eV, is the amount of energy given to an electron that is accelerated across a 1 Volt potential. 1 eV $=1.60217646\times10^{-19}$ joules. Masses are generally expressed in millions or billions of electron volts, MeV/c^2 and GeV/c^2 respectively.

Meson	**Quark Content**	**Mass (MeV$/c^2$)**
π^+	$u\bar{d}$	139.57018 ± 0.00035
K^+	$u\bar{s}$	493.677 ± 0.016
K^{*0}	$d\bar{s}$	896.00 ± 0.25
D^+	$c\bar{d}$	1869.3 ± 0.4
$D^*(2010)^+$	$c\bar{d}$	2010.0 ± 0.4
J/ψ	$c\bar{c}$	3096.916 ± 0.011
B^+	$u\bar{b}$	5279.0 ± 0.5
B^0	$d\bar{b}$	5279.4 ± 0.5
B_s^0	$s\bar{b}$	5367.5 ± 1.8

Table 1.2: Quark content of select mesons that are referenced in this text. Masses are all quoted from Reference [8].

green, and blue. The *color* of quarks is not literal, but rather a convention of labeling three color charges. The physical parallel with color comes from the fact that in light, red, green, and blue light combine to make white, or colorless, light. In the standard model, stable combinations of quarks are required to be colorless. Stable configurations consist of either three quarks of different colors (called baryons), or quark/antiquark pairs of matching color/anti-color (called mesons). Particles that are made of quarks are collectively referred to as hadrons. Tables 1.2 and 1.3 list the quark content of the mesons and baryons that are used in this text.

Baryons	**Quark Content**	**Mass (MeV/c^2)**
p	uud	938.27203 ± 0.00008
$\Delta(1232)^{++}$	uuu	1231.6
$\Lambda^0(1520)$	uds	1519.5 ± 1.0
Λ_c^+	udc	2286.46 ± 0.14
Λ_b^0	udb	5624 ± 9

Table 1.3: Quark content of select baryons that are referenced in this text. Masses are all quoted from Reference [8].

1.1.2 Interactions

In the Standard Model, interactions between fundamental fermions take place via the exchange of gague bosons. Different bosons transmit, or *mediate*, each of the four fundamental forces in nature; electromagnetism, strong nuclear, weak, and gravity. Properties of the different force carriers are summarized in Table 1.4.

The electromagnetic force is responsible for most extra-nuclear physics. It is the force responsible for binding electrons to nuclei in atoms. The electromagnetic force is mediated by a massless, spin-1, boson called the photon (γ) that couples to any particle that has an electric charge. The field theory used to compute the cross-sections for electromagnetic processes is called quantum electrodynamics (QED). QED is one of the most accurate physical theories ever constructed. Predictions agree with experimental measurements to a precision of 10^{-10}, making QED second only to special relativity (which currently is tested to 10^{-21}) in its predictive accuracy.

Force	**Boson**	J^P	**Mass (GeV/c^2)**	**Relative Strength**
Strong Nuclear	Gluon (g)	1^-	0	1
Electromagnetic	Photon (γ)	1^-	$< 6 \times 10^{-17} eV/c^2$	10^{-2}
Weak Nuclear	$W^{\pm}$	1^-	80.403 ± 0.029	10^{-7}
	Z^0	1^+	91.1876 ± 0.0021	
Gravity	Graviton	2^+	unobserved	10^{-39}

Table 1.4: The four forces in nature and their corresponding gauge bosons. The relative strength depends on the particles involved so the numbers listed in the table are approximate. The masses are quoted from Reference [8].

The strong nuclear force is responsible for binding quarks into hadrons. This force is also responsible for binding protons and neutrons inside an atom's nucleus. The strong force is mediated by massless, spin-1 bosons called gluons (g) that couple to any particle with color. The colorless leptons are un-affected by the strong force, while quarks, which have color are. In strong interactions, color charge has a role analogous to that of the electric charge in electromagnetic interactions. Unlike photons though, gluons themselves also carry color charge and couple directly to other gluons. Each gluon carries both a color and an anti-color charge. There are eight types of gluons corresponding to each of the states in a color octet[3]. The field theory used to compute strong force interactions is called quantum chromodynamics (QCD) which will be described in more detail in Section 1.3.

The weak nuclear force is responsible for nuclear β-decay. The weak nuclear force

[3]There are three possible values for the color charge; Red (R), Green (G), and Blue (B). These three colors can be combined in eight states with non-zero color. The eight possible combinations (*i.e.* gluon state vectors) are; $|R\bar{G}>$, $|R\bar{B}>$, $|G\bar{R}>$, $|G\bar{B}>$, $|B\bar{R}>$, $|B\bar{G}>$, $\frac{1}{\sqrt{2}}|R\bar{R}-G\bar{G}>$, and $\frac{1}{\sqrt{6}}|R\bar{R}+G\bar{G}-2B\bar{B}>$

is responsible for all flavor-changing (*i.e.* $\mu \rightarrow e$ or $b \rightarrow c$) interactions. The weak force is mediated by three massive bosons; W^+, W^-, and Z^0 where the superscript denotes the electric charge of each type. Since the bosons are very massive ($M_W = 80.2$GeV, $M_Z = 91.2$GeV [8]) the weak force has an extremely short range.

Gravity is by far the weakest force at sub-atomic distance scales and its effects are negligible in particle interactions. Gravity is not described by the Standard Model and is included here only for completeness. The existence of a massless, spin-2 boson called the graviton has been postulated as the mediator of the gravitational force but it has not yet been observed. Developing an effective quantum theory, or Grand Unified Theory, that includes gravity, along with the other three fundamental forces, is still one of the primary goals in modern Physics.

1.2 Feynman Diagrams

Feynman diagrams are used to represent quantum field theory calculations pictorially. This section is meant as a brief introduction to the diagrams and the interactions that they represent. More complete introductions can be found, for example, in References [2] - [5].

An example Feynman diagram is shown in Figure 1.1. In a Feynman diagram, particles are represented by lines of various type that correspond to different fundamental particles. Solid lines represent fermions and wavy or dashed lines prepresent bosons. Arrows on lines show the direction of matter flow. In Figure 1.1, time runs forward from left to right

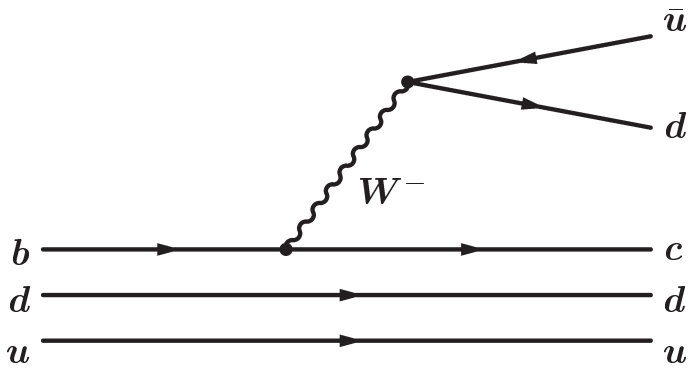

Figure 1.1: An example of a Feynman diagram. This diagram illustrates one possible mechanism for Λ_b^0 decaying to $\Lambda_c^+\pi^-$. In the decay, the bottom quark decays weakly to a W^- boson and a charm quark. W^- then decays to an anti-up and a down quark.

along the horizontal axis. Particle lines that run "backward in time" represent antiparticles moving forward in time. External lines (*i.e.* lines at the far Right and Left of the diagram) represent real, observable particles while internal lines depict particles that cannot be observed without possibly changing the process. These internal particles are said to be *virtual* particles. Points where lines connect to other lines represent interaction vertices. At each vertex, energy, momentum, and charge are conserved.

Feynman diagrams are purely symbolic and do not represent actual particle trajectories. Each diagram rather symbolizes a complicated matrix-element calculation that contributes to the amplitude for the physical process being represented. For a given interaction, an infinite number of diagrams can be drawn; and the sum of all possible Feynman diagrams gives the physical amplitude for a process. Fortunately, in the case of QED, as the diagrams become more complex (*i.e.* as the number of vertices increases) the contribution to the physical amplitude decreases and the calculations converge rapidly. Thus, by evaluating only the leading order diagrams, a good approximation for the physical amplitude can

generally be obtained.

Feynman diagrams are used in this text to illustrate how bottom quarks are produced at the Tevatron (Section 2.1). The diagrams are also used to describe interactions that contribute to lifetime differences measured in *b* hadrons (Section 1.3.2).

1.3 Quantum Chromodynamics

Quantum Chromodynamics (QCD) describes strong force interactions between colored objects, and in principle, can be used to calculate the properties of hadrons. However, unlike QED, in QCD, contributions from higher-order Feynman diagrams contribute significantly to the cross-section making the computations impossible to calculate analytically. Strong force interactions are more complicated than electromagnetic interactions because in addition to quark-quark interactions via the exchange of gluons, gluons also interact with other gluons.

In QCD, the strong interaction parameter, α_s, that quantifies the coupling of the strong force, is not a constant, but increases as a function of the distance between interacting particles. This property is known as "asymptotic freedom". At short distances (*i.e.* high energy), the strong force between two quarks is weak. As the distance between quarks increases (*i.e.* low energy), α_s increases quickly and the strong force makes it impossible to separate the quarks. This property, known as "confinement" is the mechanism that confines quarks to hadrons and makes it impossible to observe free quarks. While color-less leptons

can exist freely, quarks, because of the influence of the strong force, apparently cannot.

For short distance (high energy) interactions, quarks and gluons behave as free particles. Because α_s is small in this regime, it is possible to use a perturbative expansion in powers of α_s to calculate QCD predictions. This approach, known as perturbative QCD, has resulted in some of the most precise tests of QCD to date. However, as distances increase (energy decreases) it becomes impossible to calculate and predict QCD effects because with $\alpha_s > 1$, the calculations simply do not converge.

The QCD confinement scale, $\Lambda_{QCD} \approx 400\text{MeV}/\text{c}^2$, is the typical energy at which QCD becomes non-perturbative. The interaction of quarks in a hadron is inherently low energy – where α_s is of order unity. In this case, symmetries of QCD may be exploited to predict the properties of particle interactions. There are several methods for predicting QCD results at low energies that include; lattice QCD, $1/N$ expansions, and effective theories. Lattice QCD uses a discrete set of space-time points and heavy or light quark propagators to reduce continuum path integrals to numerical computations which can be performed on supercomputers. Such simulations are time-intensive, and each sample can take years to complete. The $1/N$, or large-N expansion, derives an expansion for QCD properties in powers of $1/N$, which is treated as a small parameter. In the limit of large N, the expansion becomes more and more accurate. In the case of QCD, where N is only 3, the higher-order terms serve as corrections to the large N limit. Effective theories also simplify QCD calculations by expanding in other small parameters. For example, chiral perturbation theories begin by assuming that the light quark masses are zero, while heavy quark effective theories assume

an infinite mass for the heavy quarks.

1.3.1 Heavy Quark Effective Theory

The QCD treatment of quark-quark interactions simplifies significantly when one of the participating quarks is much heavier than Λ_{QCD}. In this case, the momentum exchange between the heavy quark and the light *spectator* quarks is small, the recoil of the heavy quark is negligible, and the heavy quark can be treated as a static source of electromagnetic and color fields. In the limit of an infinitely heavy quark mass, the interactions of the light quarks are independent of m_Q. In reality, the mass of the heavy quark is finite, and corrections to the infinite-mass limit can be applied by expanding in powers of Λ_{QCD}/m_Q. This method for computing QCD predictions is known as a Heavy Quark Effective Theory (HQET).

Using HQET, the weak decay of the heavy quark can be treated independent of the light spectator quarks. The heavier the quark, the more appropriate the heavy quark approximation becomes and smaller lifetime differences are predicted between hadron species.

In the simple spectator model, we can write the decay width[4], Γ, for a B meson as;

$$\Gamma(b) = \frac{G_F^2 M_b^5}{192\pi^3}|V_{cb}|^2 \cdot \left[A_0 + A_1\left(\frac{\Lambda_{QCD}}{m_b}\right)^1 + A_2\left(\frac{\Lambda_{QCD}}{m_b}\right)^2 + A_3\left(\frac{\Lambda_{QCD}}{m_b}\right)^3 + \ldots\right] \quad (1.1)$$

To first order (*i.e.* $O(\Lambda_{QCD}/m_b)$), the heavy quark is a static source of color field which decays as in the spectator model, with no interaction with the cloud of light quarks and

[4]The decay width, Γ, of a particle is inversely proportional to the lifetime, τ. $\Gamma \propto 1/\tau$

gluons. At this order, the theory predicts that all *b* hadron species decay at the same rate and have the same lifetime.

Measurements confirm that the various *b* hadrons in fact decay at *different* rates. Experiments have been precise enough for some time now to clearly demonstrate that the spectator model is incomplete at $O(\Lambda_{QCD}/m_b)$. Measurements show that *B* lifetimes follow the general lifetime hierarchy of

$$\tau(B^+) > \tau(B^0) \sim \tau(B_s^0) > \tau(\Lambda_b^0) >> \tau(B_c) \tag{1.2}$$

Because of their lighter mass, charm hadrons exhibit even greater deviations from the simple spectator quark model. Lifetime ratios for several charm and bottom hadrons are listed in Table 1.5. In order to make more accurate lifetime predictions, Equation 1.1 must be calculated beyond the leading order.

Precise lifetime and mass measurements in *B* decays are the most powerful way to constrain QCD predictions. This is the essence of the measurement described in this thesis; a more accurate measure of $\tau(\Lambda_b^0)$ will help constrain the QCD effects that can obscure or confuse indirect searches for physics beyond the Standard Model. It is increasingly more important to understand non-perturbative QCD contributions as the search for physics beyond the Standard Model continues. Without a trustworthy model of QCD effects at low energies, it is difficult to identify effects that are beyond the predictions of the Standard Model.

Lifetime ratio	**Theory**	**Prediction**	**Measurement**
$\frac{\tau(D^+)}{\tau(D^0)}$	Pauli Interference dominant	~ 2	2.536 ± 0.019
$\frac{\tau(D_s^+)}{\tau(D^0)}$	without Weak Annihilation	$1.0 - 1.07$	
$\frac{\tau(D_s^+)}{\tau(D^0)}$	with Weak Annihilation	$0.9 - 1.3$	1.219 ± 0.018
$\frac{\tau(D_s^+)}{\tau(D^0)}$	QCD sum rules	1.08 ± 0.04	
$\frac{\tau(\Lambda_c^+)}{\tau(D^0)}$	quark model matrix elements	~ 0.5	0.488 ± 0.015
$\frac{\tau(B^+)}{\tau(B^0)}$	Pauli Interference in $\tau(B^+)$	1 ± 0.05	1.071 ± 0.009
$\frac{\tau(B_s^0)}{\tau(B^0)}$	QCD $1/m_b$ expansion	$1.0 \pm O(0.01)$	0.961 ± 0.019
$\frac{\tau(\Lambda_b^0)}{\tau(B^0)}$	QCD $1/m_b$ expansion	0.95 ± 0.05	0.904 ± 0.032

Table 1.5: Lifetime ratios of charm and bottom hadrons. The theoretical predictions are quoted from Reference [14] while the experimental lifetime ratios are calculated or quoted from Reference [17]. Pauli Interference and Weak Annihilation are described in detail in Section 1.3.2.

1.3.2 The Origin of Lifetime Differences

Lifetime differences between b hadrons manifest themselves only when Equation 1.1 is calculated using $O(\Lambda_{QCD}/m_b)^2$ and higher order corrections. At $O(\Lambda_{QCD}/m_b)^2$, the Fermi motion of the b quark and interactions between its spin and that of the light degrees of freedom enter. Lifetime differences between mesons and baryons appear at this order. Baryons, surrounded by two light quarks in a spin 0 cloud, decay more quickly than mesons that interact with a spin $1/2$ antiquark cloud. As a result, baryon lifetimes are predicted to be about 2% shorter than that of the mesons [11].

At $O(\Lambda_{QCD}/m_b)^3$, diagrams involving spectator quark interactions appear. Several mechanisms are responsible for the lifetime differences at this order, namely; Pauli Interference (PI), Weak Annihilation (WA), and for baryons, Weak Exchange or Scattering (WE). Although suppressed by an additional power of $1/m_b$, these effects dominate the differences in lifetimes because of a favorable phase-space factor [12].

A diagram illustrating Pauli Interference in $\Lambda_b^0 \to \Lambda_c^+ \pi^-$ is shown in Figure 1.2. There are two mechanisms for the decay; internal and external emmission of a W. The two final states are indistinguishable, resulting in quantum mechanical interference in the calculation of the decay rate. The destructive interference, caused by PI is believed to prolong Λ_b^0 lifetime, relative to B^0 by as much as 3%. Pauli Interference is also believed to be the dominant mechanism behind the $D^+ - D^0$ lifetime difference [14].

Weak Annihilation, is shown for the case of B^- in Figure 1.3. In Weak Annihilation, the constituent quarks of a meson annihilate to form a virtual W. In the case of a B^-, with

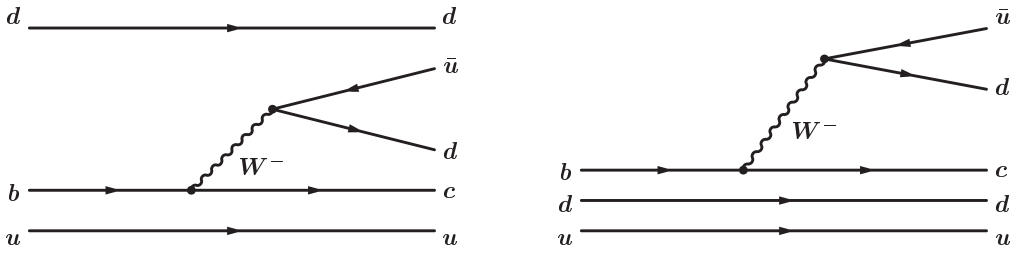

Figure 1.2: Diagram illustrating Pauli Interference. The diagrams show $\Lambda_b^0 \to \Lambda_c^+ \pi^-$ decays via two different mechanisms. The two final states are indistinguishable which results in quantum mechanical interferencewhen calculating the decay rate.

constituent quarks $b\bar{u}$, the amplitude is proportional to V_{ub}, so the effect is expected to be very small. Many interactions in the Standard Model are described by a 3×3 matrix called the Cabibbo-Kobayashi-Maskawa (CKM) matrix. The elements of the matrix are external parameters of the Standard Model that must be measured. The CKM matrix can be written as;

$$V_{CKM} = \begin{pmatrix} V_{ud} & V_{us} & V_{ub} \\ V_{cd} & V_{cs} & V_{cb} \\ V_{td} & V_{ts} & V_{tb} \end{pmatrix},$$

where the elements of the matrix describe the coupling between various quark transitions. For example, a vertex where a b quark decays to a W^- and a c quark is proportional to V_{cb}. Similarly the vertex at which a c quark decays to a W^+ and s quark is proportional to V_{cs}^* [15]. For reference, the measured values of the matrix elements [8] are;

$$V_{CKM} = \begin{pmatrix} 0.97377 \pm 0.00027 & 0.2257 \pm 0.0021 & (4.31 \pm 0.30) \times 10^{-3} \\ 0.230 \pm 0.011 & 0.957 \pm 0.017 \pm 0.093 & (41.6 \pm 0.6) \times 10^{-3} \\ (7.4 \pm 0.8) \times 10^{-3} & (40.6 \pm 2.7) \times 10^{-3} & > 0.78 \end{pmatrix}.$$

Weak Annihilation only affects the lifetime of mesons, so the Λ_b^0 lifetime is not altered

by this mechanism. The effect of WA is larger in the charm system, where it contributes to decays of D^+, but not D^0 because the weak interaction does not couple c to u in the constituent $c\bar{u}$ quarks of D^0.

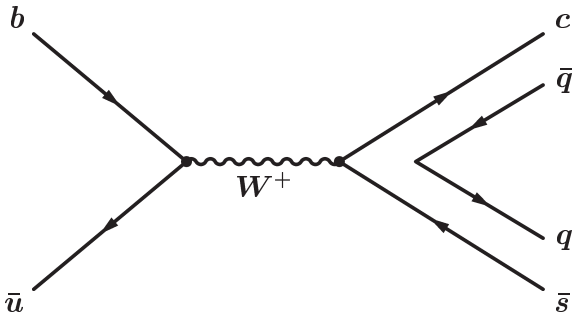

Figure 1.3: Diagram illustrating Weak Annihilation.

Weak Exchange, or Weak Scattering, is shown for $B^0 \to D^+\pi^-$ and $\Lambda_b^0 \to \Lambda_c^+\pi^-$ in Figure 1.6. Because this process is *helicity-suppressed* in Mesons, but is not in baryons, it is expected to be the mechanism most responsible for a shorter Λ_b^0 lifetime compared to B^0. Helicity is the spin projection on the momentum of a particle and is defined as $H = \frac{1}{2}\hat{\sigma}\cdot\hat{p}$. A process is said to be helicity-suppressed when, because of spin alignment, the decay is not favored quantum mechanically. It is believed that WS shortens the Λ_b^0 lifetime by as much as 7.5%. Helicity suppression of W exchange is present in pseudoscalar mesons for the same reason that the decay $\pi \to e\nu$ is suppressed. The helicity assignments of $V-A$ interaction are left-handed for particles and right handed for antiparticles. Left-handed helicity, or a helicity of $-1/2$ occurs when the spin and momentum vectors are in opposite directions. Right-handed helicity, refers to the situation when both the spin and momentum vectors are in the same direction. For weak exchange in a B^0, B^0 decays to c and $\bar{u}$ as

shown in Figure 1.6. A cartoon illustrating the desired helicity configuration for the decay of a spin-0 particle is shown in Figure 1.4. This conflicts with the configuration where the W couples to a left-handed c quark and a right-handed u quark, since both particles must be left-handed for the spins to add correctly. Meson decays then are said to be helicity suppressed. In contrast, Figure 1.5 illustrates the favored helicity configuration in Λ_b^0 decays.

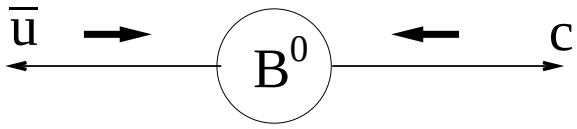

Figure 1.4: A cartoon illustrating Helicity suppression in B^0 decays. The direction of the $\bar{u}$ and c quark momentum is given by the narrow arrows. The bold arrows above the momentum lines represent the spin direction. The spin-0 B^0 is shown decaying at rest. For spin to be conserved, both the quark and anti-quark are required to have left-handed spins, this configuration is disfavored by the W coupling and the decay is said to be *helicity suppressed*.

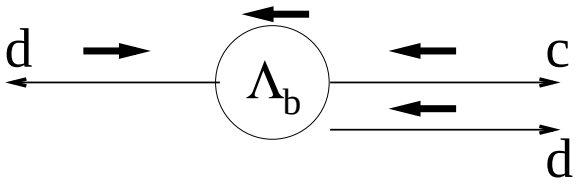

Figure 1.5: A cartoon illustrating the favorable helicity configuration in Λ_b^0 decays. Again the quark direction is indicated with the narrow arrows while the bold arrows represent the spin direction. The spin-$1/2$ Λ_b^0 is shown decaying at rest. For spin to be conserved all of the decay products are required to have left-handed spins. This configuration is favored by W coupling and the decay is not suppressed.

Recently, sub-leading spectator effects that appear at $O(\Lambda_{QCD}/m_b)^4$ in the HQET, have been included in the calculation of B lifetime ratios. The theoretical predictions for the

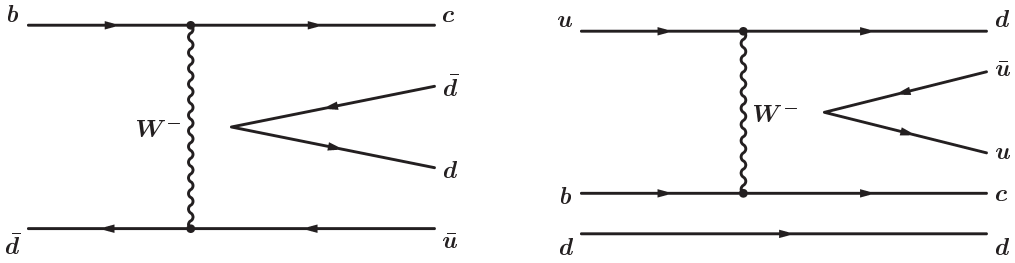

Figure 1.6: Diagrams illustrating Weak Exchange for $B^0 \to D^+\pi^-$ and $\Lambda_b^0 \to \Lambda_c^+\pi^-$ decays.

lifetime ratios thus calculated are [7];

$$\begin{aligned} \frac{\tau(B^+)}{\tau(B_d)} &= 1.06 \pm 0.02 \\ \frac{\tau(B_s)}{\tau(B_d)} &= 1.00 \pm 0.01 \\ \frac{\tau(\Lambda_b^0)}{\tau(B_d)} &= 0.88 \pm 0.05 \end{aligned}$$

The ratio $\tau(\Lambda_b^0)/\tau(B^0)$ has been the source of theoretical scrutiny since early calculations predicted a value larger than 0.90, almost 2σ higher than the world experimental average at that time. However most of the theoretical predications of the lifetime ratio center around 0.94 [16]. Some theorists believe that the lowest value of the lifetime ratio that can be accommodated in the context of the HQET corresponds to a ratio of 0.88. A larger deviation than this would imply a failure of the conventional, QCD description of hadrons and require a new paradigm for describing baryonic structure.

The experimental world-average for $\tau(\Lambda_b^0)$ in 2007, and the values that contribute to that average, are shown in Figure 1.7. Assuming a value of $\tau(B^0) = 1.530 \pm 0.009$ps [17], the values of $\tau(\Lambda_b^0)$ that correspond to a lifetime ratio of 0.88 and 0.94 are 1.346 and 1.438ps

respectively. For several years, experiments reported $\tau(\Lambda_b^0)$ lower than those predicted by theory. In late 2006, CDF reported a value that was as much as 2σ higher than the experimental world average [9].

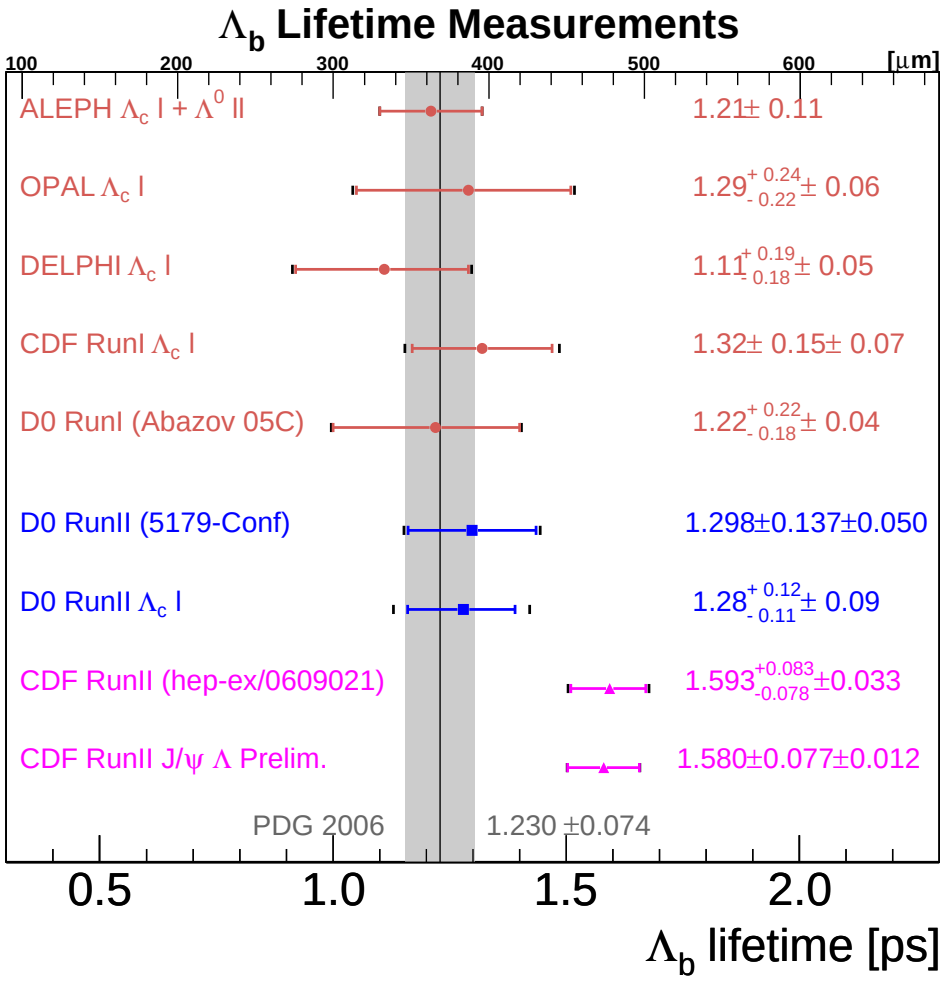

Figure 1.7: A summary of recent Λ_b^0 measurements compared to the world average [8]. Recent CDF measurements suggest a longer Λ_b^0 lifetime than has previously been measured.

On the quark level, there exists a single lifetime for a *b* quark. Differences in the lifetimes of weakly decaying B hadrons, thus provide a powerful yardstick for evaluating the impact of QCD hadronization. B decays offer a nice labratory for studying QCD. By

more accurately measuring $\tau(\Lambda_b^0)$, theorists can use the result to constrain nonperturbative QCD effects to provide a better model of hadronic behavior. Better hadronic models will help to identify physics effects beyond the predictions of the Standard Model in the future.

Chapter 2

Experimental Setup

In order to measure the lifetime of Λ_b^0 a large sample of the particles is required. Λ_b^0 baryons are not commonly found in nature; they are heavy particles that rapidly decay into lower-energy particle states. To produce the baryons one needs a high-energy particle accelerator like Fermilab's Tevatron. To measure Λ_b^0 decays, one needs a sophisticated particle detector like the Collider Detector at Fermilab (CDF). Descriptions of both the accelerator and detector are given in this chapter. More detailed descriptions of the Tevatron and CDF can be found in References [19] and [20] respectively.

2.1 $b\bar{b}$ Production at the Tevatron

The simple model of a proton is of three quarks (two *u* and one *d*) bound together by the strong force. However, as described in Section 1.3, the real picture is more compli-

cated. Hadrons are composed of three classes of partons: valence quarks – the constituent quarks of the hadron; virtual gluons; and sea quarks – quark-antiquark pairs produced by virtual gluons. All of these pieces, collectively referred to as "partons", carry part of the total energy and momentum. The hadron momentum is not distributed equally among all partons. Measured parton distribution functions, $f_i^a(x)$ give the probability that parton i carries a fraction x of the total momentum of the hadron a.

At the Tevatron, protons and antiprotons collide with a center of mass energy of $\sqrt{s} = 1.96 TeV$. At these energies, the collision time and distance between partons is so short that they may be treated as free particles – this property of QCD is referred to as asymptotic freedom as described in Section 1.3. In this case perturbative QCD and the parton distribution functions may be used to determine the possible interactions. Very rarely is the entire momentum of the proton and the antiproton involved in a collision. More commonly, only one parton from the proton and one from the antiproton will interact, via the exchange of virtual bosons.

There are many ways in which a $b\bar{b}$ pair can be produced. Figure 2.1 shows the lowest, or leading order, QCD production mechanisms. The leading order mechanisms are those with the fewest possible number of quark-gluon or gluon-gluon interactions. In leading order production, the $b\bar{b}$ pair are the only outgoing products so they move away from each other with equal and opposite momenta in the center-of-mass frame. The leading order production dominates for $q\bar{q}$ pairs when the quark mass m_q is comparable to, or larger than, the average momentum carried by the partons. At Tevatron energies, this is only true

of $t\bar{t}$ production. For $b\bar{b}$ production, next-to-leading order production mechanisms, such as those shown in Figure 2.2 also play a significant role. Each of these mechanisms has an additional quark-gluon or gluon-gluon connection than the leading order mechanisms, resulting in a final state with a $b\bar{b}$ pair and a gluon. The gluon may take a significant portion of the energy.

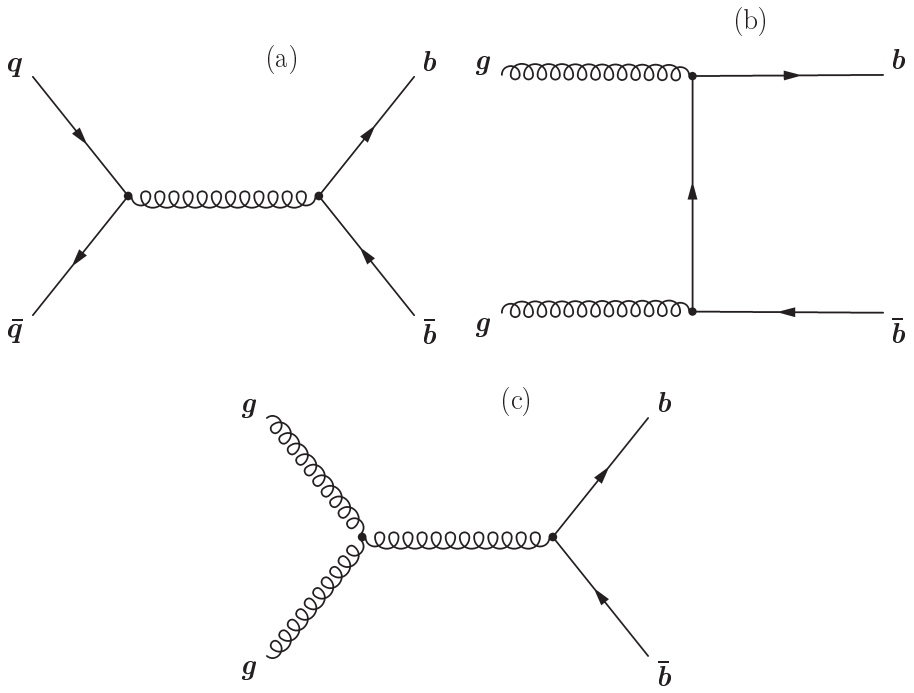

Figure 2.1: Feynman diagrams of the leading order $b\bar{b}$ production mechanisms. Diagram (a) shows flavor creation through quark annihilation where q can be any quark flavor. Diagrams (b) and (c) are both examples of flavor creation from gluon fusion.

As described in Section 1.3, confinement keeps quarks and gluons bound in hadrons. After a $b\bar{b}$ pair is produced, the strong force organizes the quarks and gluons into colorless hadrons. This process is usually achieved by the creation of additional $q\bar{q}$ pairs from the vacuum in a process called *fragmentation* or *hadronization*. For high energy gluons or b quarks, many fragmentation particles may be produced, leading to a collimated "jet"

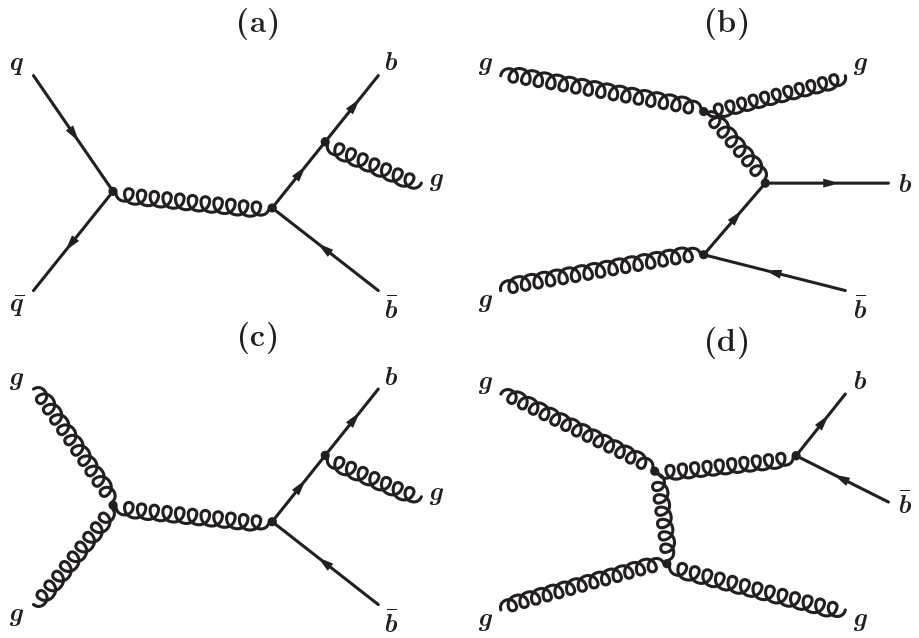

Figure 2.2: Feynman diagrams of the next to leading order $b\bar{b}$ production mechanisms; each of these processes have an additional final state gluon and three vertices. Diagrams (a) and (c) are both examples of flavor creation. Diagram (b) is an example of *b* production through flavor excitation. Diagram (d) illustrates an interaction called gluon splitting.

of hadrons whose total energy is equal to the energy of the initial quark or gluon. The fractions f_u , f_d , f_s , f_c, and $f_{\Lambda_b^0}$ give the likelihood for a *b*-quark to first produce a $u\bar{u}$, $d\bar{d}$, $s\bar{s}$, $c\bar{c}$, or diquark-antidiquark pair respectively. Depending on the $q\bar{q}$ produced, the *b* quark will hadronize into a B^+, B^0, B_s^0, or Λ_b^0. The B_c is produced so rarely that the production fraction f_c has not yet been measured. The fractions $f_u \approx f_d$ have been measured at both e^+e^- and $p\bar{p}$ colliders to be about $39.8 \pm 1.0\%$. A recent CDF measurement of the relative

production fractions [18] finds;

$$\begin{aligned}
\frac{f_u}{f_d} &= 1.054 \pm 0.018(stat.)^{+0.025}_{-0.045}(syst.) \pm 0.082(BR) \\
\frac{f_s}{f_u + f_d} &= 0.160 \pm 0.005(stat.)^{+0.011}_{-0.010}(syst.)^{+0.057}_{-0.034}(BR) \\
\frac{f_{\Lambda_b^0}}{f_u + f_d} &= 0.281 \pm 0.012(stat.)^{+0.058}_{-0.056}(syst.)^{+0.128}_{-0.086}(BR).
\end{aligned}$$

The three errors on each measurement are due to statistical fluctuations (stat.), systematic uncertainties (syst.), and uncertainties due to measurements of the branching ratios on the decays of the given hadrons (BR). Using these numbers, b hadrons will be produced in the following ratio; $B^+ : B^0 : B_s^0 : \Lambda_b^0 = 36 : 34 : 11 : 19$.

2.1.1 Topology of a $b\bar{b}$ Collision

When two partons interact to produce a $b\bar{b}$ quark pair and possibly also a gluon, the two b quarks and the gluon fragment to produce other hadrons. The remnants of the original proton and antiproton also hadronize to form other colorless states, producing more hadrons that are not related to the b quark production. These hadrons are collectively referred to as the *underlying event*. In addition, there may be more than one $p\bar{p}$ collision in a bunch crossing. At the very highest luminosities, there may be as many as 5-10 $p\bar{p}$ interactions per crossing. Since the proton and antiproton bunches in the Tevatron are quite long (about 30 cm) multiple $p\bar{p}$ interactions are typically far enough apart that they can be distinguished. Background hadrons from other $p\bar{p}$ collisions are referred to as a "pile-up event". The topology of a $b\bar{b}$ event at CDF is shown in Figure 2.3. An event display from

an actual event is shown in Figure 2.4. The cylindrical symmetry of $p\bar{p}$ collisions motivate the design of the CDF detector as described in Section 2.3. Concentric layers of tracking detectors are used to track charged particles as they travel through CDF.

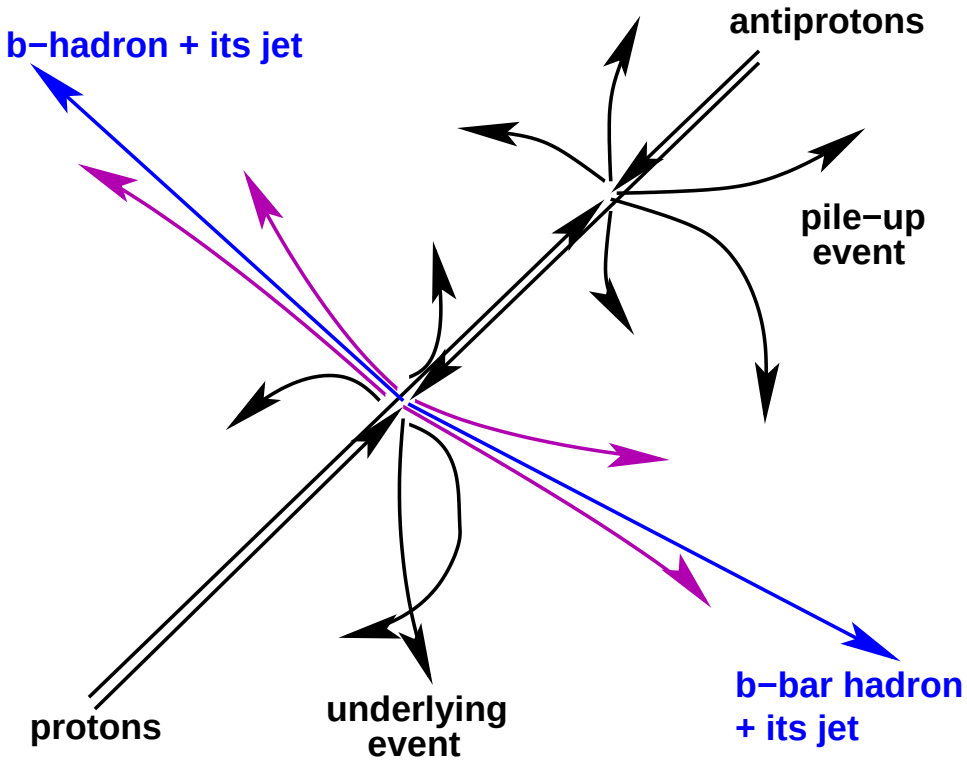

Figure 2.3: Cartoon of a typical $b\bar{b}$ collision at CDF.

2.2 The Accelerator

Fermilab's Tevatron accelerates bunches of protons and antiprotons each to 980 GeV. An electron volt (eV) is the amount of energy given to an electron that is accelerated by a voltage difference of 1 Volt and is equivalent to $1.60217646 \times 10^{-19}$ joules. The particles

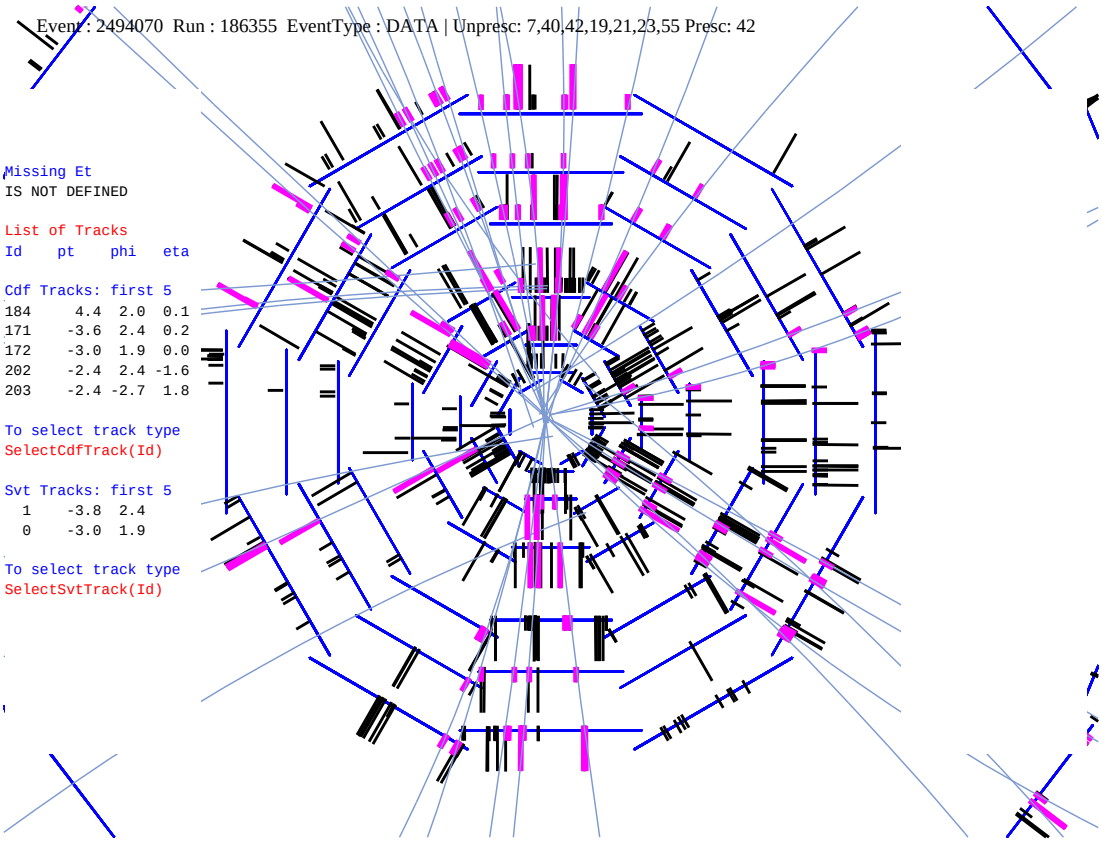

Figure 2.4: An event display from an actual collision event at CDF. The display shows the *xy*-plane (with the Tevatron beam going into the page). Layers of the silicon tracking detector are shown as dark blue lines that encircle the collision point. Most of the tracks originate from a single point called the Primary Vertex (PV). Other tracks are displaced from the PV. Some of these displaced tracks are from the decay of long-lived particles (*e.g.* Λ_b^0) that are created at the PV and travel some distance before decaying.

collide with a center of mass energy of 1.96 TeV. The initial Run II integrated luminosity goal was 2 inverse-femtobarns (fb^{-1}) with a long-term (Run IIb) goal of as much as $8\,fb^{-1}$. A barn[1] is a unit for measuring particle cross-sections. 1 barn equals $10^{-24}cm^2$. In the Spring of 2008, the Tevatron has achieved a record instantaneous luminosity of $2.92 \times 10^{32}cm^{-2}s^{-1}$.

[1]Physicists developed the term "barn" during World War II while scattering neutrons off of uranium nuclei, which were described as being as "big as a barn." One femto-barn (fb) is equal to 10^{-15} barns.

Luminosity is a measure of particle interaction, specifically the chance that a proton will collide with an antiproton. The higher the luminosity, the greater the chance of quark production. Luminosity is given by;

$$L = \frac{fBN_pN_{\bar{p}}}{2\pi(\sigma_p^2 + \sigma_{\bar{p}}^2)} F\left(\frac{\sigma_l}{\beta^*}\right), \tag{2.1}$$

where f is the revolution frequency, B is the number of bunches, and N_p ($N_{\bar{p}}$) is the number of protons (antiprotons) per bunch (typically 3×10^{11} for protons and 3×10^{10} for antiprotons). σ_p and $\sigma_{\bar{p}}$ denote the rms beam sizes at the point of interaction. F is a form factor that depends on the ratio of σ_l, the bunch length, and β^*, the beta function, at the interaction point. The beta function is a measure of the beam width, and is proportional to the *x* and *y* dimensions of the beam. The limiting factor for achieving high luminosity is the number of available antiprotons.

Fermilab uses a series of sequential accelerators to create the worlds highest energy beam of protons. Figure 2.5 gives a schematic representation of the accelerators in the Tevatron chain. The Cockcroft-Walton pre-accelerator provides the first stage of acceleration by creating H^-, hydrogen gas ions, consisting of two electrons and one proton. The ions are accelerated by a positive voltage and reach an energy of 750,000 electron volts (750 keV). The ions next enter a linear accelerator (Linac) that is approximately 500 feet long. Oscillating electric fields accelerate the ions to 400 million electron volts (400 MeV). Before entering the next accelerator stage, the ions are passed through a thin carbon foil to strip the electrons and leave only the positively charged protons. At this point, the protons enter the Booster; a circular, synchrotron accelerator that uses magnets to bend the beam

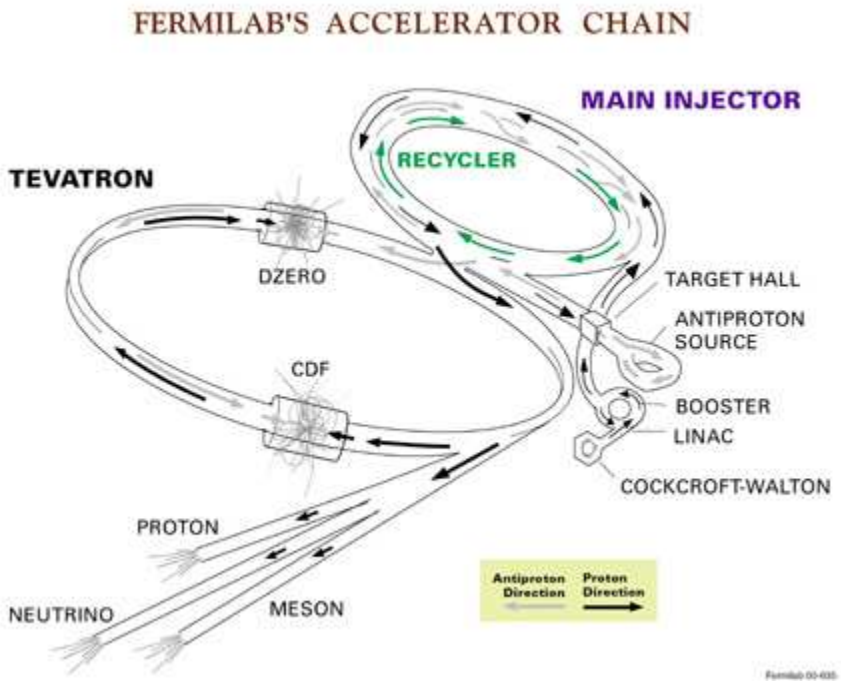

Figure 2.5: Schematic view of the elements in the Tevatron accelerator chain.

of protons in a circular path. The protons travel around the Booster about 20,000 times, repeatedly experiencing electric fields that accelerate the particles. The protons exit the Booster with an energy of 8 billion electron volts (8GeV) [21].

The next phase of acceleration takes place in the Main Injector where protons accelerate from 8GeV to 150GeV before they are injected into the Tevatron. Additionally, high-energy protons from the Main Injector are used to make antiprotons.

To produce antiprotons, the Main Injector sends 120GeV protons to the Antiproton Source, where the protons collide with a nickel target. The collisions produce a wide range of secondary particles that include antiprotons. The secondary particles are focused using a lithium lens and antiprotons are filtered using a pulsed magnet. Roughly one antiproton

is created, and successfully captured, for every 500,000 incident protons. Upon creation, antiprotons are stored in the Accumulator until a sufficient number (about $(80-200)\times 10^{10}$) have been collected, at which point, they are sent to the Main Injector, where they too are accelerated to 150GeV.

The Main Injector shares its tunnel with a recent Tevatron upgrade called the Antiproton Recycler. The Recycler was originally designed to store un-collided antiprotons that return from the Tevatron. The Recycler has never been used this way but now serves as an 8GeV antiproton storage ring between Tevatron collider stores. The Recycler reduces the time required to accumulate a sufficient antiproton store for Tevatron collisions.

The final accelerator in the chain is called the Tevatron which is a circular ring with a radius of one kilometer. The Tevatron receives 150GeV protons and antiprotons from the Main Injector and accelerates them to 980 GeV(or nearly one Tera electron volt (1 TeV) hence the name "Tevatron"). At this energy, the protons and antiprotons travel just 200 miles per hour below the speed of light. 36 bunches (or clouds) of positively charged protons, and 36 bunches of negatively charged antiprotons, circle through the Tevatron in opposite directions. Each particle bunch is about 1 meter long with a circular width of a few millimeters. Particle bunches are focused, and made to collide at two places on the Tevatron ring; at the centers of the 5000-ton CDF and D0 detectors. To achieve high luminosity at the two detector sites, the particle bunches are are focused, or "squeezed" by superconducting quadrapole magnets called Low Beta magnets, to a width of approximately 35μm and collided.

2.3 The Collider Detector at Fermilab

The Collider Detector at Fermilab (CDF) is a general purpose, solenoidal detector capable of precision charged particle tracking, fast projective calorimetry, and fine grained muon detection. The detector has been designed to make precision QCD, electroweak, and heavy flavor physics measurements as well as search for exotic, new particles and new physics. The experiment is run by a multi-national collaboration of over 800 physicists from more than 50 participating institutions. A cartoon of the CDF detector is shown in Figure 2.6.

The detector was designed to be nearly cylindrically symmetric around the beam and symmetric front to back with respect to the nominal beam interaction point. The tracking systems are located within a super-conducting solenoid magnet that provides a 1.4 Tesla field in the direction of the beam. The momentum and charge of tracked particles can be determined by their deflection in the magnetic field. A Time-of-Flight (TOF) system is located directly outside (radially) of the tracking system. TOF information is combined with momentum information from the tracking system to aid in particle identification. The calorimeter systems are located outside the solenoidal magnet and are used to measure electron and photon energies, jet energies, and net transverse energy flow. Calorimeter systems are also used to identify electrons and photons. Muon detection systems are located on the exterior of the detector and are used for triggering and for identifying particles as muons.

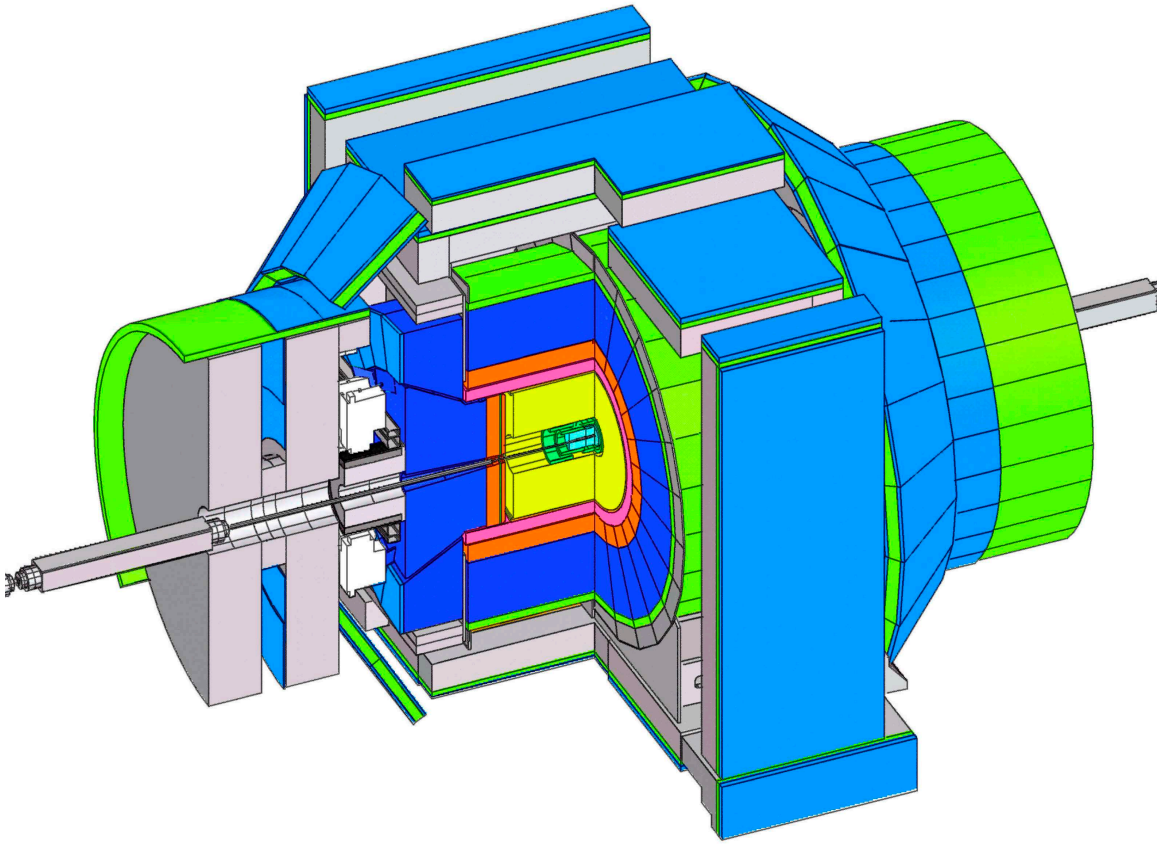

Figure 2.6: Three dimensional diagram of the CDF detector. The Tevatron beam-pipe is shown running through the center of the detector. The innermost detector, shown in light blue and green, is the silicon tracking system. The COT, shown in yellow, is surrounded by a cylindrical magnet, shown in pink. The electromagnetic and hadronic calorimeters are shown in orange and dark blue respectively. The outermost detectors, shown in green and light blue are the muon detectors. The detector is about 12 meters tall and 20 meters long.

2.3.1 From Detector Hits to Particle Tracks

Efficient and precise charged particle tracking is critical for most of the measurements done at CDF. The tracking system reconstructs charged particle trajectories that traverse the tracking volume. The tracking system is comprised of a drift chamber, called the Central Outer Tracker (COT), and a silicon based tracking system comprised of three sub-detectors; The inner-most Layer Zero Zero (L00), the Silicon Vertex Detector for Run II (SVX II),

and the Intermediate Silicon Layers (ISL). All of the tracking systems are enclosed by a superconducting, 1.4T, solenoidal magnet that is 2.8m in diameter and 3.5m long. Figure 2.7 is a cartoon of the tracking systems.

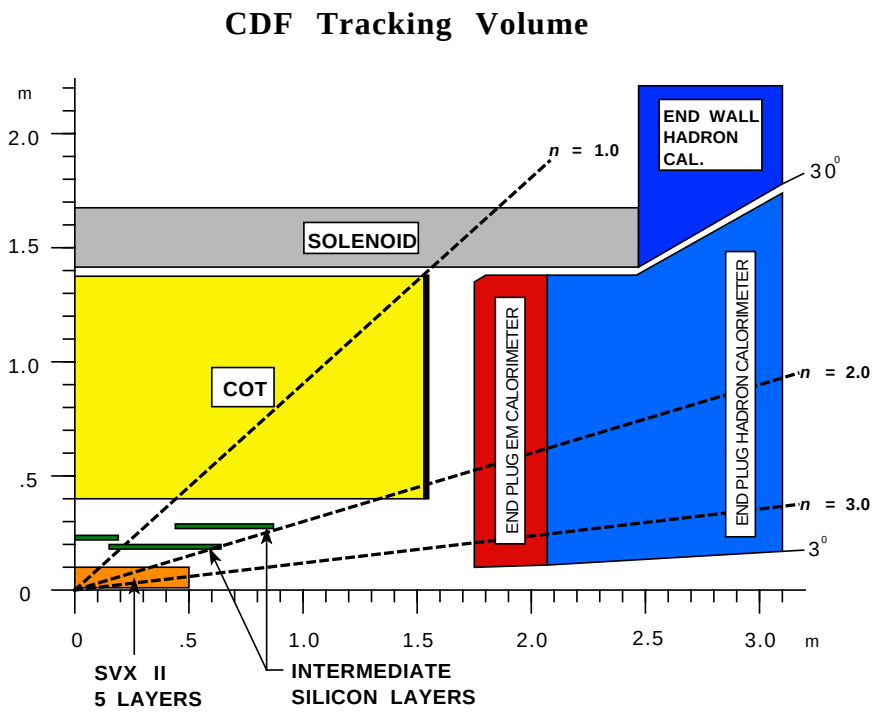

Figure 2.7: Tracking systems of CDF

In a uniform magnetic field, like the one produced by the CDF solenoid, the trajectories of charged particles are bent to form a helix. The curvature of the helix depends on the electric charge of the particle and is inversely proportional to the particle's momentum.

Before describing each of the tracking systems in detail, it may be useful to first describe how information from each system is combined to form tracks.

2.3.1.1 Definition of Common Tracking Variables

There are two commonly used coordinate systems used at CDF. A Cartesian coordinate system (x,y,z) where the origin is located at the center of the beam pipe in the center of the detector. The positive *z*-axis is along the beam in the direction of proton motion. The positive *x*-axis points toward the outside of the Tevatron ring. The positive *y*-axis points straight up, perpendicular to the Tevatron ring. The second coordinate system that is commonly used is a polar coordinate system (r,θ,ϕ) where *r* is the distance from the beam, θ is the polar angle made with respect to the *z*-axis and ϕ is the azimuthal angle.

Five track parameters are used at CDF to describe the helical trajectory of a charged particle [22];

- d_0: The signed impact parameter of the track, defined as the distance of closest approach to the beam..
- z_0: The *z*-position of the track at its point of closest approach to the beam.
- C: The half-curvature of the track, $C = \frac{1}{2\rho}$ where ρ is the radius of the circle made by projecting the track trajectory on the *xy*-plane.
- ϕ_0: The azimuthal angle of the track at the point of closest approach to the beam.
- $cot\theta$: The co-tangent of the polar angle, θ, of the track the point of closest approach to the beam. Sometimes denoted as λ.

Other variables that are often used at CDF (and in many other high-energy collider

experiments) are;

- $\eta = -ln\left[tan\left(\frac{\theta}{2}\right)\right]$: where θ is the polar angle. η is known as pseudorapidity.
- $E_T = E \cdot sin\theta$: Transverse energy.
- $p_T = p \cdot sin\theta$: Transverse momentum (component of the particle's momentum projected onto the transverse plane).
- L_{xy}: The distance a particle travels in the transverse plane from the primary vertex before decaying.
- $ct = \frac{L_{xy} \cdot mc}{p_T}$: ct is the proper decay length of a particle. m is the particle mass and c is the speed of light.

2.3.1.2 Reconstructing Tracks

Tracks are reconstructed using data taken by the COT and silicon tracking systems. Because the COT is at a larger radius from the interaction, the track density there is lower than in the silicon. Track reconstruction generally begins by looking for clusters of hits in the COT. Hits from different COT superlayers are linked into straight segments, and the segments are joined into tracks. Tracking in the silicon is done using COT tracks as seeds. A tracking "window" is defined using the point of a COT track's intersection with the outermost layer of silicon. All silicon hit clusters within the window are attached to track seeds one at a time; the track is then refit using the updated hit information. The track fit for each layer of silicon is used to define a new tracking window for the next layer of silicon.

This process continues until all silicon layers have been searched. It is possible to have multiple silicon tracks from a single COT track seed if more than one valid combination of silicon hits is found. The best track is chosen based on the χ^2 of the track fit and the number of attached silicon hits. This algorithm is referred to as "Outside-In" (OI) tracking.

After the OI tracking algorithm is run, some unattached silicon hits may remain. A stand-alone silicon tracking algorithm has been developed to reconstruct tracks using only these unattached hits. This algorithm is particularly useful in the forward region of CDF where there is no COT coverage.

2.3.1.3 Track Refitting

Tracks reconstructed from detector information are not ready to be used in an analysis until a couple of important corrections are applied. First, Multiple Coulomb Scattering (MCS) in the COT volume must be considered. MCS is a statistical description of the scattering angle of a particle as a result of many small interactions with atomic nuclei. MCS has the highest impact on particles with low energy. For reconstructed COT tracks, ignoring MCS results in underestimated track parameter errors. As a correction, the elements of the track covariance matrix are rescaled using the prescription given in Reference [23].

Second, the energy loss of a particle due to interactions with both the active and passive materials in the detector must be accounted for. As a particle loses energy its momentum decreases, and thus the curvature of the track changes along the particle's path. The original track reconstruction assumes the same curvature along the entire length of a track. Energy

loss per unit length in a material is also dependent on the type of particle being tracked, as the interaction cross-sections change for different particles. Different corrections are applied for pion, kaon, and muon track hypotheses using a Kalman fitter [24] when tracks are refit. Additionally, corrections to the magnetic field in the tracking volume and the silicon geometry are also applied [23].

2.3.2 The Tracking System

This section provides a description of the detector systems that provide the hit information required to track particles as described in the previous section.

2.3.2.1 Silicon Tracking

The inner-most tracker, L00, was added to the original CDF II upgrade design to improve the impact parameter resolution of the tracking system. L00 consists of 48 single-sided silicon wafers mounted directly to the Tevatron beam pipe. The wafers come in two widths; 8.4 and 14.6 mm wide, and are mounted in an overlapping, 12-sided pattern as shown in Figure 2.8. The inner (outer) wafers are mounted 1.35 (1.65) cm from the Tevatron beam. The silicon wafers are each 7.84 cm long, but are electrically bonded in pairs to form 15.7 cm long sensors. The entire length of the L00 detector is 0.9 m.

Each L00 silicon wafer consists of *p*-doped strips implanted on an *n*-doped substrate. The strips have a pitch of 25μm and a width of 8 μm. The strips are readout through AC coupling to an insulated conductor above the doped signal strip. L00 consists of 13,824

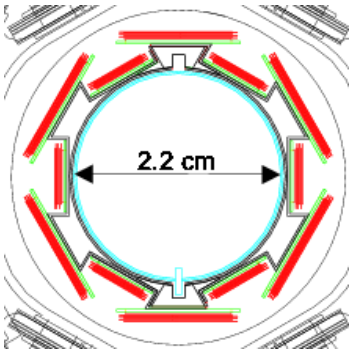

Figure 2.8: L00 silicon tracker.

individual readout channels.

The next tracker, radially outward from L00, is five layers of silicon that comprise the SVX II detector as shown in Figure 2.9. The SVX II detector resembles a series of five concentric cylinders that surround the beam pipe and L00. Each cylinder is divided into 3 barrels length-wise. Like L00, each cylinder, or layer, of SVX II consists of 12 silicon wafers, or ladders, that are each 29 cm long.

The silicon sensors in SVX II are all double-sided. The bulk material is nearly pure silicon with 60-65 μm pitch, 14 μm wide, *p*-doped, strips running axially down one side. Depending on the layer, the other side of the sensor consists of *n*-doped, stereo [2], strips that are arranged at a 90^o angle, or at a small angle relative to the length of the wafer. The pattern for the five layers of SVX II from the inside-out is 90^o, 90^o, -1.2^o, 90^o, and 1.2^o. The spacing of the stereo strips for each layer is 141 μm, 125.5 μm, 60 μm, 141μm, and 65 μm with strip widths of 20 μm for 90^o strips and 15 μm for small angle stereo strips. All SVX II channels use readout electronics similar to that of L00 that are mounted directly to

[2]Stereo strips provide information on the z-position of the track.

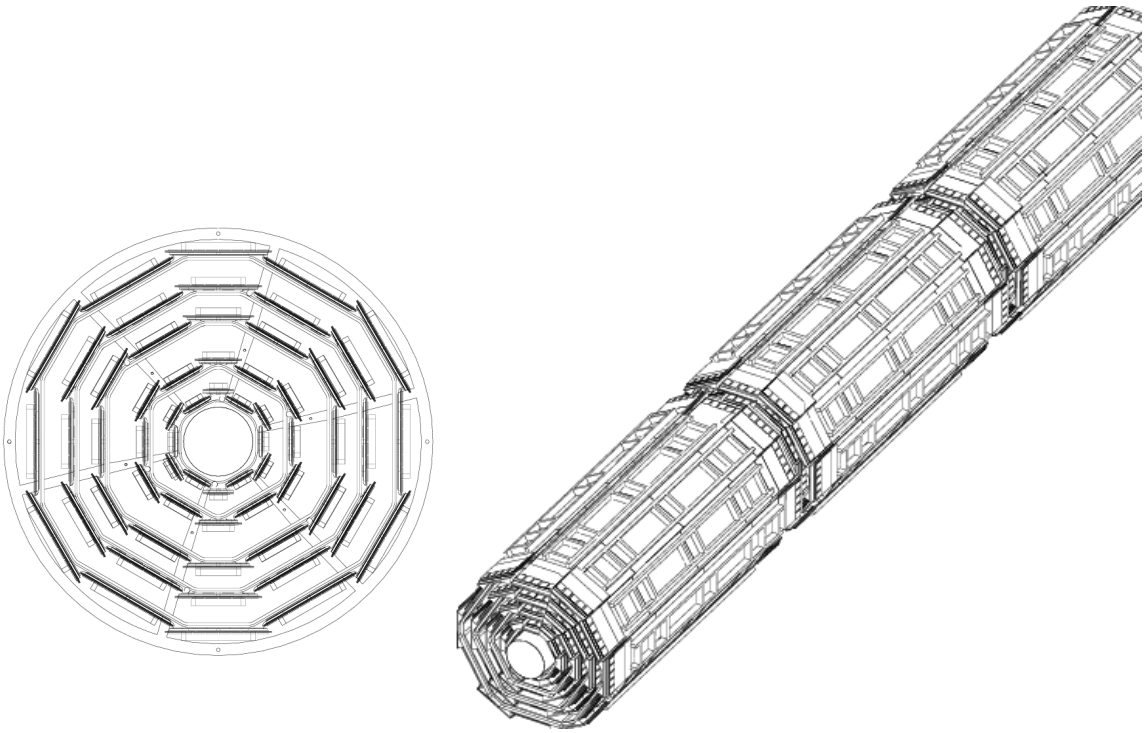

Figure 2.9: SVX II silicon tracker. Left: an end-view of the 5 layers of the SVX II detector. Right: a 3-D view illustrating the three-barrel structure of the detector.

the silicon wafers. SVX II consists of 405,504 individual readout channels.

Outside of the SVX II is one more Silicon sub-system called the ISL. The ISL provides another layer of tracking between the SVX II and the large COT drift chamber. As in SVX II, the sensors that make up the ISL are double-sided silicon wafers. The strip pitch on both sides of the ISL is 112 μm and uses the same readout electronics as the SVX II. One side of the ISL sensors are axial strips while the other side uses 1.2^o small angle stereo strips.

The ISL consists of 5 barrels as shown in Figure 2.10. The central barrel of the ISL consists of silicon wafers that are staggered at a radii between 22.6 cm and 23.1 cm from the beam. On either end of the ISL are two concentric barrels; the inner with sensors at

radii between 19.7 cm and 20.28 cm and the outer composed of sensors at radii between 28.6 cm and 29.0 cm from the beam. The two barrels at either end of the ISL provide tracking at high-η where, because of poor coverage, the acceptance of the COT is low.

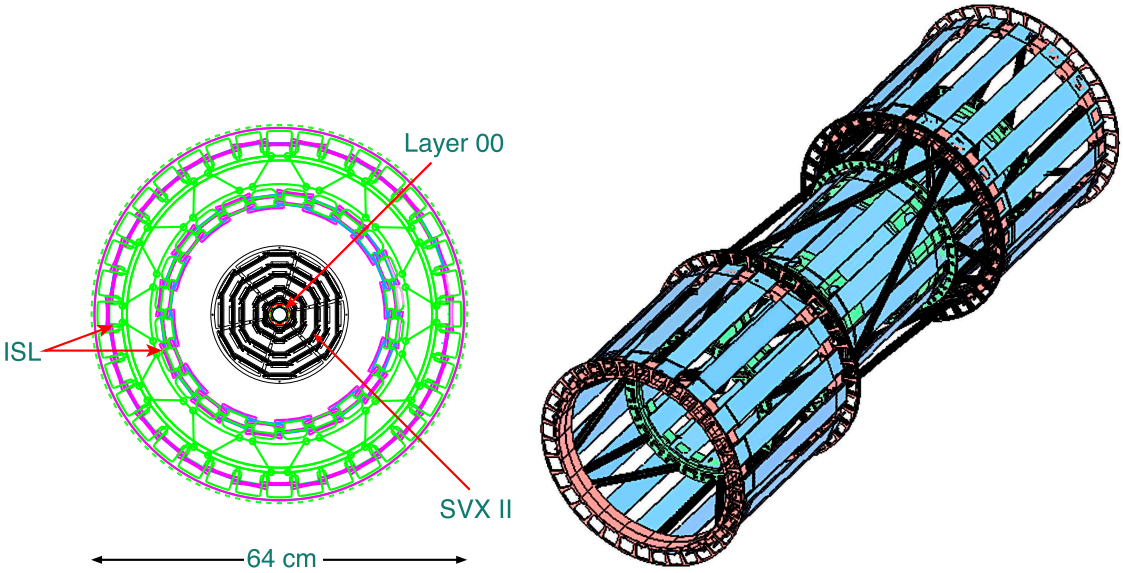

Figure 2.10: ISL silicon tracker. Left: end-view of the ISL. Right: The barrel structure of ISL. The barrels on either end consist of two layers of silicon, while the central layer is a single layer.

2.3.2.2 Central Outer Tracker

Outside the Silicon Tracker is a large cylindrical drift chamber called the Central Outer Tracker (COT). The COT is 310 cm long, covering a radius of 43.4 cm to 132.3 cm from the beam. The COT provides tracking for particles with pseudo-rapidity as high as 1.1 ($|\eta| < 1.1$).

The COT consists of 96 radial sense wire layers organized into 8 “superlayers” of 12 wires each. Superlayers 1, 3, 5, and 7 consist of wires that are oriented at a stereo angle of

$\pm 3^o$ relative to the beam while superlayers 2, 4, 6, and 8 consist of wires that are parallel to the beam. Each superlayer is divided in ϕ into "super cells". A super cell consists of one wire plane surrounded by a field plane on either side. A wire plane in a super cell consists of 12 sense wires, 13 potential wires, and 4 field-shaping wires. Figure 2.11 shows the cell layout for superlayer 2. Super cells are mounted at an angle of 35^o with respect to the $\hat{r}$ direction; providing better left-right hand curvature signal resolution during track reconstruction.

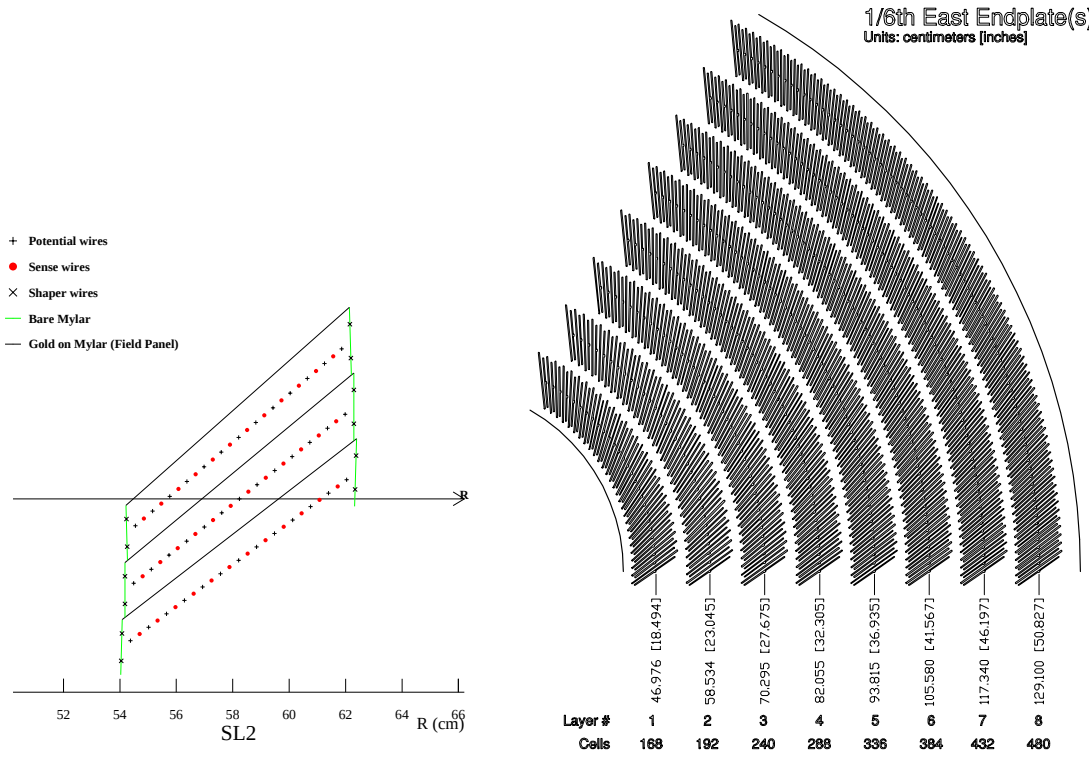

Figure 2.11: Cell layout of the COT. Left: The nominal layout for superlayer 2. Right: end-view of 1/6th of the COT wire planes.

Critical to the performance of the COT is low drift time. Drift time is a measure of how long it takes an ion to drift to a sense wire after being produced in the chamber. A mixture

of Argon/Ethane (50:50) is used in the COT to achieve a maximum drift time of 177ns over the 0.88cm, maximum drift distance in the COT.

CDF also has precise calorimeter and muon tracking systems that are not relevant for this analysis, but, for completeness, they are described in Appendix A.

2.3.3 Trigger Systems

Tevatron collisions at CDF occur every 396ns or at a rate of 2.5MHz. The maximum rate at which recorded events can be written is only about 75Hz. Since only a small fraction of the collisions can be recorded, CDF uses a three-level system of digital electronics to select events with signatures that indicate the presence of interesting underlying physics.

2.3.3.1 Level-1 Trigger

The Level-1 trigger stores data in a pipeline capable of storing detector information for up to 42 beam crossings. Simultaneously, data from the COT, calorimeters, and muon systems are analyzed using custom hardware to find particle tracks and jets.

Hit information from the four axial layers of the COT is sent to a custom piece of hardware called the eXtremely Fast Tracker (XFT) where tracks and particle jets are roughly reconstructed. The reconstructed tracks from the XFT are matched to muon and calorimeter information using look-up tables by the extrapolation unit (XTRP).

Based on the rough, Level-1, tracking information, a decision is made regarding the physics quality of the event based on the presence of various particle types (ie electrons,

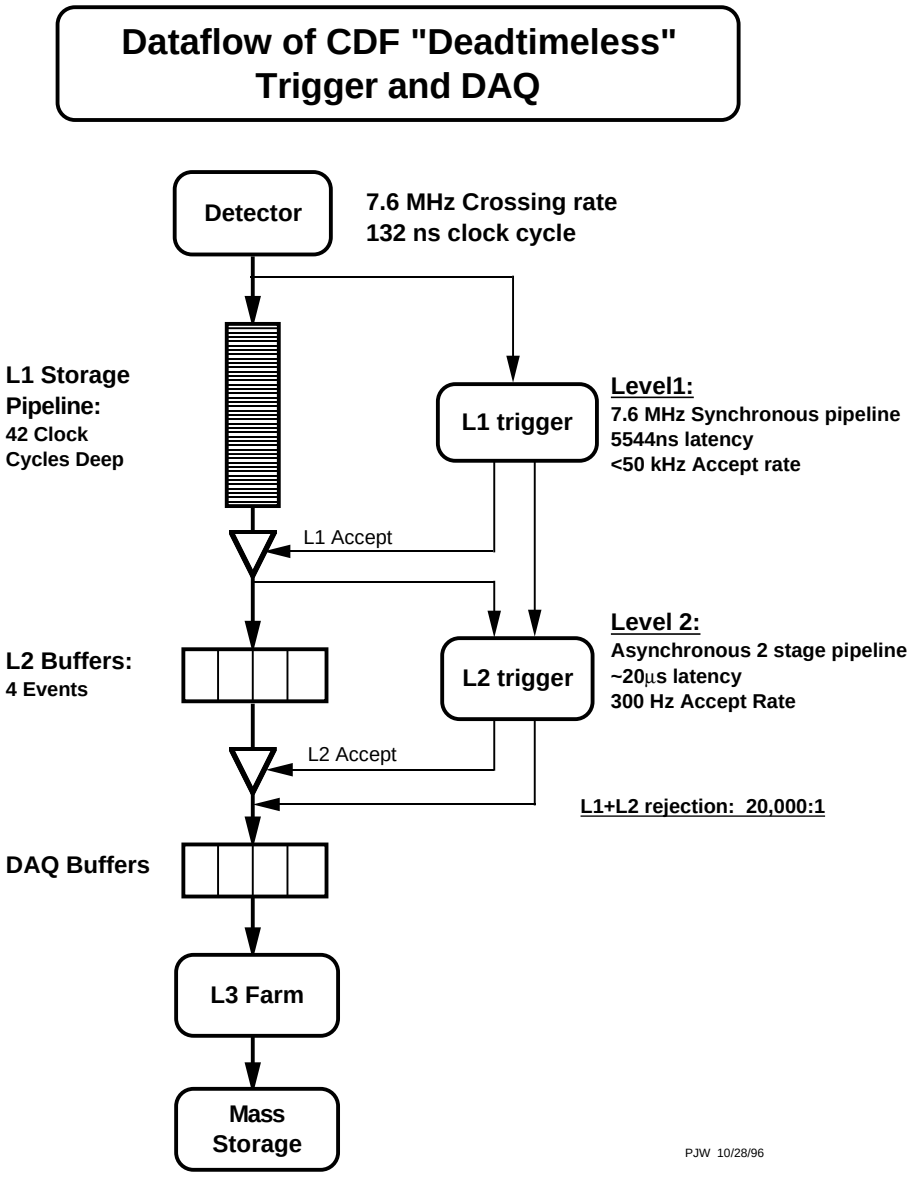

Figure 2.12: CDF data flow schematic.

muons, photons, and jets), missing energy, and transverse momentum. If the event is determined to be sufficiently interesting, the event is stored in one of four, Level-2 buffers for further reconstruction. The accept rate at Level-1 is limited to about 40kHz by the speed of the Level-2 trigger. About 1.5% of the total bunch crossings are accepted by Level-1.

2.3.3.2 Level-2 Trigger

Level-2, uses a combination of custom hardware and software to do a more sophisticated event reconstruction than was possible at Level-2. Level-2 processing begins as soon as an event passes Level-1 and is written to one of four, Level-2 buffers[3]. Level-2 combines the Level-1 trigger information with data from SVX II and the calorimeter shower-max detectors, in order to more precisely reconstruct an event.

At the heart of the CDF trigger system is the silicon DAQ. All three of the silicon tracking sub-systems use the same, SVX3D, *dead-timeless* readout chip. Each chip is able to store hit information for 128 channels in a 46 capacitor analog storage ring. The chip is said to be *dead-timeless* because it is capable of integrating the charge on one capacitor while reading from another. This mode of operation is crucial to the CDF trigger system and allows CDF to use the silicon hit information to make trigger decisions at Level 2.

Tracks from the XTRP are combined with SVX II hit information in the Silicon Vertex Tracker (SVT). The SVT is capable of quickly reconstructing the 2-D trajectory of tracks measured at CDF. The SVT is particularly important for the *b*-physics program at CDF. Hadrons that include a bottom quark have a relatively long lifetime (on the order of 10^{-12}s), and, at the Tevatron, are produced with enough momentum to travel a few millimeters before decaying. Because of this long lifetime, the decay products of a *b* hadron will be displaced (ie have a large impact parameter, d_0) from the primary vertex of the interaction. By triggering on displaced tracks, identified by the SVT, CDF is capable of triggering

[3]Level-2 dead-time occurs when all four of the Level-2 buffers are full and Level-1 accepts another event.

on events that are rich in heavy flavor physics. This capability of CDF is central to our measurement of the Λ_b^0 lifetime. Displaced tracks are illustrated in Figure 2.3 and the impact of the displaced track trigger on this measurement is discussed in more detail in Section 3.3 and Chapter 4.

The global Level-2 decision is made based on information from the SVT, calorimeter, and muon systems. The average Level-2 processing time is $\sim 30\mu s$. The Level-2 accept rate is set, by the capability of Level-3 to accept events, at about $600Hz$. When an event is accepted by the Level-2 trigger, information from the entire detector is read for that event and passed to Level-3.

2.3.3.3 Level-3 Trigger

When an event is accepted by Level-2, the hit information from all detectors is read and sent to the Level-3 processor farm by the Event Builder. The Event Builder is a small farm of Scanner CPUs which assemble the event data from the various detector sub-systems.

The L3 farm is composed of 16 sub-farms; each sub-farm consisting of 10-15 processing nodes and one converter node. A converter node receives the event from the Event Builder and distributes the event to the next available processor in its sub-farm. Each converter node has multiple event buffers, so that new events can be received while distributing others. The processor nodes are PCs running Level-3 reconstruction software, which fully reconstructs the event and checks all possible trigger paths before making the final trigger decision. Events that don't pass Level-3 are discarded, while accepted events are sent to

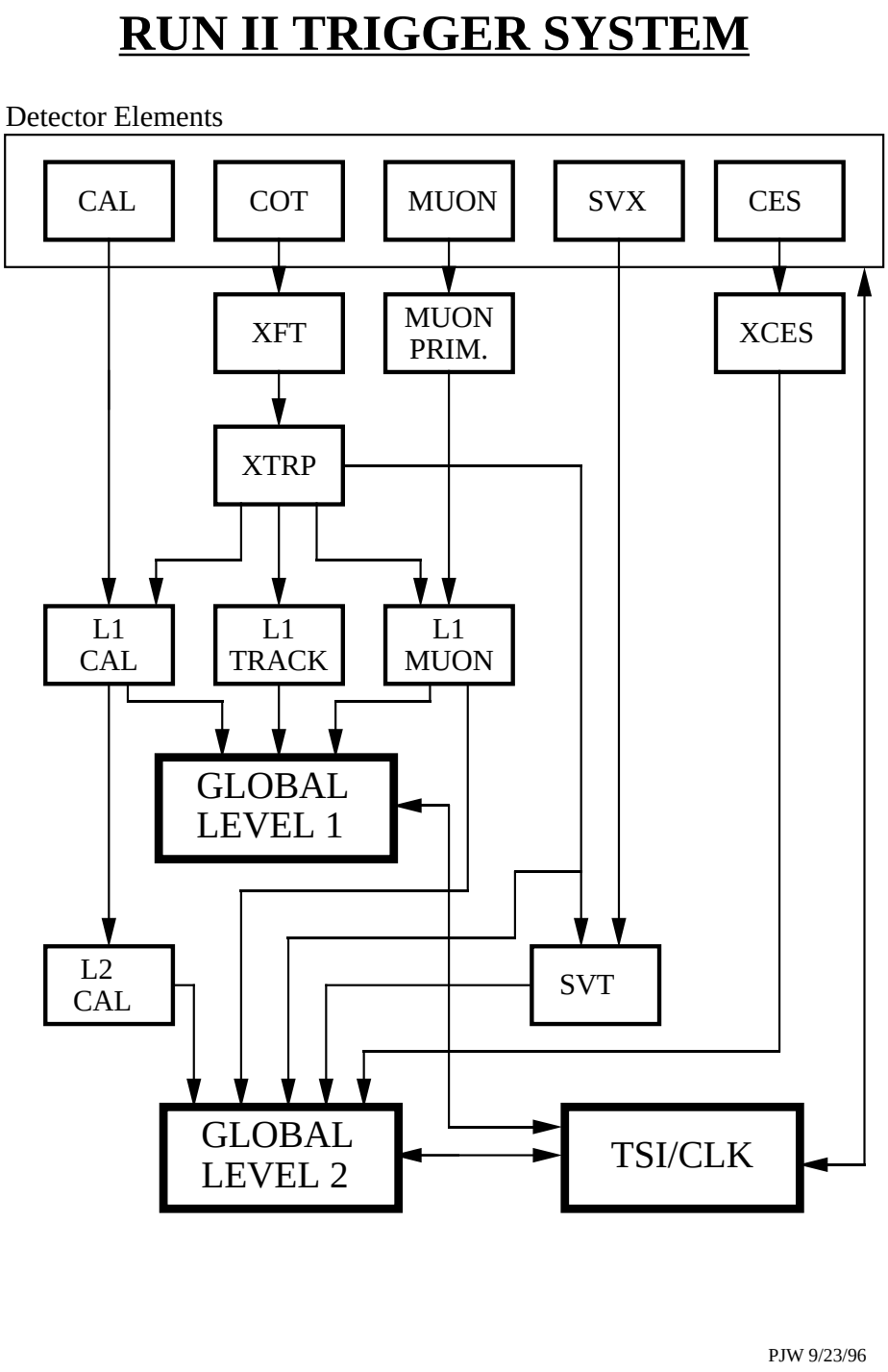

Figure 2.13: CDF trigger system block diagram.

the Consumer Server Logger (CSL) where events are monitored and written to disks for permanent storage. The accept rate at Level-3 is about 75 Hz.

Chapter 3

Methodology

3.1 Measuring the time of a particle's decay

In a detector with perfect resolution and without a trigger bias, the distribution of the proper decay time t' (or, equivalently, of the proper decay length, ct') of an unstable particle with *true* lifetime, τ (and $c\tau$) follows a simple exponential distribution. For a given Λ_b^0 candidate, the probability of observing a proper decay length ct' in the interval $[ct', ct' + cdt']$ is $P(ct')cdt'$, where

$$P(ct') = \frac{1}{c\tau} e^{\frac{-ct'}{c\tau}}. \tag{3.1}$$

is the Probability Density Function (PDF). The proper decay length, ct', is defined in terms of perfectly measured quantities to be

$$ct' \equiv \frac{L'_{xy} \cdot m_{\mathrm{PDG}} c}{p'_T}. \tag{3.2}$$

where L'_{xy} is the decay length projected in the transverse (xy-plane), p'_T is the transverse momentum, m_{PDG} is the true mass of the unstable particle (from Reference [8]), and c is the speed of light.

In practice, the *observed* proper decay length, ct, is defined in terms of quantities that have measurement errors (indicated by un-primed variables);

$$ct \equiv \frac{L_{xy} \cdot mc}{p_T}. \tag{3.3}$$

As the detector does not have perfect resolution, we need an expression equivalent to Equation 3.1 for ct from Equation 3.3 to account for this difference.

3.2 Detector Resolution

In a real detector, the measurement of L_{xy} has a finite resolution, and thus each measurement of ct' has an uncertainty σ_{ct}. This smearing of the true ct' which results in the measured value ct is accounted for by convoluting the measured lifetime with a function that describes the detector resolution[1]. The resolution function, $R(ct, \sigma_{ct}; ct')$, is the PDF of the measured ct and σ_{ct} given the true value of ct'. With this addition, the PDF for the measured proper decay length distribution becomes

$$P(ct|\sigma_{ct}) = \frac{1}{c\tau} e^{\frac{-ct'}{c\tau}} \otimes R(ct, \sigma_{ct}; ct'). \tag{3.4}$$

[1] In this analysis, the ct resolution is modeled by a sum of two Gaussians.

The probability density function $P(ct|\sigma_{ct})$, is a one-dimensional conditional PDF[2] that predicts the probability of observing this value of *ct given* the value of σ_{ct}. In order to obtain a proper two-dimensional PDF for both *ct* and σ_{ct} based on the conditional probability, the σ_{ct} distribution (PDF) must multiply $P(ct|\sigma_{ct})$. So the full two-dimensional *ct*-σ_{ct} PDF becomes;

$$\begin{aligned} P(ct,\sigma_{ct}) &= P(ct|\sigma_{ct})\cdot P(\sigma_{ct}) \\ &= \frac{1}{c\tau}e^{\frac{-ct'}{c\tau}} \otimes R(ct,\sigma_{ct};ct')\cdot P(\sigma_{ct}) \end{aligned} \tag{3.5}$$

where $P(\sigma_{ct})$ is the distribution of σ_{ct} observed in data.

The error on L_{xy}, σ_{Lxy} (and therefore also σ_{ct} due to Equation 3.3), as reported by a vertex-constrained kinematic fit, is usually underestimated. There are two reasons for this: one is the imperfect knowledge of the resolutions of silicon hits[3]. The other cause for the underestimation of the errors on the track parameters d_0, φ_0 and Z_0 (which propagate to the errors on the secondary vertex) is the small probability for the pattern recognition to pick up a wrong hit (*e.g.* in a dense track environment). This would result in tails in the track parameter distributions even if the silicon hits on tracks had perfect errors.

To account for these effects, the σ_{ct} estimated by a vertex-constrained kinematic fit, is multiplied by an additional scale factor, S_{ct}. One can estimate the value of this scale factor by comparing the true ct' obtained from the MC truth information in the $\Lambda_b^0 \to \Lambda_c^+\pi^-$ signal Monte Carlo with the *ct* measured in the same event. Figure 3.1 shows the same *ct* pull

[2]The conditional PDF is implemented via the RooFit toolkit using RooProdPdf with the optional Conditional(pdfSet,depSet) statement [46].

[3]We are using Gen 5 pattern recognition; the silicon hit resolutions were re-done in Gen 7 and the resolutions are larger, in particular on L00.

distribution $(ct' - ct)/\sigma_{ct}$) fit with a single Gaussian resolution function (Left) and a double-Gaussian resolution function (Right). It is clear from these fits, that the double-Gaussian resolution provides a better resolution model. Based on the result of this fit, a double-Gaussian resolution function is used to model the detector resolution in this analysis;

$$R(ct, \sigma_{ct}) = f \cdot Gauss(S_1 \cdot \sigma_{ct}) + (1 - f) \cdot Gauss(S_2 \cdot \sigma_{ct});$$

Where the relative fraction, $f = 0.76$, and the scale factor widths, $S_1 = 1.107$ and $S_2 = 1.508$ are all parameters obtained from the fit shown in Figure 3.1 (Right).

Throughout the analysis, the same fraction and relative widths are used to model the resolution. In particular, when generating the SVT efficiency and fitting the Λ_b^0 signal Monte Carlo sample (described in Section 4.3.1) the values obtained from the fit in Figure 3.1 are used. When fitting data, it is impossible to measure the *ct* resolution directly as done for the Monte Carlo; this is usually done via the prompt peak from the combinatorial background, but in this sample the peak has been removed by the Two Track Trigger. Instead, a global scale factor, S_{ct}, is used to scale σ_{ct}. The value of the narrow Gaussian is set to S_{ct} while the broad Gaussian is scaled in order to maintain the same relative widths between S_1 and S_2 as measured in the Monte Carlo. The choice of S_{ct} is somewhat arbitrary and is treated as a source of systematic error. It will be shown that the measurement is not sensitive to large variations in the choice of S_{ct}.

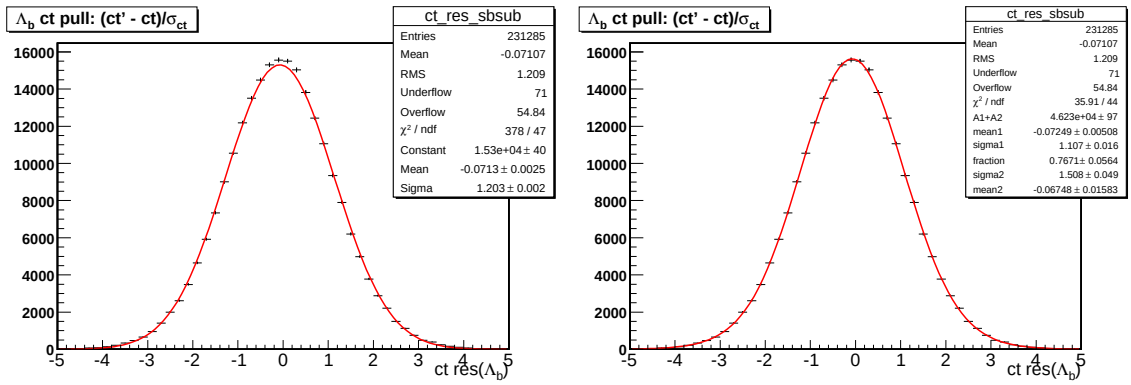

Figure 3.1: The $ct(\Lambda_b^0)$ pull $(ct' - ct)/\sigma_{ct}$ from HQGen $\Lambda_b^0 \to \Lambda_c^+\pi^-$ signal Monte Carlo. (Left) The distribution is fit with a single Gaussian resolution. (Right) The distribution is fit with a double Gaussian.

3.3 Trigger Efficiency

In addition to the detector resolution, the Two Track Trigger (TTT) introduces a bias on the observed proper decay length. Let us consider a simple example from everyday life: imagine if the average length of a human life was measured using a group of only people who graduated college and who hadn't yet retired from their jobs. The selection of the sample introduces a very strong bias on both the lower and upper value of a person's age. Similarly, the TTT selects events with two displaced tracks which removes both the events with short proper decay lengths, and those with very long ones. The resulting lifetime distribution is no longer exponential and this crucially (and dramatically) complicates the extraction of the lifetime.

In order to correct for the trigger selection bias, an efficiency function, $\varepsilon_{TTT}(ct)$, is introduced. To first order, the efficiency function depends only on the observed ct of each event and is computed using the $\Lambda_b^0 \to \Lambda_c^+\pi^-$ signal Monte Carlo sample described in

Section 4.3.1.

With the addition of the σ_{ct} scale factor S_{ct} and the efficiency function, $\varepsilon_{TTT}(ct)$, the joint two-dimensional $ct - \sigma_{ct}$ PDF becomes

$$P(ct, \sigma_{ct}; S_{ct}) = P(ct|\sigma_{ct}, S_{ct}) \cdot P(\sigma_{ct}) \cdot \varepsilon_{TTT}(ct). \tag{3.6}$$

Several Monte Carlo based methods for computing the trigger efficiency are described in Reference [1]. In all cases, a sample of simulated signal events are used to model the effect of the trigger and analysis cuts on measuring the lifetime. The efficiency function is of the form;

$$h_{TTT}(ct) = \frac{Histo^{TTT}(ct)}{\sum_i exp(ct^i, c\tau^{MC}) \otimes R(ct^i, \sigma_{ct}^i)}. \tag{3.7}$$

The numerator is the *ct* distribution of the realistically simulated signal events after all the trigger (and also offline cuts that may have impact on the proper time distribution or σ_{ct}) cuts have been applied. The denominator is computed in the following way; for each event that enters the histogram at the numerator, the following quantity is added to the content of each bin of a second histogram (with same number of bins of the numerator);

$$r_i = f(x_i, \sigma_{ct}) \tag{3.8}$$

where σ_{ct} is the uncertainty on *ct* of the event we are considering, x_i is the *ct* corresponding to the center of the *i*-th bin, and $f(x_i, \sigma_{ct})$ is the *normalized* distribution given by the convolution of an exponenatial (with lifetime $c\tau_{MC}$) with an appropriate resolution function centered at zero with a width equal to σ_{ct}. The ratio is the TTT efficiency as a function of *ct*represented as a histogram h_{TTT}.

In other CDF measurements of the lifetime-related quantities using the TTT data, the efficiency histogram, $h_{TTT}(ct)$, computed using Equation 3.7, was fit with an arbitrary function (preferably one that is analytically integrable) to obtain a parameterized efficiency function $\varepsilon_{TTT}(ct)$. We find that, due to differences in both the event selection and the properties of the decays (*e.g.*, a much shorter charm lifetime), the functional forms used in previous lifetime analyses do not adequately describe our distribution; leading to biases and instabilities in the final lifetime fit results. So, instead of parameterizing h_{TTT}, we use a smoothed version of the numerator in Equation (3.7), divide it by the same denominator, and use the resulting histogram directly;

$$\varepsilon_{TTT}(ct) = \frac{Histo^{TTT}_{smoothed}(ct)}{\sum_i exp(ct^i, c\tau^{MC}) \otimes R(ct^i, \sigma^i_{ct})}. \tag{3.9}$$

This method has the advantage of avoiding systematic error due to inadequate choice of parameterization to model the efficiency shape. However, since the shape of the smoothed distribution is arbitrary, we must now numerically integrate the PDF in Equation 3.6 in order to normalize it to unit area, making this approach computationally much more expensive.

3.4 Roadmap Towards a Lifetime Measurement

Let us now pause and review the ingredients of a lifetime measurement in a sample of fully reconstructed Λ_b^0 events collected with a displaced track trigger. Equation 3.6 has two parts, $\varepsilon_{TTT}(ct)$ and $P(ct|\sigma_{ct}, S_{ct})P(\sigma_{ct})$. Each part is discussed in detail below.

3.4.1 Building Confidence in $\varepsilon_{TTT}(ct)$

The TTT mangles the original exponential distribution of proper times. However, by computing the TTT efficiency, $\varepsilon_{TTT}(ct)$, with great precision, it is possible to disentangle the effect of the trigger on the measured proper time distribution and compute the lifetime of Λ_b^0 correctly.

The TTT efficiency, $\varepsilon_{TTT}(ct)$, is the probability that a given decay of the Λ_b^0 baryon passes the trigger. It depends on σ_{ct}(since we use the measured ct and not the true ct') but only very weakly. However, the TTT trigger efficiency depends crucially on both the kinematics of the decay and the behavior of the SVT trigger.

$\varepsilon_{TTT}(ct)$ is derived using realistic Monte Carlo simulation. A variety of checks are performed to compare the data and MC. Whenever a disagreement is found that stems from our lack of knowledge of production and decays of Λ_b^0 baryons, the Monte Carlo is reweighted to look like the distributions observed in data. The reweighting of the Monte Carlo is described in detail in Section 4.3.1.

In particular, the quantity called `trigCode` is important in identifying whether the decay kinematics of the particular Λ_b^0 candidate is simulated well (see Section 5.5.5). `trigCode` is a number used to classify the events in our sample according to which of the stable daughter tracks satisfy the requirements of the TTT. The fact that each `trigCode` sample results in a measured lifetime that agrees with the input value, confirms that both the decay kinematics and the detector simulation are at least consistent with each other for different categories of decays. The `trigCode` study builds confidence that $\varepsilon_{TTT}(ct)$ is correct within

the assigned systematic uncertainties.

Furthermore, a dedicated study, using $J/\psi \to \mu\mu$ decays, has been performed to quantify the accuracy of the SVX II and SVT simulation. The details of this study are documented in Section 7.2.2. No significant discrepancy is found between the actual data and the SVT model used in the simulation. However, due to limited statistics for the $J/\psi \to \mu\mu$ study, the SVT model is actually the leading source of systematic uncertainty for this measurement.

3.4.2 Building confidence in $P_{ct}(ct, \sigma_{ct}, S_{ct})$

The product $P(ct|\sigma_{ct}, S_{ct}) \cdot P(\sigma_{ct})$ is less controversial. However, two concerns need to be addressed:

1) S_{ct} is only roughly known. It is not possible to measure S_{ct} directly in our sample because it does not have the so-called 'prompt' peak [25]. A prompt peak is produced by events that decay very close to the Primary Vertex. In our sample, this peak is removed by the TTT requiring displaced tracks. However, the systematics due to unknown S_{ct} is small; large variations of S_{ct} (spanning the range from ~ 1.1 to ~ 1.5) produce very small (sub-micron) changes to Λ_b^0 lifetime, as is shown in Section 7. Thus, any choice of S_{ct} in a broad range is acceptable.

2) ct and σ_{ct} are correlated, since σ_{ct} depends on the kinematics of the decay (namely angles w.r.t. the flight path). However, this dependence between σ_{ct} and ct does not need to be represented as the joint two-dimensional PDF, but could also be modeled

by a dependence of the scale factor on ct: $S_{ct} = S_{ct}(ct)$. However, because of (1) above, the changes in the distribution of σ_{ct} do not really influence the value of the Λ_b^0 lifetime.

Therefore, if the claims made in this section are supported by evidence, both parts of Eq. 3.6 are correct within the assigned systematic errors, and we can proceed with a measurement of Λ_b^0 lifetime. The following sections demonstrate all of these points specifically.

Chapter 4

Data Samples

This chapter describes the data and Monte Carlo samples that are used in this analysis. Approximately 3,000 Λ_b^0 decays are reconstructed from CDF data that was collected over a span of about 4 years. The details of the CDF data samples, run ranges, triggers, and criteria used to reconstruct the Λ_b^0 candidates are given in Sections 4.1 and 4.2. This analysis also relies heavily on a simulated data sample to correct for the trigger bias on measuring the lifetime as described in Section 3.3. The techniques used to generate the Monte Carlo data sample from which the trigger correction is derived are described in Section 4.3. Finally, Section 4.4 describes a sample of $B^0 \to D^{*-}\pi^+$ decays that are used as a crosscheck to develop confidence in our lifetime fitting procedure.

4.1 Λ_b^0 Run Periods

The present analysis is based on events collected by the CDF detector from February 2002 through February 2006, with an integrated luminosity of $\mathcal{L} = 1070 \pm 60$ pb^{-1} before good run criteria are applied. We apply the same good run criteria as the CDF B_s mixing analysis [28]; these criteria reduce the number of reconstructed Λ_b^0 by about 8%. The stripped sample described in detail in Ref. [32] is used for this analysis. This sample is a combination of the compressed all-hadronic datasets `xbhd0d`, `xbhd0h` and `xbhd0i`. We use the `B_CHARM_SCENA` and `B_CHARM_HIGHPT` flavours of the two displaced track trigger for this measurement. There also exists a dataset with data which pass on the `B_CHARM_LOWPT` trigger configurations. Events in this dataset which pass the `B_CHARM_LOWPT` but not the `B_CHARM_SCENA` trigger configuration may be added to this analysis in the future to increase the Λ_b^0 statistics. We also discovered that there are some duplicated events present in this sample – events in the run ranges from 186040 to 211539 which were processed twice and thus contain exactly the same Λ_b^0 candidates. The second instance of these events was removed from the analysis.

4.2 Λ_b^0 Reconstruction

The stripped sample was produced with very loose cuts and reconstructed with the Universal Finder [41]. [1] We added in the Layer-00 (L00) silicon hits and also used Event

[1] We reconstructed Λ_b^0 from a xbhd0h subset of the data using three different packages: the Universal Finder, the JpsiXMods [42], and the BottomMods package [43]. No significant discrepancy in the Λ_b^0 yields

by Event Primary Vertexing. The tcl inputs for the Universal Finder track reconstruction are shown in Appendix B. To reconstruct a Λ_b^0 candidate, the selection module loops over three tracks, assumed to be proton, kaon, and pion candidates. These tracks must each pass basic track quality requirements:

- At least 5 hits each in 2 axial layers of the Central Outer Tracker (COT)
- At least 5 hits each in 2 stereo layers of the Central Outer Tracker (COT)
- At least 3 $r\phi$ hits in the Silicon Vertex Tracker (SVXII)

Additionally, each track must have an impact parameter (d_0) from the primary vertex of less than 0.1 cm and a transverse momentum of more than 500 MeV/c. The proton candidate is additionally required to have a transverse momentum greater than the pion candidate, and greater than 2.0 GeV/c. Once these tracks are selected, a kinematic fit is performed using `CTVMFT` to constrain the tracks to a common vertex. If this fit is successful, the following cuts are applied to this Λ_c^+ candidate:

- $\chi^2_{xy} < 30$
- $p_{\mathrm{T}}(\Lambda_c^+) > 4.3$ GeV/c
- $2.269 < |\mathrm{M}(pK\pi)| < 2.301$ GeV/c^2.

If the above criteria are satisified, the program enters a loop over the fourth track. This track, assumed to be a pion candidate, must again pass track quality cuts and have an

or signal between the three methods was found.

impact parameter < 0.1 cm, with a transverse momentum (p_{T}) of > 2.0 GeV/c. Another kinematic fit constrains this track along with the previous $pK\pi$ candidate vertex to form the Λ_b^0 candidate vertex. For this fit, the mass of the $pK\pi$ candidate is constrained to the Λ_c^+ mass from the PDG [8]. The requirements on this Λ_b^0 candidate are:

- $\chi^2_{xy} < 30$
- $4.8 < |\mathrm{M}(pK\pi\pi)| < 7.0$ GeV/c^2
- $p_{\mathrm{T}}(pK\pi\pi) > 6.0$ GeV/c
- $-0.007 < ct(\Lambda_c^+) < 0.028$ cm (w.r.t to Λ_b^0 vertex)
- $ct(\Lambda_b^0) > 0.025$ cm.

These are the basic requirements to reconstruct a Λ_b^0 candidate from the stripped sample, not the final analysis cuts. Cut optimization of the Λ_b^0 sample is described in detail in Reference [32]. The final cuts determined by this optimization and applied in this analysis are listed in Table 4.1. Using these cuts on the stripped data sample gives a $\Lambda_b^0 \to \Lambda_c^+\pi^-$ yield of 2927 ± 58 candidates in the signal region m(Λ_b^0) $\in$ [5.565, 5.670] GeV/c^2, with the Λ_b^0 mass plot shown in Figure 4.1.

Variable	Cut value
	B_CHARM_SCENA
$p_{\mathrm{T}}(\pi_b^-)$	> 2 GeV/c
$p_{\mathrm{T}}(p)$	> 2 GeV/c
$p_{\mathrm{T}}(p)$	$> p_{\mathrm{T}}(\pi^+)$
$p_{\mathrm{T}}(K^-)$	> 0.5 GeV/c
$p_{\mathrm{T}}(\pi^+)$	> 0.5 GeV/c
$ct(\Lambda_b^0)$	> 250 μm
$ct(\Lambda_b^0)/\sigma_{ct}$	> 10
$\left\|d_0(\Lambda_b^0)\right\|$	< 80 μm
$ct(\Lambda_c^+ \leftarrow \Lambda_b^0)$	> -70 μm
$ct(\Lambda_c^+ \leftarrow \Lambda_b^0)$	< 200 μm
$\lvert m(pK^-\pi^+) - m(\Lambda_c^+)_{PDG}\rvert$	< 16 MeV/c^2
$p_{\mathrm{T}}(\Lambda_b^0)$	> 6.0 GeV/c
$p_{\mathrm{T}}(\Lambda_c^+)$	> 4.5 GeV/c
Prob(χ^2_{3D}) of Λ_b^0 vertex fit	$> 0.1\%$

Table 4.1: Analysis cuts determined for Λ_b reconstruction.

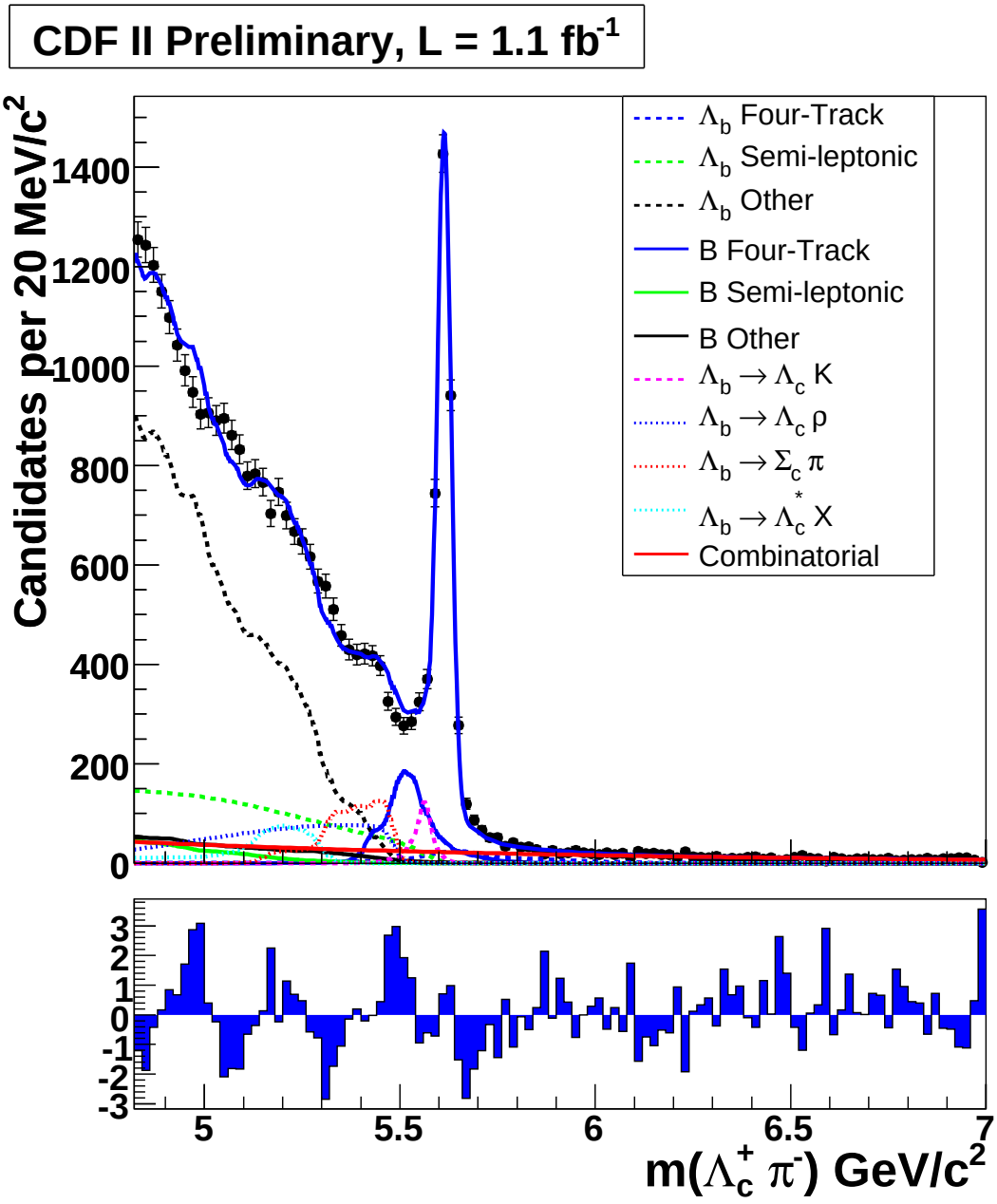

Figure 4.1: Λ_b^0 mass fit from Ref. [32]. The solid blue line is the total fit. The primary background components are listed in the legend and explained in detail in [32].

Quantity	Cut value
$Q(trk1) \times Q(trk2)$	< 0
$p_T(trk1) + p_T(trk2)$	$> 5.5\text{GeV/c}$
$p_T(trk1)$	$> 2.0\text{GeV/c}$
$p_T(trk2)$	$> 2.0\text{GeV/c}$
$\lvert z0(trk1) - z0(trk2)\rvert$	$< 5.0cm$
$\lvert D0_{SVT}(trk1)\rvert$	$[0.012, 0.1]cm$
$\lvert D0_{SVT}(trk2)\rvert$	$[0.012, 0.1]cm$
$p_{T(SVT)}(trk1)$	$> 2.0\text{GeV/c}$
$p_{T(SVT)}(trk2)$	$> 2.0\text{GeV/c}$
$\Delta\phi(trk1, trk2)$	$[2^\circ, 90^\circ]$

Table 4.2: Cuts used for offline confirmation of the Scenario A, Two Track Trigger

4.3 Monte Carlo Generation

All Monte Carlo samples are generated in the CDF II analysis framework, and involve the successive use of the following steps (performed by different executables):

Event Generation (cdfGen): This phase begins with an event generator which creates an event. The Monte Carlo samples in this analysis use either the PYTHIA [33], BGenerator [34], or HQGen [35] software packages. After the generation, a decayer program runs to simulate the decay of the generated particles; our samples use either the EvtGen [36] or QQModule [37] software packages. At this point b hadrons may be forced to decay only in a specified channel, such as $\Lambda_b^0 \to \Lambda_c^+\pi^-; \Lambda_c^+ \to pK\pi$.

Detector simulation (cdfSim): This phase runs a detailed simulation of the CDF II detector using the GEANT software package [38]. The CDF II detector simulation operates at the level of hits for all detector components except the calorimetry, where the shower evolution is computationally prohibitive. However, the tracking, especially the hits in the silicon detector, are simulated at a very detailed level, and include the strip-to-strip variations in performance as well as the generation of random noise throughout the detector. The output of cdfSim looks like the output from the CDF II data acquisition system.

Trigger simulation (TrigSim++): The detector-like event information is then fed to a trigger emulation system developed at CDF. TrigSim++ runs as an event filter, transmitting only those Monte Carlo events that would pass the real trigger system.

Event reconstruction (ProductionExe): Events that pass the trigger simulation are processed with the standard CDF II production executable. At this stage, the hits in the muon chambers (CMU, CMP, and CMX) are reconstructed and linked into muon stubs. Hits in the COT are reconstructed and linked into COT tracks. COT tracks are extrapolated and matched with the muon stubs. The other tracks are also extrapolated into the silicon detector where silicon hits are attached to these tracks. The output of ProductionExe has the same format as the final CDF II data.

Analysis reconstruction (Universal Finder): Finally, the Monte Carlo data is reconstructed by the same analysis code used to reconstruct the decay mode in data.

4.3.1 Λ_b^0 Signal Monte Carlo Sample

As outlined in Sec. 3.4.1, the TTT efficiency, $\varepsilon_{TTT}(ct)$, is obtained from the Monte Carlo simulation. In order to ensure that this procedure is not influenced by fluctuations, the Monte Carlo sample of $\Lambda_b^0 \to \Lambda_c^+\pi^-$ decays from which $\varepsilon_{TTT}(ct)$ is derived needs to be very large. A signal sample was produced using the HeavyQuarkGenerator (HQGen) package, which directly produces *b*-hadrons following a known kinematic distribution. For this purpose we used a custom $p_T(\Lambda_b^0)$ spectrum, measured and described in Reference [27]. The resulting Λ_b^0 hadrons are decayed, simulated, and reconstructed as described above. After the trigger and offline reconstruction selection cuts are applied, there are approximately *one million* events. This sample is the starting point for the re-weighting.

Re-weighting is a process used to sculpt a Monte Carlo distribution to look more like the same distribution observed in the data. Kinematic agreement between Monte Carlo and data is critical to correctly measuring the lifetime of Λ_b^0. The Monte Carlo has been re-weighted with respect to the Λ_c^+ Dalitz fractions, Λ_b^0 polarization, trigger track pairs (`trigCode`), and $p_T(\Lambda_b^0)$ to match the distributions observed in the data. A description of the re-weighting in each variable follows. After re-weighting, a sample of about $230,000$ signal Monte Carlo events remain. Several plots comparing the kinematics between the re-weighted Monte Carlo and sideband-subtracted data are given in Appendix C.

4.3.1.1 Primary Vertex Errors

When reconstructing $\Lambda_b^0 \to \Lambda_c^+\pi^-$ decays in data, event-by-event primary vertexing is used to better constrain the primary vertex position and more accurately estimate the associated errors. In the HQGen Monte Carlo sample, this approach is not possible because the sample lacks the prompt tracks required to do the event-by-event primary vertexing. In order to simulate event-by-event primary vertexing in the Monte Carlo, the distribution of PV errors, in x and y, from sideband-subtracted data are used to generate PV errors when reconstructing the Monte Carlo. Figure 4.2 compares the distribution of errors from sideband-subtracted data and Monte Carlo.

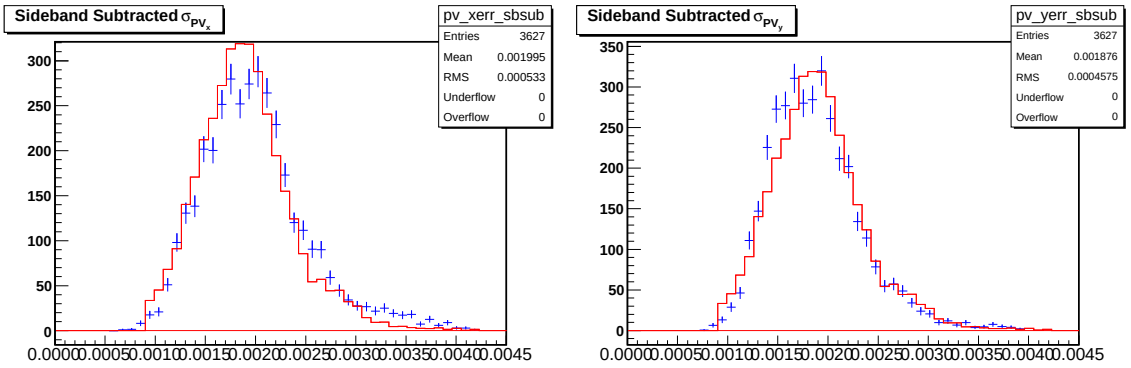

Figure 4.2: The distribution of primary vertex errors in x (Left) and y (Right). Sideband-subtracted data is shown in blue with errors. Monte Carlo errors (red) are generated based on the distributions observed in sideband-subtracted data.

4.3.1.2 Λ_c^+ Dalitz Fractions

Λ_c^+ decays via the following four dominant Dalitz modes; $\Lambda_c^+ \to pK^*$, $\Lambda_c^+ \to \Delta^{++}K^-$, $\Lambda_c^+ \to \Lambda(1520)\pi^+$, and the non-resonant $\Lambda_c^+ \to pK^-\pi^+$. The branching fraction for each mode has not been measured very accurately and consequently the uncertainty on each fraction is quite large. The latest branching fractions and their associated errors, from the PDG [8], are given in Table 4.3. The sample is weighted to the quoted PDG fractions. The uncertainty in the Dalitz fractions is treated as a systematic error.

4.3.1.3 Λ_b^0 Polarization Re-Weighting

The Monte Carlo programs in use, namely HQGen, Pythia and EvtGen, do not have provision for Λ_b^0 polarization. In an effort to take the true non-zero value of the polarization into account we re-weight the Monte Carlo to look like data following the prescription described in Reference [45].

Λ_c^+ **Decay Mode**	**Branching Fraction**
pK^*	22.7 $\pm$ 7.1%
$\Delta^{++}K^-$	12.2 $\pm$ 5.4%
$\Lambda(1520)\pi^+$	25.5 $\pm$ 8.5%
$pK^-\pi^+$ non-res	39.7 $\pm$ 11.3%

Table 4.3: PDG Λ_c^+ branching fractions

The angular distribution of $\Lambda_b^0 \to \Lambda_c^+\pi$ decay chain are best described using the following two variables:

- $\Theta_{\Lambda_c^+}$: the angle between the Λ_c^+ momentum in Λ_b^0 rest frame and the "Λ_b^0 production plane," defined by Λ_b^0's momentum in the lab frame and the beam direction.

- Θ_p: is the angle between the proton in Λ_c^+ rest frame and the "Λ_c^+ production plane," defined as the plane containing the Λ_b^0 and Λ_c^+ momenta.

We do not attempt to extract the true Λ_b^0 polarization from data, since these two distributions in $\Lambda_b^0 \to \Lambda_c^+\pi^-$ decays are only sensitive to the product of Λ_b^0 polarization and the decay asymmetry of Λ_c^+ decays, $\alpha_{\Lambda_c^+}$. Instead, we re-weight the distribution of $\cos\Theta_{\Lambda_c^+}$ and $\cos\Theta_p$ from the Monte Carlo to match the sideband-subtracted data.

Fig. 4.3, shows the distributions match very well in the case of $\Theta_{\Lambda_c^+}$. In the case of Θ_p, the Monte Carlo is re-weighted to better match the distribution observed in data. The uncertainty in the re-weighting is considered as a source of systematic error.

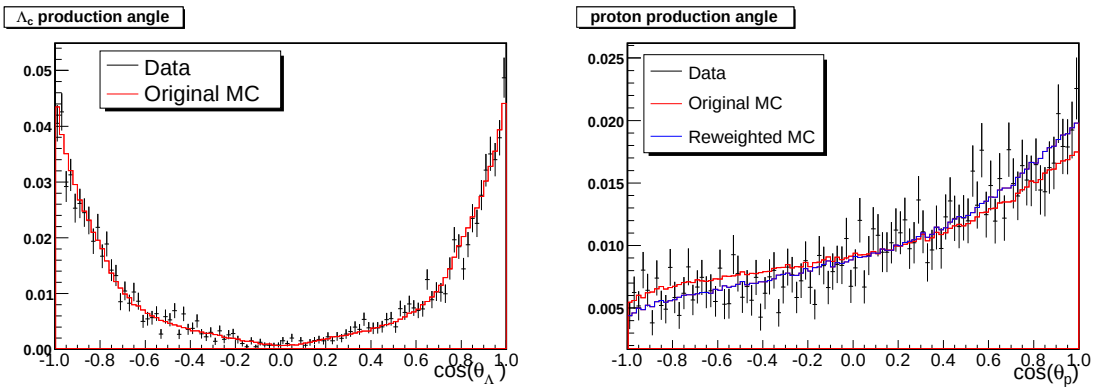

Figure 4.3: Left: Data (points) and Monte Carlo (red histogram) $cos(\Theta_{\Lambda_c^+})$ distribution. Right: Data and Monte Carlo raw (red), and re-weighted production distributions for $cos(\Theta_p)$. In the case of $cos(\Theta_p)$, the Monte Carlo has been re-weighted to better match the distribution observed in data.

4.3.1.4 Trigger Track Re-Weighting

The Two Track Trigger (TTT) requires a pair of stable tracks to fire. The kinematics of the decay can be very different depending on which pair of stable tracks satisfy the requirements (listed in Table 4.2) of the TTT. The decay; $\Lambda_b^0 \rightarrow \Lambda_c^+ \pi_2^-; \Lambda_c^+ \rightarrow pK^-\pi_1^+$ has four stable tracks that can be combined into four unique track pairs capable of satisfying the TTT. Each event is examined to determine which allowed pair(s) of trigger tracks satisfied the TTT. The distribution of tracks which satisfy the TTT selection is shown in Figure 4.4. The Monte Carlo is re-weighted to match the distribution of trigger tracks observed in data. The uncertainty in the re-weighting is considered as a source of systematic error.

4.3.1.5 $p_T(\Lambda_b^0)$ Re-Weighting

As previously mentioned, the Monte Carlo is generated using a custom $\eta(\Lambda_b^0)$ vs. $p_T(\Lambda_b^0)$ spectrum described in Reference [27]. However, the Monte Carlo $p_T(\Lambda_b^0)$ spec-

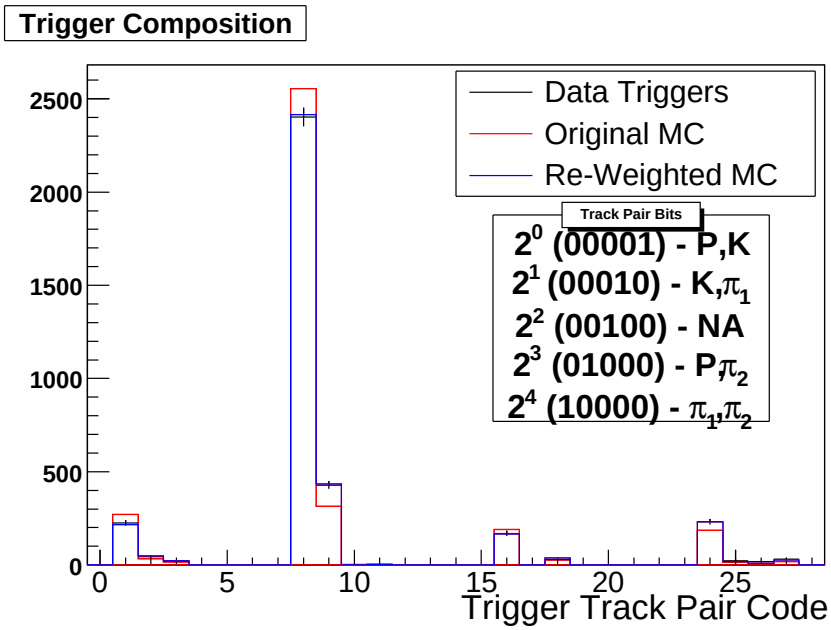

Figure 4.4: Distribution of track-pairs that sastify the TTT requirements in data (points with error bars) and the Monte Carlo (red) before re-weighting. Each track pair is assigned a bit as shown in the legend. For example, bin 9, shows the number of events where the p,π_2 **and** p,K track combinations both simultaneously satify the trigger requirements. (We note an excellent *a priori* agreement of the two distributions, considering how little we know about the Λ_b^0 decays.) The Monte Carlo is subsequently re-weighted (blue) to match the distribution observed in data.

trum does not completely agree with what is observed in the data, especially in the turn-on. Therefore, the turn-on ($p_T(\Lambda_b^0) < 10\text{GeV/c}$) of the spectrum in Monte Carlo is re-weighted to match the data. The data, original, and re-weighted Monte Carlo spectra are shown in Figure 4.5. The uncertainty in the re-weighting is considered as a source of systematic error.

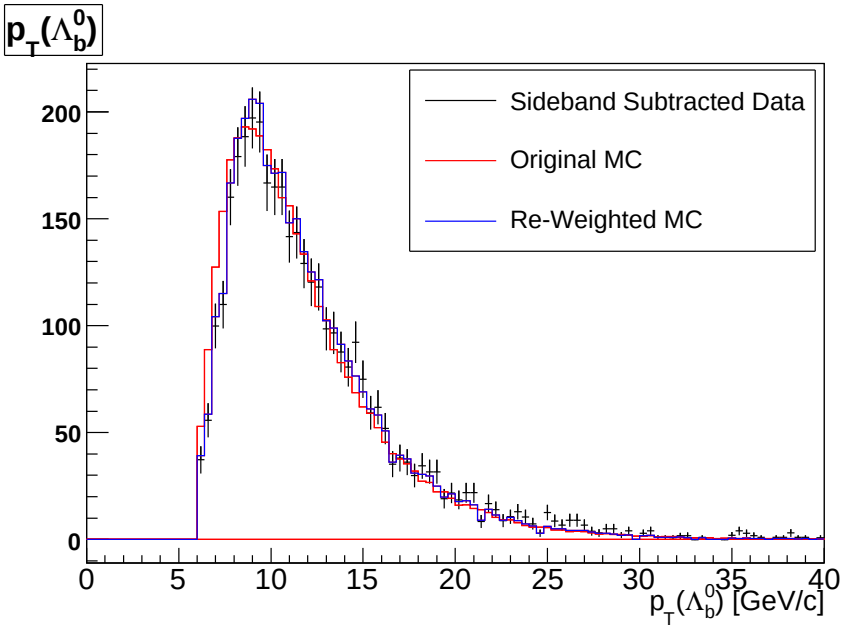

Figure 4.5: $p_T(\Lambda_b^0)$ distribution from data (points), original Monte Carlo (red), and re-weighted Monte Carlo (blue).

4.4 Cross-Check $B^0 \to D^{*-}\pi^+$ Sample

As a cross-check of our fitter, a sample of $B^0 \to D^{*-}\pi^+$ events is fit with a simplified lifetime model described in Section 5.6. The B^0 sample used is the same as that used for the recent CDF measurement of B^0, B^+ and B_s^0 lifetimes [30], [31].

The event selection and reconstruction used for the $B^0 \to D^{*-}\pi^+$ sample is described in detail in Reference [29]. The sample consists of events reconstructed in `xbhd0d`, `xbhd0h`, and `xbhd0i` datasets. The sample consists of about $\sim 16,500$ fully and partially reconstructed B^0 decays. For our cross-check, only the fully-reconstructed ($m \in [5.225, 5.331]$) candidates (~ 4000) are considered. The $D^{*-}\pi^+$ mass distribution is shown in Figure 4.6.

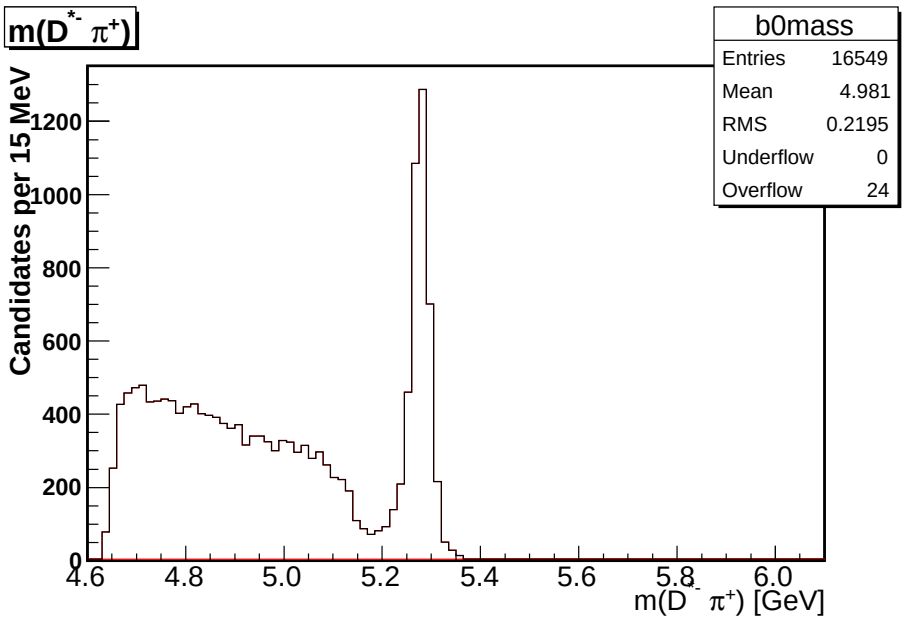

Figure 4.6: $B^0 \to D^{*-}\pi^+$ mass distribution from `xbhd0d`, `0h`, and `0i` data.

Chapter 5

Fit Description

A two-step process is used to obtain the lifetime of the Λ_b^0 baryon. In the first step, the sample composition is determined using a binned maximum likelihood fit of the invariant mass distribution of the $\Lambda_c^+\pi^-$ candidates. The chief objective of the first step (*ie. mass fit*) is to determine the composition of the $\Lambda_c^+\pi^-$ sample. In addition to the signal, there are several background components whose fractions are established via the mass fit.

The mass fit is described with the following likelihood;

$$-ln\ \mathcal{L}(m) = -N_T \sum_i ln\ \frac{N^i}{N_T} \cdot P_m^i(m) - N_T ln\nu + \nu \tag{5.1}$$

where ν is the expected number of events predicted by the PDF, N_T is the total number of events in the sample. m is the invariant mass of $\Lambda_c^+\pi^-$ candidates, the index i sums over all signal and background components, $P_m^i(m)$ is the invariant mass distribution of each of the components normalized to the unit area (so each is a proper probability density function (PDF)) and N^i is normalization of each of the components. This is an extended likelihood

fit with a number of external Gaussian constraints. The normalizations N^i are floating as fit parameters, and the main result of the mass fit is the set of N^i's and their errors. The Λ_b^0 mass fit is described further in Section 5.5.1.

In the Second step, the sample composition is fixed and the fit for the Λ_b^0 lifetime is performed. The lifetime fit is an unbinned maximum-likelihood fit in ct and σ_{ct}. Only events in the Λ_b^0 signal region are used in the lifetime fit. The mass PDFs, $P_m^i(m)$, from the mass fit are integrated over the signal mass region, and multiplied by the corresponding N^i to obtain the sample composition in the *signal* region. This yields $N^i_{\rm sig}$, or the number of events for each signal and background component in the signal region.

The likelihood of one event is a sum over several fit components, i, of two-dimensional distribution functions;

$$\mathcal{L}(ct,\sigma_{ct}) = \sum_i N^i_{\rm sig} \cdot P^i_{ct}(ct|\sigma_{ct}) \cdot P^i_{\sigma_{ct}}(\sigma_{ct}). \tag{5.2}$$

Here P^i_{ct} is the probability distribution of ct – a product of the proper time of the Λ_b^0 decay, t and the speed of light c. $P^i_{\sigma_{ct}}$ is the probability distribution of the error on ct. In this fit, all values of $N^i_{\rm sig}$ are fixed, and the Λ_b^0 lifetime is the sole parameter allowed to float. Moreover, several of the background components do not contribute to the signal region and are ignored in the lifetime fit.

Distributions used to model ct, and σ_{ct} are either defined parametrically or are obtained from templates derived from Monte Carlo or data samples, as discussed in the following sections.

5.1 Mass Templates

In general, the templates used to model the mass probabilities are derived from data and Monte Carlo samples. The observed mass distributions are either modeled parametrically with functions which are then fit to Monte Carlo distributions, or are modeled as histograms and simply smoothed.

5.2 Proper Decay Length Templates

The majority of the proper decay length PDFs $P^i_{ct}(ct|\sigma_{ct})$ from Equation 5.2 are broken into a product of $\varepsilon_{TTT}(ct)$, obtained using the procedure outlined in Sec. 3.3, and an analytical function, as given in Equation 3.6. Only one shape – the combinatorial background – is completely modeled by a histogram (of ct from events in the upper-sideband), smoothed using the kernel-estimating algorithm provided by RooFit called RooKeysPdf [26].

5.3 σ_{ct} Templates

The templates for σ_{ct} are derived directly from the data that is being fit. Only two σ_{ct} distributions are used for any of the several PDF components present in the lifetime fit: $P^s_{\sigma_{ct}}$ describes the distribution of errors for the Λ^0_b signal and B meson background components and $P^b_{\sigma_{ct}}$ describes the combinatorial background. It has been shown that the σ_{ct} distributions for signal Λ^0_b and B decays are very similar in the inclusive realistic Monte

Carlo (see Figure 5.1, Right). $P^s_{\sigma_{ct}}$ is obtained from the sideband-subtracted data while $P^b_{\sigma_{ct}}$ is taken directly from the upper-sideband.

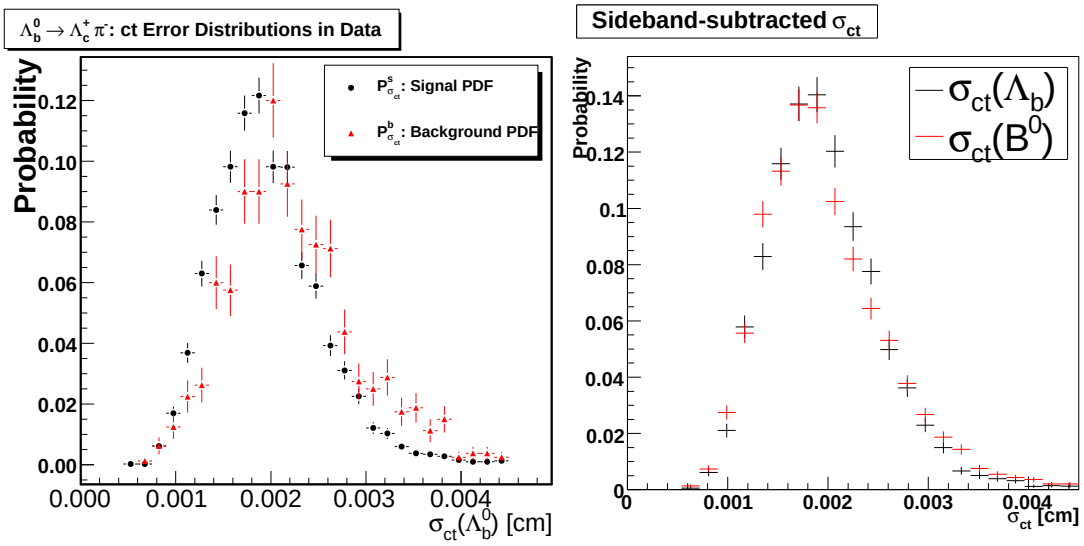

Figure 5.1: Left: The $P^s_{\sigma_{ct}}$ distribution from the sideband subtracted Λ_b^0 and B meson decays (black) and the combinatorial background, $P^b_{\sigma_{ct}}$ (red). Right: The distribution of σ_{ct} from sideband subtracted $\Lambda_b^0 \to \Lambda_c^+ \pi^-$ (black) and $B^0 \to D^{*-}\pi^+$ (black) data events. The agreement between B and Λ_b^0 distributions is good, and is the basis for using the same $P^s_{\sigma_{ct}}$ distribution for both the Λ_b^0 and B^0 components of the fit.

5.4 Efficiency Distribution

The TTT efficiency distributions, used in each fit, are computed from realistic signal Monte Carlo samples using Equation 3.9.

A comprehensive description of each lifetime fit; including the shapes used for the proper decay templates, σ_{ct} templates, and efficiency distributions is given in the following sections.

5.5 Lifetime Fit in $\Lambda_b^0 \to \Lambda_c^+\pi^-$ Decays

5.5.1 $\Lambda_b^0 \to \Lambda_c^+\pi^-$ Mass Fit

The Λ_b^0 mass fit is a one-dimensional, extended likelihood fit with Gaussian constraints as described above. All normalizations are allowed to float, though they may be constrained to an external number, or to another component. The $\Lambda_c^+\pi^-$ components are divided according to the number of *stable*[1]daughters. The mass fit is composed of the following 12 shapes.

1. $\underline{B \text{ Meson Four-Track}}$: decays starting with B^0 or B_s that have exactly four charged stable daughters and exactly zero neutral stable daughters. Mostly $\bar{B}^0 \to D^+\pi^-$, this forms a lumpy peak below the signal mass mean position. This shape (Figure 5.2) is derived from realistic signal Monte Carlo using `RooKeysPdf` smoothing.

2. $\underline{B \to \ell\bar{\nu}_\ell X}$: B meson semi-leptonic modes. The lepton in question must be stable and hence modes decaying via τ lepton are excluded from this category. This shape (Figure 5.2) is derived from a QuickSim Monte Carlo sample using `RooKeysPdf` smoothing.

3. $\underline{B \text{ Other}}$: all other decay modes starting with B^0, $B^\pm$ or B_s. This shape (Figure 5.3) is derived from the QuickSim sample using `RooKeysPdf` smoothing.

[1]Particles that do not decay inside the CDF detector are considered to be stable. For example, muons are taken to be "stable".

4. $\underline{\Lambda_b^0 \to \Lambda_c^+ \pi^-}$: the signal mode. This shape is modeled by a Gaussian PDF plus exponential-like tails on both sides to account for the resolution effects. (The tails are implemented as exponential decay PDF using a Gaussian resolution model.) The mean position of the Gaussian PDF and the mean position of the smeared decay PDF are taken to be the same, as are the standard deviations of the Gaussian PDF and Gaussian resolution model. The amount of tails is determined to the fit to the signal-only $\Lambda_b^0 \to \Lambda_c^+ \pi^-$ sample based on Pythia, since the extra hits from fragmentation tracks allow for a more realistic description of the pattern recognition mistakes in COT which cause the tails.

5. $\underline{\Lambda_b^0 \text{ Four-Track}}$: Similar to the B four-track decays. These are Λ_b^0 decays that have exactly four charged stable daughters and exactly zero neutral stable daughters. This shape resides more or less entirely within 2σ of the signal mass mean position, as shown in Figure 5.4). It is derived from a QuickSim Monte Carlo sample on account of its low statistics in the realistic simulation and employs `RooKeysPdf` smoothing. It is expected that the overall normalizaton of this shape is small, however with a large systematic uncertainty – neither of the decay modes that comprise this shape has been observed, so all their branching fractions are guesses.

6. $\underline{\Lambda_b^0 \to \ell \bar{\nu}_\ell X}$: Λ_b^0 semi-leptonic modes. Similar to the B semi-leptonic category. Decays proceeding with τ leptons as a primary daughter are excluded. This shape (Figure 5.4) is defined parametrically. The distribution from the inclusive realistic Monte

Carlo, $\Lambda_b^0 \to \Lambda_c^+ X$, sample is fit with a Gaussian plus an exponential with a cutoff at the high mass range.

7. $\Lambda_b^0 \to \Lambda_c^+ K^-$: the Cabbibo-suppressed mode. Shifted down from the signal mass mean position by approximately the difference between the pion and kaon masses, this shape (Figure 5.5) is derived from the realistic Monte Carlo using `RooKeysPdf` smoothing.

8. $\Lambda_b^0 \to \Lambda_c^+ \rho^-$: this mode is separated from the other Λ_b^0 decays on account of the poor knowledge of its relative branching ratio. The shape (Figure 5.5) is defined parametrically by fitting the realistic simulation with a Gaussian plus an exponential with a cutoff in the high mass region.

9. $\Lambda_b^0 \to \Sigma_c^+ \pi^-, \Sigma_c^{+*} \pi^-$: also separated from other Λ_b^0 decays on account of the poor knowledge of its relative branching ratio. This shape (Figure 5.6) is derived from realistic simulation using `RooKeysPdf` smoothing.

10. Λ_b^0 Bump: mainly composed of $\Lambda_b^0 \to \Lambda_c^{+*} X$. This shape was also originally included in the 'Λ_b^0 Other' category but was separated because of the poor knowledge of its relative branching ratio. This shape (Figure 5.6) is derived from realistic simulation using `RooKeysPdf` smoothing.

11. Λ_b^0 Other: all other decays originating from Λ_b^0 , which are not alredy included in one of the other categories. This shape (Figure 5.7) is derived from the realistic simulation using `RooKeysPdf` smoothing.

12. True Combinatorial Background[2]: modeled by a single falling exponential PDF. In the $\Lambda_c^+\pi^-$ invariant mass fit, the decay constant in the exponential is floating. The *ct* part of this component is determined by fitting the data sample on the upper sideband region, $m(\Lambda_c^+\pi^-) \geq 5.7$ GeV/c^2.

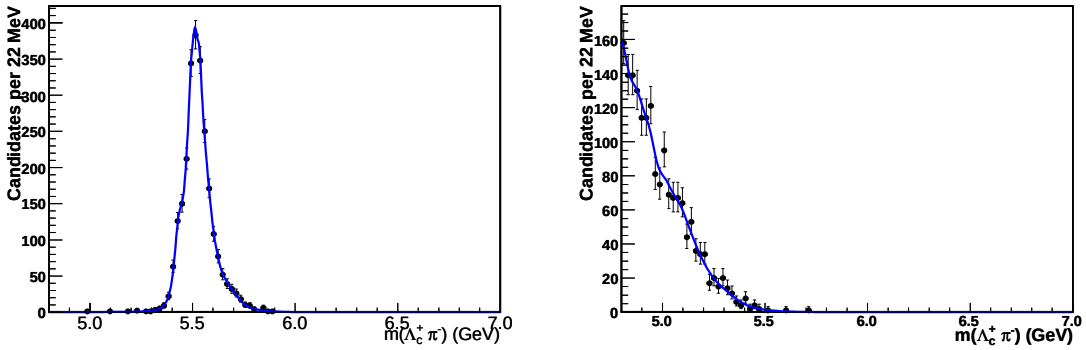

Figure 5.2: Left:*B* **Four-Track** realistic simulation distribution. Right: $B \to \ell\overline{\nu}_\ell X$ Quick-Sim distribution.

[2]Other $B \to D\pi$ mass fits used at CDF usually employ a parameterization of a constant + exponential to describe the combinatorial mass shape. This shape results in a more quickly falling background below the main Gaussian peak. That shape includes the combinatorial background of the "*D*" meson because the definition of other shapes does not include the contribution of decays that do not decay to "*D*", but contribute to the "*D*" combinatorial background. In our analysis, we explictly include in non-combinatorial components the Λ_b^0 and *B* decays that contribute to Λ_c^+ sidebands. After comparing those components and the Λ_c^+ sidebads, we do not have evidence that the shape of the true combinatorial background (*i.e.* in which at least one track is fake) is not a simple exponential.

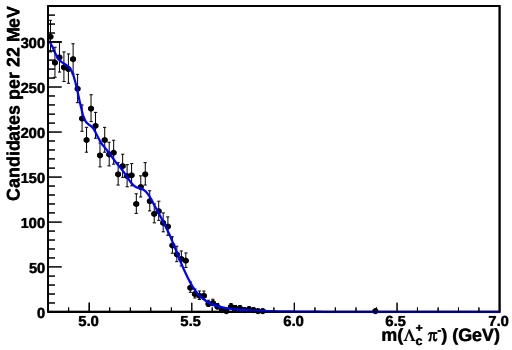

Figure 5.3: *B* **Other** QuickSim distribution

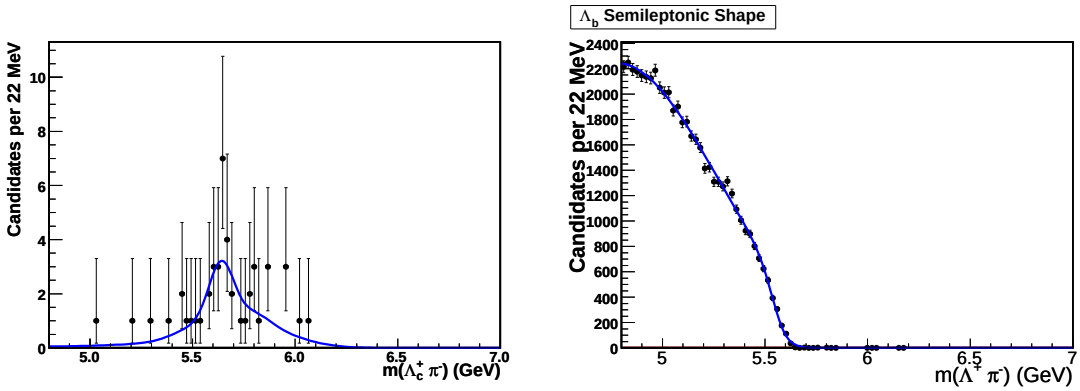

Figure 5.4: Left: Λ_b **Four-Track** QuickSim distribution. Right: $\Lambda_b \to \ell\bar{\nu}_\ell X$ realistic simulation distribution.

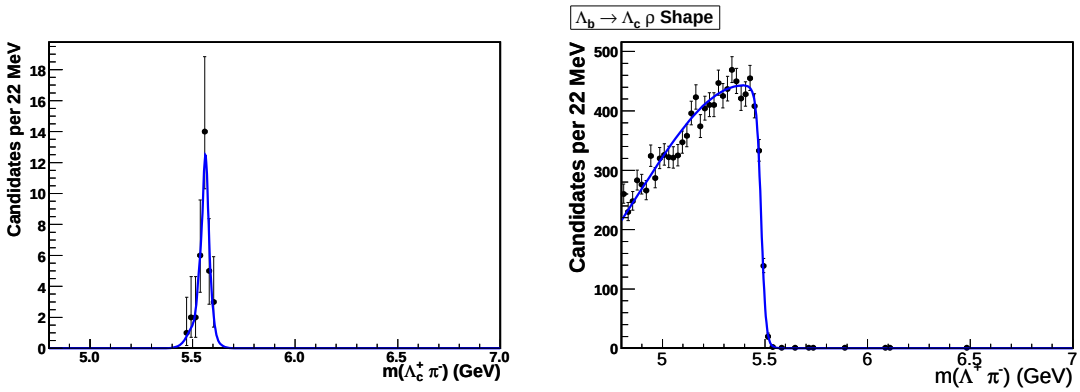

Figure 5.5: Left:$\Lambda_b^0 \to \Lambda_c^+ K^-$ realistic simulation distribution. Right: $\Lambda_b^0 \to \Lambda_c^+ \rho$ realistic simulation distribution.

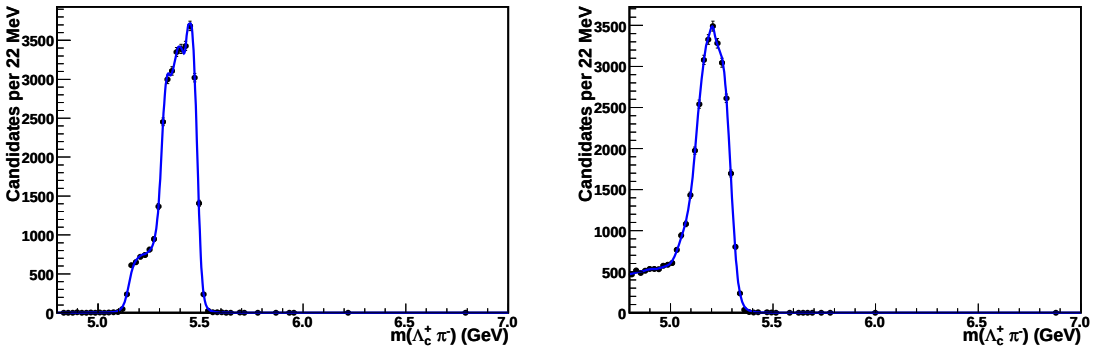

Figure 5.6: Left:$\Lambda_b^0 \to \Sigma_c^+ \pi^-$ realistic simulation distribution. Right: $\Lambda_b^0 \to \Lambda_c^{+*}$ realistic simulation distribution.

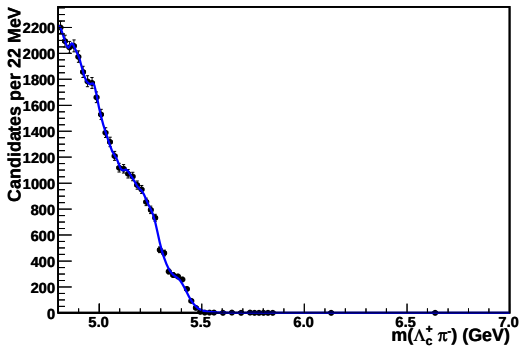

Figure 5.7: Λ_b **Other** realistic simulation distribution.

5.5.1.1 Fit Constraints

Because several background shapes are quite similar (e.g. B semi-leptonic and Λ_b^0 semi-leptonic) and since all of the normalizations are allowed to float in the fit, it is necessary to constrain the ratios of several normalizations to improve fit stability. The constraints described below appear as χ^2 penalty terms in the extended negative log likelihood. For brevity, the categories *all mesons* and *all baryons* are defined as the sum of all categories starting with B and Λ_b^0 respectively. The following constraints are imposed on the mass fit:

1. B Four-Track Candidates: The normalization of this component is based on the number of B^0 decaying to a kaon and three pions (including, for example, $\bar{B^0} \to D^+\pi^-$), which is observed in the $\Lambda_c^+\pi$ sample when the mass of the proton candidate track has been replaced by m_π. The fit of the invariant mass of such $B \to \cdots \to K3\pi$ candidate is given in Figure 5.8. The total number of $B \to \cdots \to K3\pi$ candidates obtained from $\Lambda_c^+\pi$ data this way still needs to be scaled up to accomodate the B reflections which do not fit the $K3\pi$ signature. This scale factor is obtained from the inclusive MC simulation and is found to be 1.75. As the events from the $B \to \cdots \to K3\pi$ invariant mass distribution come from the $\Lambda_c^+\pi$ sample itself, we do not consider the statistical error from the B mass fit. However, the scale factor based on the MC simulation depends on PDG branching ratios [8], and we do use their combined relative error of 0.0906. The number of B four-track events are constrained to

$$N_{BFour-Track} = 1356 \pm 125.$$

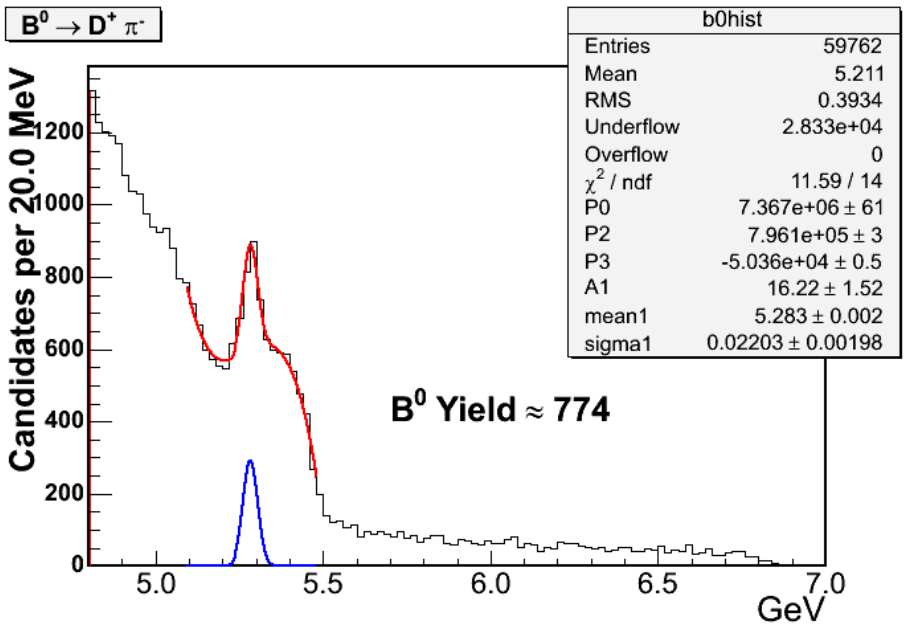

Figure 5.8: The fit of the invariant mass of $B \to K3\pi$ candidates. This distribution is computed from the $\Lambda_c^+\pi$ mass distribution where the mass of the proton candidate track, from $\Lambda_c^+ \to pK\pi$, has been replaced by the mass of a pion.

2. B Semi-Leptonic Candidates to All B Meson Candidates: The value of this constraint is obtained from the Generic Realistic sample. The relative error comes from the measurement of the B^0 semi-leptonic branching fraction. Using the PDG value, one obtains the error on the ratio of B semileptonic to all B meson events of 0.012.

$$\frac{N_{B\to\ell\bar{\nu}_l}}{N_{allmesons}} = 0.195 \pm 0.002$$

3. Λ_b^0 Semi-leptonic Candidates to $\Lambda_b^0 \to \Lambda_c^+\pi$ Candidates: The amount of Λ_b^0 semi-leptonic events is pinned down to the $\Lambda_b^0 \to \Lambda_c^+\pi$ signal itself, using Reference [39]. After taking the efficiencies into account, we get

$$\frac{N_{\Lambda_b^0\to\ell\bar{\nu}_l}}{N_{\Lambda_b^0\to\Lambda_c^+ pi}} = 2.87 \pm 0.53.$$

4. Total Number of *b*-baryon Candidates: While the total contribution of various *B* meson decays is relatively straightforward to estimate from the known branching fractions measured at the *B* factories, there is a considerable uncertainty in estimating the *total* number of Λ_b^0 decays that end up in our $\Lambda_c^+\pi$ sample.

   We therefore adopt the following strategy: we subtract the Λ_c^+ sidebands, and that way remove almost all contribution from *B* meson decays, as well as Λ_b^0 decays that do not produce a Λ_c^+, or those that do, but into a Λ_c^+ which does not decay to $pK\pi$. From Figure 5.9 we measure $30,976$ Λ_c^+ candidates in the data. Next, we extrapolate the $\Lambda_c^+\pi$ combinatorial background (composed of true-Λ_c^+ and fake π-from-Λ_b^0 pairs) from the upper sideband back to lower masses (see Figure 5.10), calculate the total amount of π-from-Λ_b^0 combinatorial background and subtract that too from the area of the Λ_c^+-sideband-subtracted distribution. We subtract about 2500 true-Λ_c^+ , fake-π events, which leaves us with about $28,500$ Λ_c^+ candidates. What remains is the total of Λ_b^0 decays from our sample which decay to $\Lambda_c^+ X$, with $\Lambda_c^+ \to pK\pi$. That number needs to be multiplied by a correction factor of 1.04, which takes into account the Λ_b^0 decays that do not result in $\Lambda_c^+ X, \Lambda_c^+ \to pK\pi$. Following this procedure, we obtain the total number of Λ_b^0 candidates as $28,272$. We assign the uncertainty of $\sim 5\%$ to this overall Λ_b^0 yield. This is motivated mainly by the lack of understanding of the Λ_b^0 branching fractions. The non-$pK\pi$ baryon contribution is determined largely by the Λ_b^0 branching fractions with large uncertainties, since most of them have not be observed and are mere theoretical estimates. Therefore, the total number of Λ_b^0

candidates in the mass fit is constrained to

$$N_{\Lambda_b^0 \rightarrow \text{ anything}} = 28,272 \pm 1,414$$

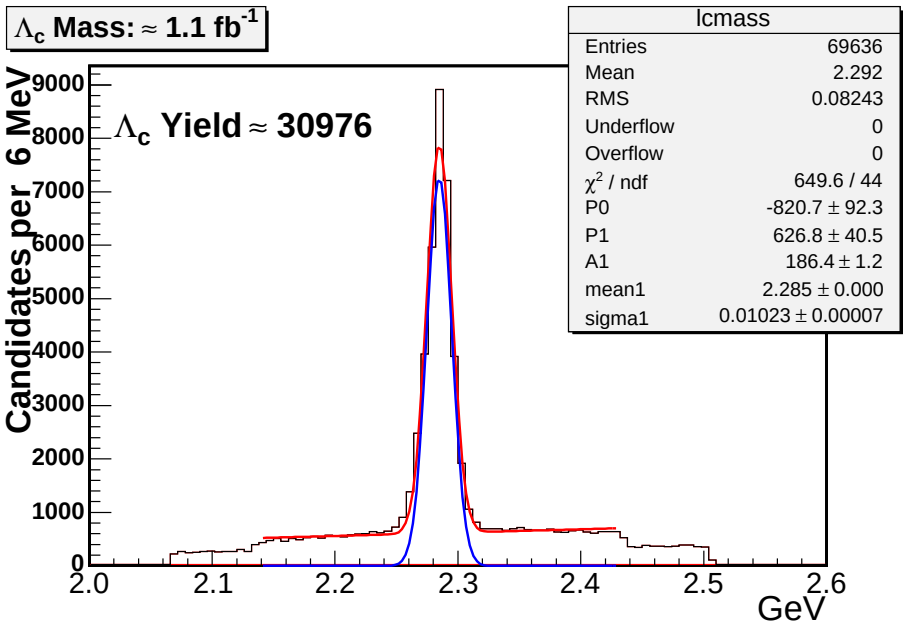

Figure 5.9: $m(pK\pi)$ distribution. We fit the signal distribution with a Gaussian and the background with a straight line. We count $\sim 31,000$ Λ_c^+ candidates in our data sample.

5. $\Lambda_b^0 \rightarrow \Lambda_c^+ K^-$ to $\Lambda_b^0 \rightarrow \Lambda_c^+ \pi^-$ Events: This constraint is based on the prediction made from [40] for the ratio of $B \rightarrow D\pi$:$B \rightarrow DK$ events. We use the following constraint.

$$\frac{N_{\Lambda_b^0 \rightarrow \Lambda_c^+ K^-}}{N_{\Lambda_b^0 \rightarrow \Lambda_c^+ \pi}} = 0.07 \pm 0.021.$$

6. $\Lambda_b^0 \rightarrow \Lambda_c^+ \rho$: we again use the results from [40]. to constrain the ratio of $N_{\Lambda_b^0 \rightarrow \Lambda_c^+ \rho}$ to $N_{\Lambda_b^0 \rightarrow \Lambda_c^+ \pi}$. The relative error is taken from the uncertainty on $B \rightarrow D\rho$ decays.

$$\frac{N_{\Lambda_b^0 \rightarrow \Lambda_c^+ \rho}}{N_{\Lambda_b^0 \rightarrow \Lambda_c^+ \pi}} = 0.56 \pm 0.10$$

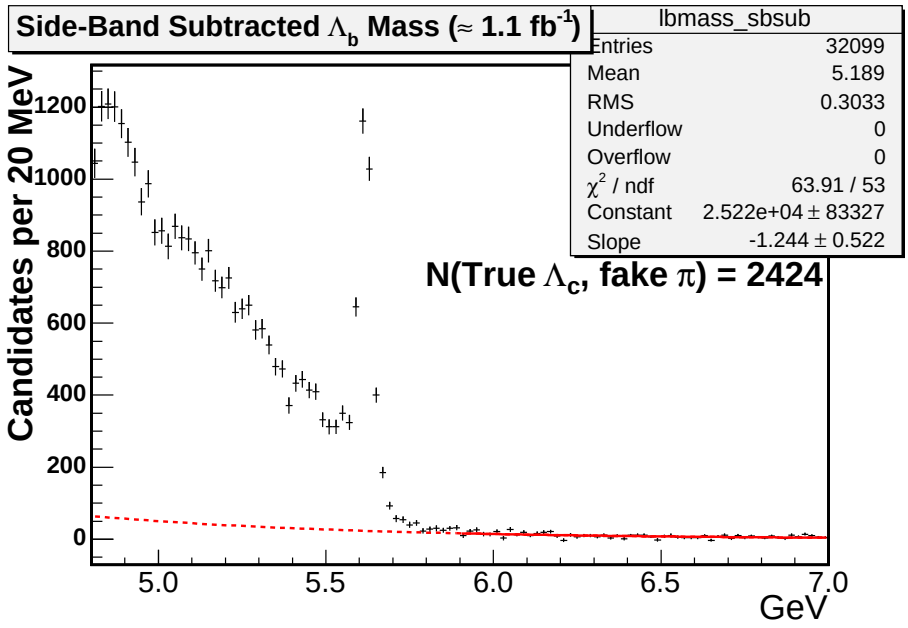

Figure 5.10: $m(\Lambda_c^+\pi)$ distribution for Λ_c^+ sideband subtracted data. The upper sideband of this distribution is fit with an exponential in order to estimate the number of true-Λ_c^+ , fake-π candidates we have.

7. $\Lambda_b^0 \to \Lambda_c^{+*}X$: The hadronic branching ratios used in the generation of the inclusive real Monte Carlo samples were, in many cases educated guesses. A more complete description of these branching fractions and the generation of the Monte Carlo sample can be found in [40]. Conservative branching ratio uncertainties for $\Lambda_b^0 \to \Lambda_c^{+*}X$ are $+150\%$ and -70% which, when we average positive and negative uncertainties, propagates to ± 0.21.

8. Λ_b^0 Four-Track: Similar to $\Lambda_b^0 \to \Lambda_c^{+*}$. We use a relative uncertainty of ± 0.005 which represents errors of $+100\%$ and -50% on the original branching ratios.

9. $\Lambda_b^0 \to \Sigma_c\pi$ and $\Lambda_b^0 \to \Sigma_c^*\pi$: Similar to $\Lambda_b^0 \to \Lambda_c^{+*}X$. We use a relative uncertainty of ± 0.17 which represents uncertainties of $+150\%$ and -70% in the original branching

ratios.

5.5.1.2 $\Lambda_b^0 \to \Lambda_c^+ \pi^-$ Mass Fit Results

Using the previously described background templates and constraints, we obtain the mass fit shown in Figure 4.1. The results of this binned, extended likelihood mass fit are shown in Table 5.1. The pulls from the constraints described above are listed in Table 5.2. The signal window is defined to be $m(\Lambda_c^+\pi^-) \in [5.565, 5.670]\mathrm{GeV/c^2}$. This choice was made to correspond to the bin boundaries closest to the signal mass mean position plus or minus three times the standard deviation of the signal distribution. Similarly, the upper sideband is defined to be $m(\Lambda_c^+\pi^-) \in [5.8, 7.0]\mathrm{GeV/c^2}$. The normalizations returned from the fit in the signal window are listed in Table 5.3.

Parameter	Fit Value	Error
$N_{\Lambda_b^0 \to \Lambda_c^+ \pi^-}$	3152	63
$N_{\Lambda_b^0 \to \Lambda_c^+ K^-}$	357	41
$N_{\Lambda_b^0 Four-Track}$	394	55
$N_{\Lambda_b^0 \to \ell \bar{\nu}_\ell X}$	3621	1043
$N_{\Lambda_b^0 \to \Lambda_c^+ \rho^-}$	1987	307
$N_{\Lambda_b^0 \to \Sigma_c^+ \pi^-}$	1256	185
$N_{\Lambda_b^0 \to \Lambda_c^{+*} X}$	838	187
$N_{\Lambda_b^0 `Other'}$	14734	1162
$N_{BFour-Track}$	1271	78
$N_{B \to \ell \bar{\nu}_\ell X}$	558	241
$N_{B `Other'}$	1050	989
$N_{Combinatorial}$	2160	94
$m(\Lambda_b^0)$	5.6135	0.0004

Table 5.1: Results of the binned Λ_b^0 mass fit on the entire fit range; from 4.8 to 7.0 GeV/c^2.

Constraint	Pull (χ^2)
Total Baryons	1.367
$\Lambda_b^0 \to \Lambda_c^+ K^+$	2.058
$\Lambda_b^0 \to \ell\bar{\nu_l}$	3.248
Λ_b^0 four-track	3.77
$\Lambda_b^0 \to \Lambda_c^{+*} X$	1.346
$\Lambda_b^0 \to \Lambda_c^+ \rho$	0.7058
$\Lambda_b^0 \to \Sigma_c \pi$	1.456
B four-track	4.545
$B \to \ell\bar{\nu_l}$	0.05638

Table 5.2: The χ^2 pulls on the mass fit constraints.

Normalization	Value
$N_{\Lambda_b^0 \to \Lambda_c^+ \pi^-}$	2904.9 ± 57.9 (82%)
$N_{BFour-Track}$	250.5 ± 15.4 (7%)
$N_{\Lambda_b^0 \to \Lambda_c^+ K^-}$	138.6 ± 15.9 (4%)
$N_{Combinatorial}$	116.2 ± 5.0 (3%)
$N_{\Lambda_b^0 Four-Track}$	113.7 ± 15.9 (3%)
$N_{\Lambda_b^0 \to \ell \bar{\nu}_\ell X}$	27.0 ± 7.8 ($< 1\%$)
$N_{\Lambda_b^0 `Other'}$	7.2 ± 6.8 ($< 1\%$)
$N_{B `Other'}$	3.5 ± 0.3
$N_{\Lambda_b^0 \to \Sigma_c^+ \pi^-}$	0.763917 ± 0.112236
$N_{B \to \ell \bar{\nu}_\ell X}$	0.643348 ± 0.27741
$N_{\Lambda_b^0 \to \Lambda_c^{+*} X}$	0.097919 ± 0.0217996
$N_{\Lambda_b^0 \to \Lambda_c^+ \rho^-}$	0.0265047 ± 0.00408758

Table 5.3: Normalizations for all backgrounds in the Λ_b^0 signal window $m(\Lambda_c^+ \pi^-) \in [5.565, 5.670] \mathrm{GeV/c^2}$.

5.5.2 $\Lambda_b^0 \to \Lambda_c^+\pi^-$ Lifetime Fit

Based on the mass fit results listed in Table 5.3, only 7 of the mass fit components contribute appreciably to the signal composition in the Λ_b^0 signal window. Therefore, the lifetime likelihood is composed of only 7 components; the $\Lambda_b^0 \to \Lambda_c^+\pi^-$ signal and 6 other backgrounds.

The $P^s_{\sigma_{ct}}$ and $P^b_{\sigma_{ct}}$ models are obtained from the data as described in Section 5.3. Both templates are shown overlaid in Figure 5.1 (Left).

The σ_{ct} dependence on the mass of the $\Lambda_c^+\pi^-$ candidate was investigated by separating the upper-sideband into two regions and comparing the σ_{ct} distribution from each. The result is shown in Figure 5.11. As a further check, the average ct and σ_{ct} for $m(\Lambda_c^+\pi^-)$ slices of the signal (Figure 5.12 and the upper-sideband (Figure 5.13) were computed. There is no evidence to suggest that there is any correlation between the σ_{ct} and $m(\Lambda_c^+\pi^-)$.

The $\Lambda_b^0 \to \Lambda_c^+\pi^-$ Monte Carlo sample described in Section 4.3.1 is used to compute the TTT efficiency, $\varepsilon^{\Lambda_b^0}_{TTT}(ct)$, for the Λ_b^0 components of the likelihood. Approximately $270,000$ events are used to compute the efficiency. The proper decay length distribution, and the derived TTT efficiency distribution are shown in Figure 5.14.

A separate efficiency, $\varepsilon^{B^0}_{TTT}(ct)$, is computed for the $B \to$ four track component of this fit using a Bgenerator sample of $B^0 \to D^+\pi^-$ decays reconstructed as $\Lambda_b^0 \to \Lambda_c^+\pi^-$. Approximately $80,000$ events are used to compute the efficiency. The proper decay length distribution and the derived B^0 TTT efficiency are shown in Figure 5.15. For comparison, the Λ_b^0 and B^0 efficiencies are shown overlaid in Figure 5.16.

Only the signal region is used when fitting for the lifetime. In some lifetime fits, the upper sideband is included explicitly, and the parametric shape of the combinatorial background is allowed to float in a combined signal plus sideband region fit. We chose not to follow this approach in favor of a less complicated, faster fit. We have studied changes to the shape of the combinatorial background along the *ct* axis. Since the ratio of the Λ_b^0 signal to combinatorial background in the signal region is about $30:1$, the shape of the combinatorial background lifetime has sub-micron influence on the final lifetime fit (*i.e.*, on the order of $0.2-0.3$ μm), and is therefore negligible.

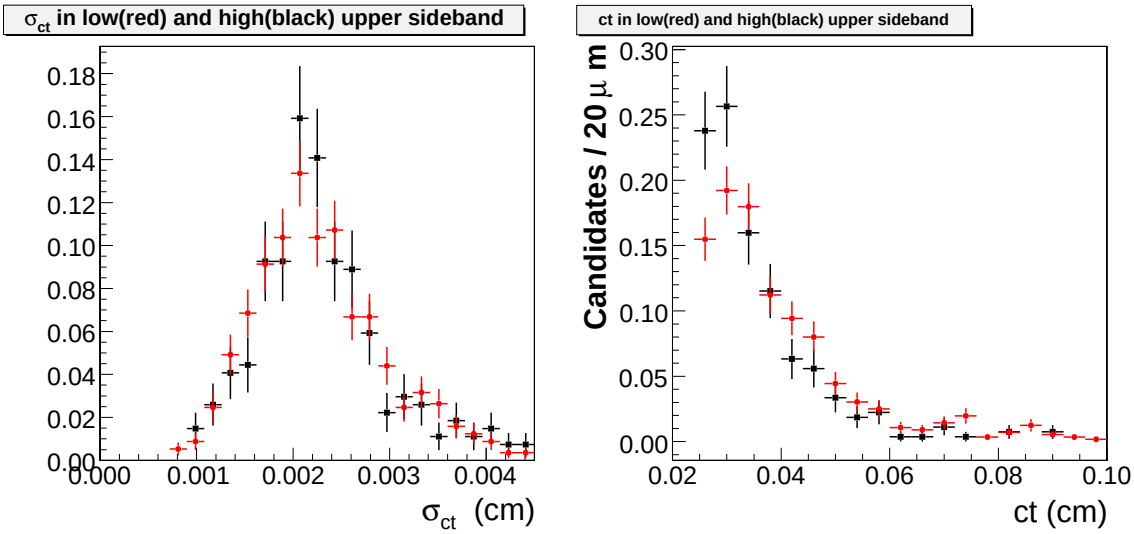

Figure 5.11: Left: comparison of σ_{ct} distribution for two regions of the upper-sideband (pure combinatorial background): $m(\Lambda_c^+\pi^-) \in [5.8, 6.5]$ GeV$/c^2$(red) and $m(\Lambda_c^+\pi^-) \in [6.5, 7.0]$ GeV$/c^2$(black). There is no evidence for any dependence of σ_{ct} in the combinatorial background on $m(\Lambda_c^+\pi^-)$. Right: comparison of *ct* for the same two regions of the upper sideband. The low-mass region (red points) (*i.e.*, the region nearest to the $\Lambda_b^0 \to \Lambda_c^+\pi^-$ mass peak) differs slightly from the high-mass region (black points). The low-mass region is however larger in terms of the overall normalization, so the modeling of the *ct* shape of the background underneath the $\Lambda_b^0 \to \Lambda_c^+\pi^-$ main mass peak is not very affected. The effect on the blinded fit due to changes of the background shape is at the sub-micron level.

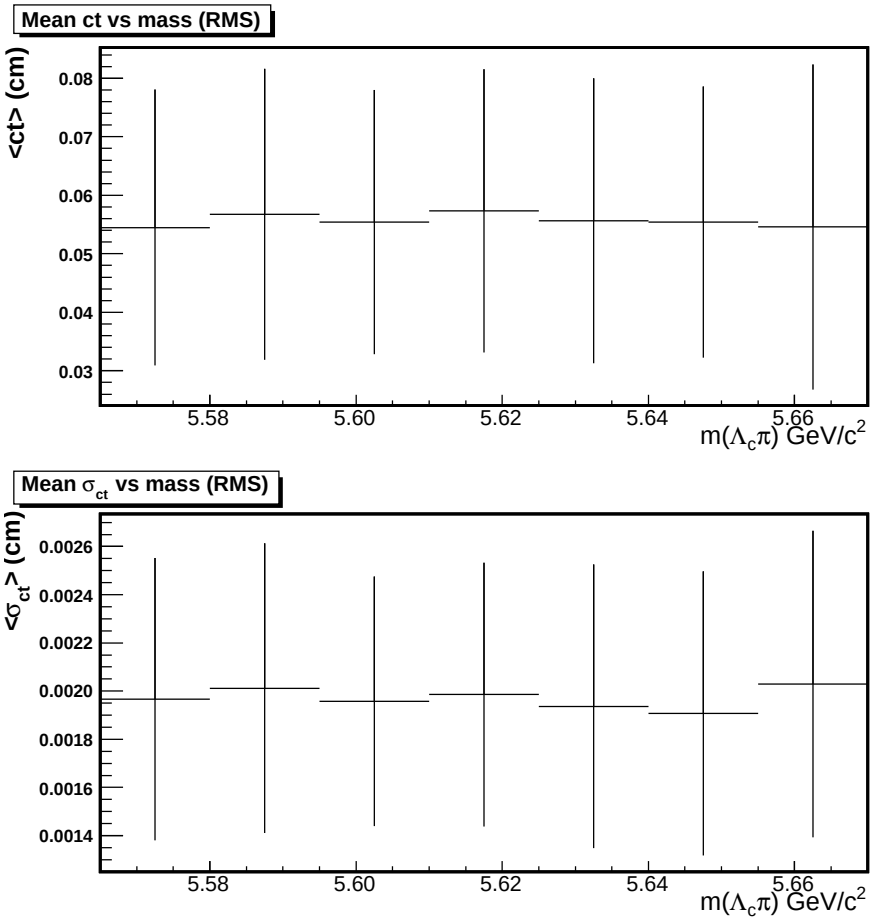

Figure 5.12: Profile histograms of ct and σ_{ct} in slices of $m(\Lambda_c^+\pi^-)$ in the signal window. The points on both figures represent the average of ct (σ_{ct}) for each mass slice, and the error is the RMS of the distribution. RMS is used in order to indicate the shape of the distribution which is, by nature a two dimensional distribution.

The general form of the likelihood used in the lifetime fit is given in Equation 5.2. The normalizations used for each component are those listed in Table 5.3. The P_{ct} and $P_{\sigma_{ct}}$ distributions for each component of the fit are described below.

1. $\Lambda_b^0 \to \Lambda_c^+\pi^-$ Signal. Comprised of Λ_b^0 events that decay into Λ_c^+ and a pion, with the Λ_c^+ decaying (eventually) into a proton, a pion and a kaon.

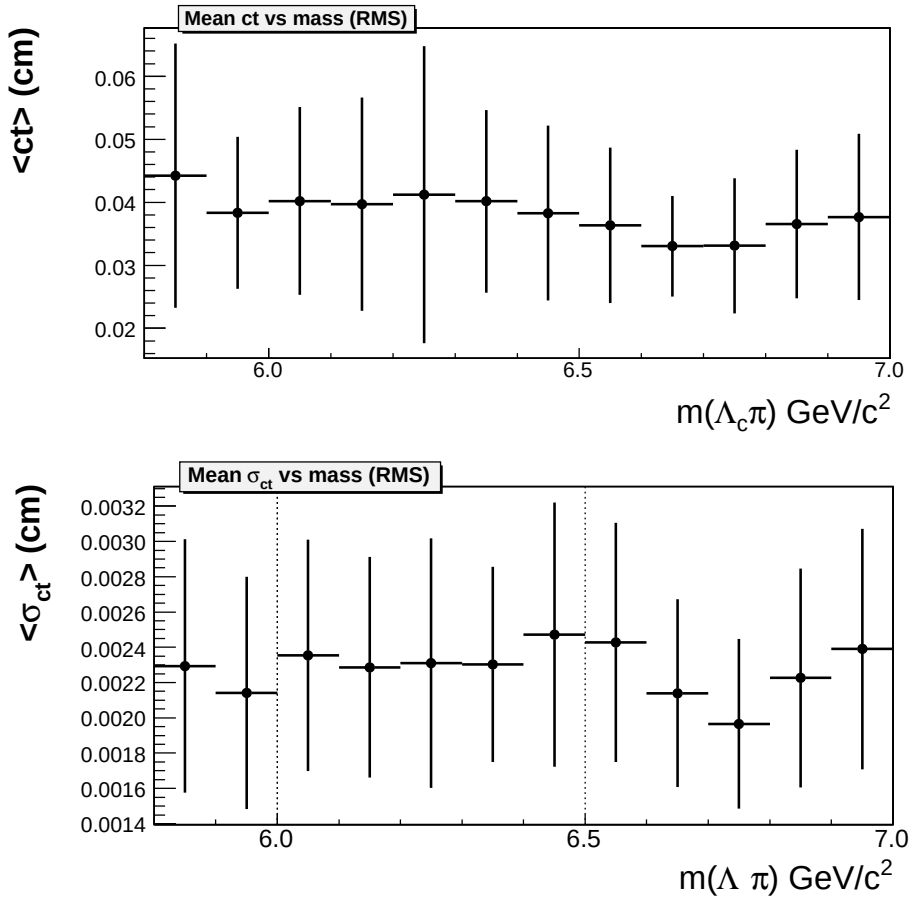

Figure 5.13: Profile histograms of ct and σ_{ct} in slices of $m(\Lambda_c^+\pi^-)$ in the upper-sideband. The points on both figures represent the average of ct (σ_{ct}) for each mass slice, and the error is the RMS of the distribution.

- P_{ct}^1: The parametric proper decay length model described in Section 3.2;

$$P_{ct}^1(ct|\sigma_{ct}) = exp(ct, c\tau) \otimes R(ct, \sigma_{ct}) \cdot \varepsilon_{TTT}^{\Lambda_b^0}(ct).$$

  The Λ_b^0 lifetime, τ, is the only parameter left floating in the lifetime fit.

- $P_{\sigma_{ct}}^1$: $P_{\sigma_{ct}}^s$ from sideband-subtracted data.

2. $\underline{B \rightarrow \text{four tracks}}$: Comprised of B meson events (excluding semi-leptonic B decays and those covered by the "other B decay" component described below) that decay

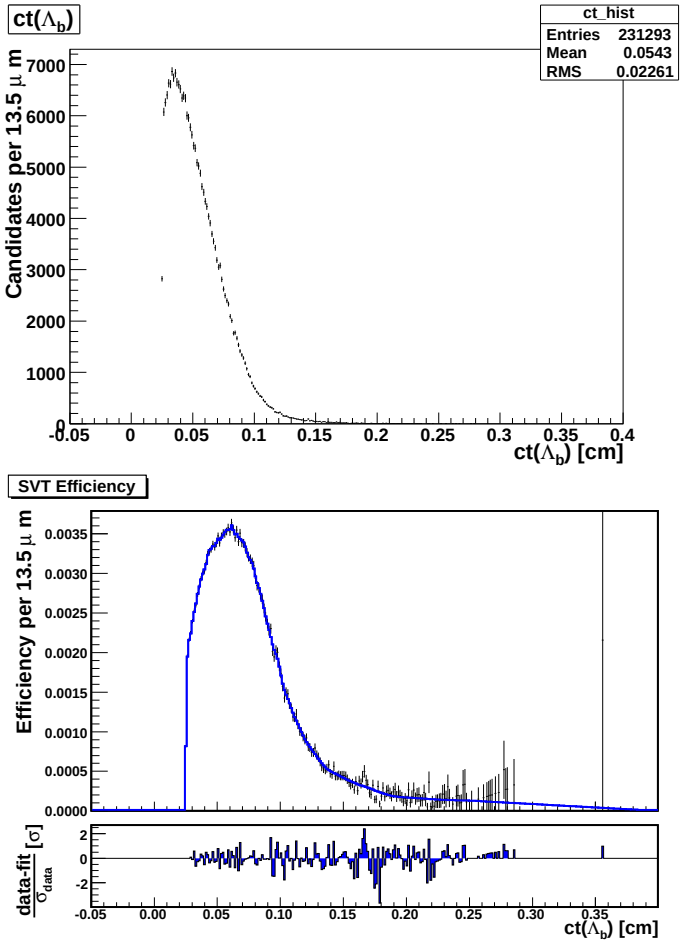

Figure 5.14: Top: the *ct* distribution for $\Lambda_b^0 \to \Lambda_c^+\pi^-$ HQGen Monte Carlo after trigger and analysis cuts have been applied. Bottom: The Λ_b^0 TTT efficiency distribution, $\varepsilon_{TTT}^{\Lambda_b^0}(ct)$ computed applying Equation 3.9 to the HQGen sample described in Section 4.3.1.

into exactly four charged stable daughters and exactly zero neutral stable daughters.

- P_{ct}^2: The same parametric model used to model the Λ_b^0 signal is also used here with a slight modification. When reconstructing a candidate, it is assumed that we have a true Λ_b^0 decay and $m(\Lambda_b^0)$ is used to compute the candidate's *ct*. On an event-by-event basis, we don't know if we are reconstructing a true Λ_b^0 or *B* decay and all events get *ct* computed using the Λ_b^0 mass. To compute the

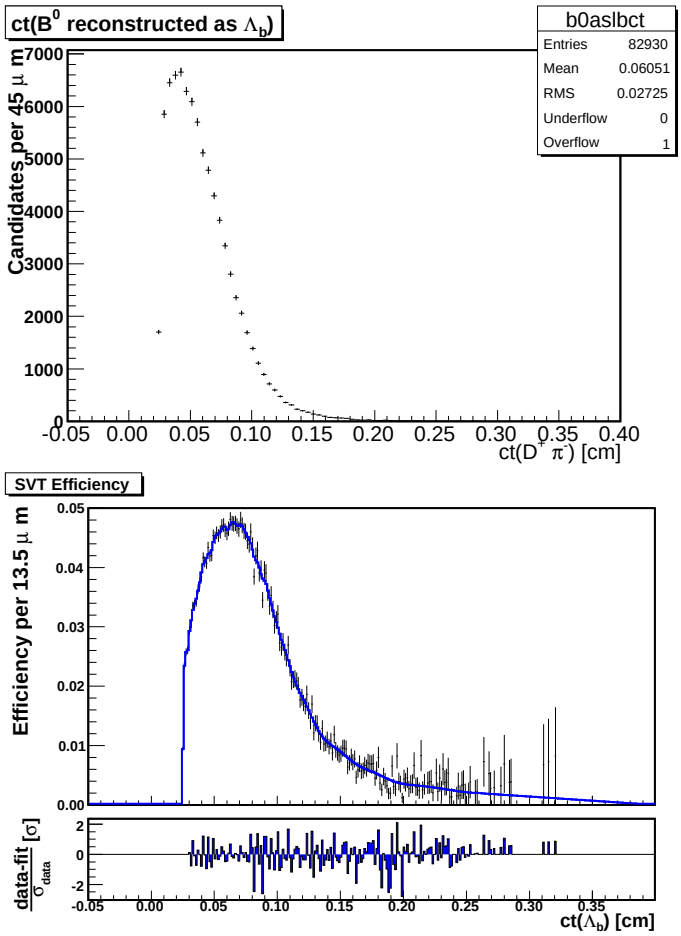

Figure 5.15: Top: the *ct* distribution for B-Generator $B^0 \to D^+\pi^-$ reconstructed as $\Lambda_b^0 \to \Lambda_c^+\pi^-$, $\varepsilon_{TTT}^{B^0}(ct)$, after trigger and analysis cuts have been applied. Bottom: The Λ_b^0 TTT efficiency distribution computed applying Equation 3.9.

correct *ct* for a true B^0, one needs to use the correct B^0 mass. Therefore, in place of the Λ_b^0 lifetime, in the PDF, we make the following substitution;

$$\tau \to \tilde{\tau} = \frac{m(\Lambda_b^0)}{m(B^0)} \cdot \tau_{B^0}.$$

The B^0 lifetime is fixed to the value from the PDG [8], and scaled by the ratio of Λ_b^0 to B^0 masses to correct for the Λ_b^0 mass hypothesis used when incorrectly

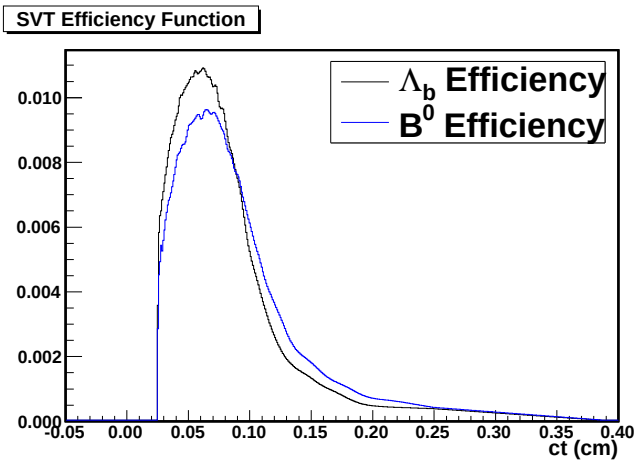

Figure 5.16: The Λ_b^0 and B^0 efficiencies shown super-imposed on one another for comparison.

reconstructing a true B decay as a Λ_b^0.

$$P_{ct}^2(ct|\sigma_{ct}) = exp(ct, c\tilde{\tau}) \otimes R(ct, \sigma_{ct}) \cdot \varepsilon_{TTT}^{B^0}(ct).$$

- $P_{\sigma_{ct}}^2$: $P_{\sigma_{ct}}^s$ from sideband-subtracted data.

3. Cabibbo suppressed, $\Lambda_b^0 \to \Lambda_c^+ K^-$ Comprised of Λ_b^0 events that decay to Λ_c^+ and a kaon, with the Λ_c^+ eventually decaying to a proton, a pion and a kaon.

   - P_{ct}^3: These are pure Λ_b^0 decays and therefore use a model identical to the signal.
   - $P_{\sigma_{ct}}^3$: $P_{\sigma_{ct}}^s$ from sideband-subtracted data.

4. Combinatorial Background: Comprised of Λ_b^0 candidates reconstructed with a true Λ_c^+ and a fake pion.

   - P_{ct}^4: The lifetime shape is derived directly from candidates in the upper sideband ($5.8 < m(\Lambda_c^+\pi^-) < 7.0$) of data. The candidates are fit with a Landau distribu-

tion, as shown in Figure 5.17 (Left). The model is manually set to zero for proper times less than $0.025cm$ to mimic the analysis cut, $ct(\Lambda_b^0) > 0.025cm$. The resulting model for P_{ct}^4 is shown in Figure 5.17 (Right).

- $P_{\sigma_{ct}}^4$: $P_{\sigma_{ct}}^b$ from the upper-sideband of data.

5. $\underline{\Lambda_b^0 \rightarrow \text{four tracks}}$: Comprised of Λ_b^0 events (excluding $\Lambda_b^0 \rightarrow \Lambda_c^+\pi^-$, $\Lambda_b^0 \rightarrow \Lambda_c^+K^-$, and Λ_b^0 semi-leptonic decays) that decay into exactly four charged stable daughters and exactly zero neutral stable daughters.

   - P_{ct}^5: These are again pure Λ_b^0 decays and therefore use the same model as the signal.

   - $P_{\sigma_{ct}}^5$: $P_{\sigma_{ct}}^s$ from sideband-subtracted data.

6. $\underline{\Lambda_b^0 \rightarrow l\bar{\nu}_l X}$: Λ_b^0 events that have a stable lepton (an e or a μ as opposed to a τ) as one of the direct daughters.

   - P_{ct}^6: The smoothed histogram shown in Figure 5.18 (Left), used to model this background is derived from inclusive realistic Monte Carlo. No special attention is given to the loss of momentum associated with the un-detected neutrino in these decays. For the lifetime fit, only events in the signal mass window, near the Λ_b^0 mass peak are considered. Neutrinos from these decays carry almost no momentum and their effect can be neglected.

   - $P_{\sigma_{ct}}^6$: $P_{\sigma_{ct}}^s$ from sideband-subtracted data.

7. Other Λ_b^0 Decays: All Other Λ_b^0 events that are not already included in another template.

   - P_{ct}^7: The smoothed histogram shown in Figure 5.18 (Right) is derived from inclusive realistic Monte Carlo.

   - $P_{\sigma_{ct}}^7$: $P_{\sigma_{ct}}^s$ from sideband-subtracted data.

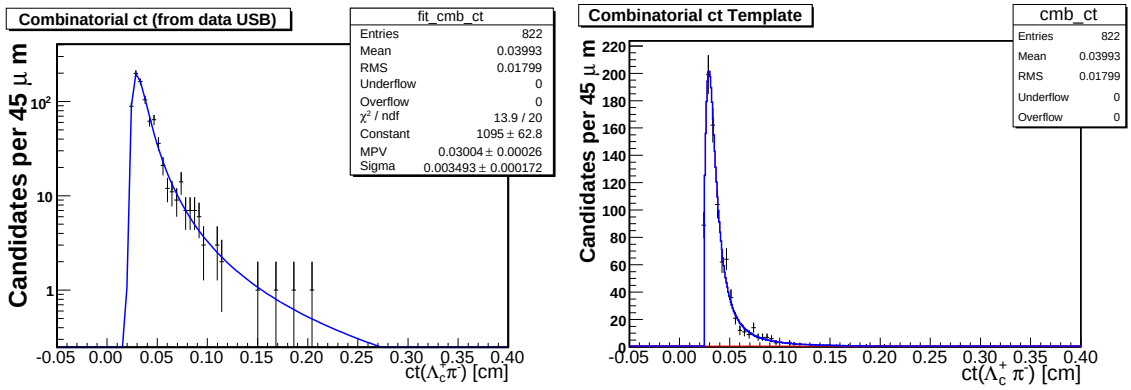

Figure 5.17: Left: The Landau fit to candidates in the upper sideband of data. The fit probability is 0.835. The model is manually set to zero for $ct < 0.025$ cm. The resulting combinatorial *ct* template is shown on the Right.

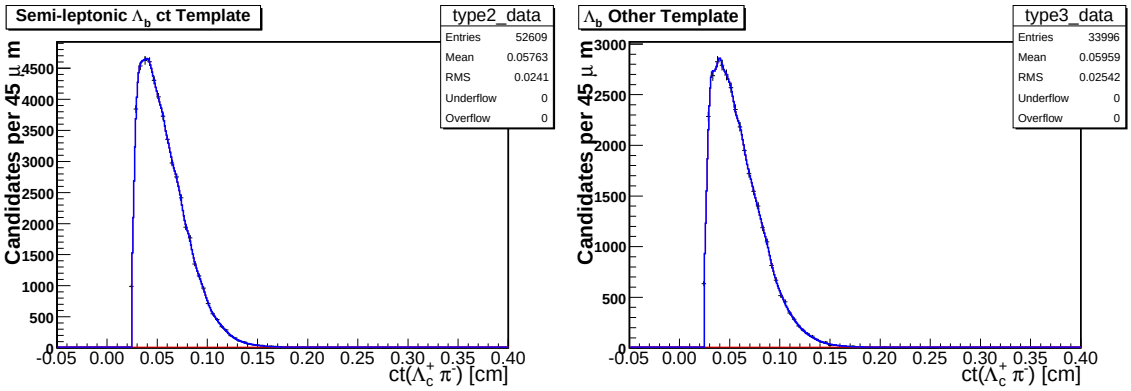

Figure 5.18: Left: Λ_b^0 semi-leptonic *ct* template. Right: Other Λ_b^0 decays *ct* template.

5.5.3 Lifetime Fit Cross-Check I: Toy Monte Carlo

With all of the fit templates and lifetime likelihood ingredients in place, we can test the fitter using Toy Monte Carlo. Toy Monte Carlo samples are generated by sampling the total lifetime probability distribution function to generate distributions for each of the fit variables (in our case ct and $\sigma_{ct}\dot{}$Toy Monte Carlo allows one to quickly generate similar but statistically independent datasets. Toy generation is performed using RooFit's "Accept/Reject" method using the distributions of our combined likelihood as input. Events for ct, and σ_{ct} are generated separately by RooFit's Accept/Reject method using the following algorithm.

1. Start by finding the maximum, $y_{\max}$, of the PDF in a given variable by random sampling.

2. a number,x, from the domain of the variable is generated using a uniform distribution.

3. a uniform random number $r \in [0, y_{\max}]$ is generated.

4. if $PDF(x) > r$, x is accepted; otherwise it is rejected.

The same Toy generation method is used to evaluate the impact of systematic errors as described in Section 7.

To test the stability of the Λ_b^0 lifetime fit, 500 Toy experiments of ~ 3700 events (statistics similar to those found in the signal window of data) were generated and fit. In each case, signal and background components were generated in the same proportion as that observed in data (see Section 6. Toy data were generated using Λ_b^0 lifetimes of 350.0, 400.0,

450.0, and 500.0μm. In all cases, the Toy fit results are consistent with the input lifetime, with pulls consistent with 1.0. The distributions are given in Figures 5.19 through 5.22.

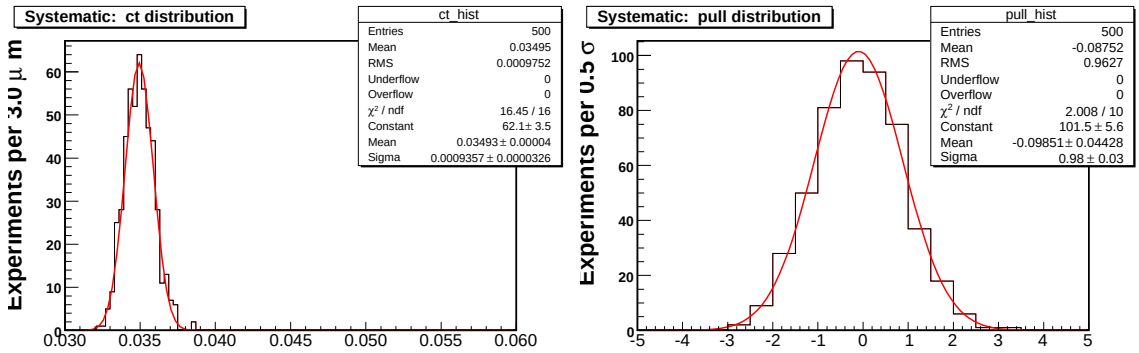

Figure 5.19: Left:The distribution of lifetime fit results on Toy Monte Carlo samples. The Toy was generated with a lifetime of $c\tau(\Lambda_b^0) = 350.0\mu$m. Right:The pull distribution from the Toy fits. The pull is defined as (input - measured)/error. The result shows a small deviation from a mean of 0 and has a width consistent with 1.

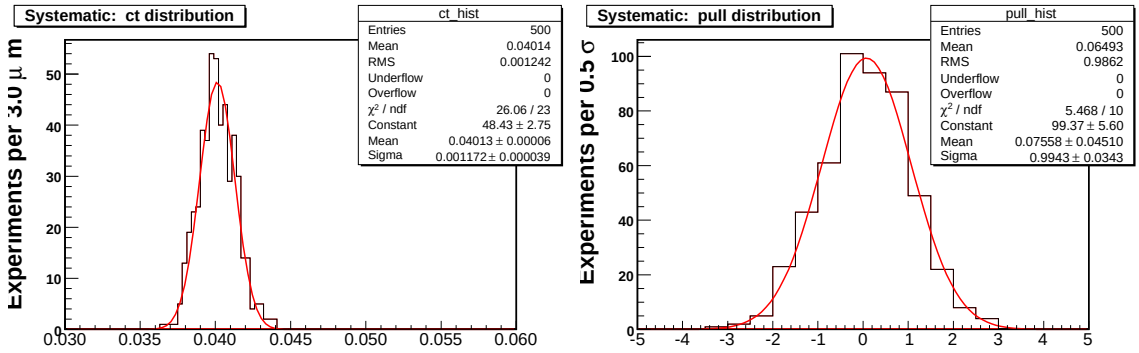

Figure 5.20: Left:The distribution of lifetime fit results on Toy Monte Carlo samples. The Toy was generated with a lifetime of $c\tau(\Lambda_b^0) = 400.0\mu$m. Right:The pull distribution from the Toy fits. The pull is defined as (input - measured)/error. The result shows a small deviation from a mean of 0 and has a width consistent with 1.

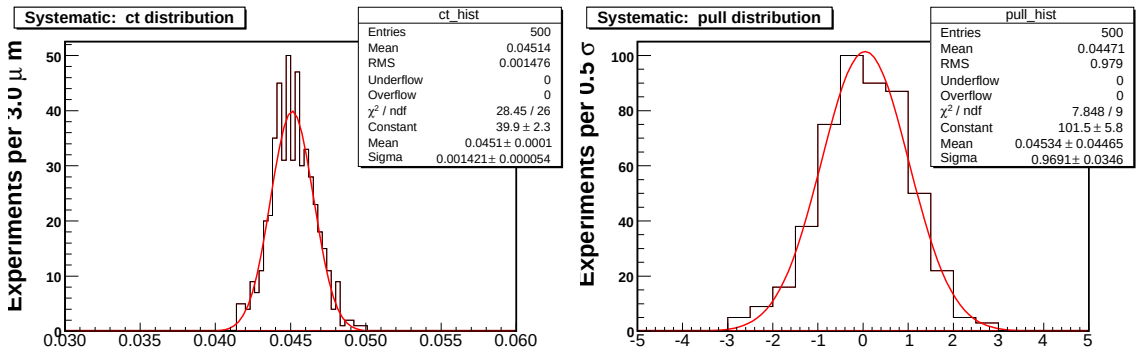

Figure 5.21: Left:The distribution of lifetime fit results on Toy Monte Carlo samples. The Toy was generated with a lifetime of $c\tau(\Lambda_b^0) = 450.0\mu$m. Right:The pull distribution from the Toy fits. The pull is defined as (input - measured)/error. The result shows a small deviation from a mean of 0 and has a width consistent with 1.

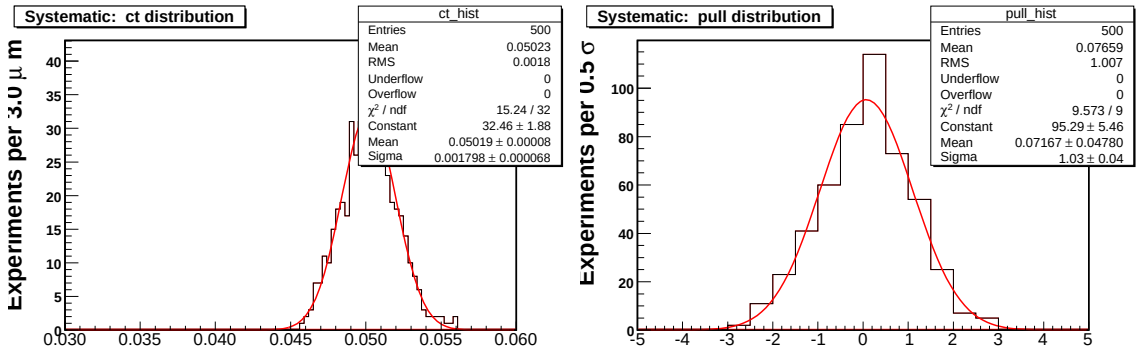

Figure 5.22: Left:The distribution of lifetime fit results on Toy Monte Carlo samples. The Toy was generated with a lifetime of $c\tau(\Lambda_b^0) = 500.0\mu$m. Right:The pull distribution from the Toy fits. The pull is defined as (input - measured)/error. The result shows a small deviation from a mean of 0 and has a width consistent with 1.

5.5.4 Lifetime Fit Cross-Check II: Realistic Signal Monte Carlo

As a second check of the Λ_b^0 lifetime fit, one can fit realistic Monte Carlo samples. The large Monte Carlo sample that is used to compute the TTT efficiency provides a good circular check of the fit. Because the sample is so large, the statistical error on the fit result is very small making the cross-check very sensitive.

Additionally, two smaller Monte Carlo samples were generated with $c\tau'(\Lambda_b^0)$ equal to 325 and 500μm. These samples were re-weighted to match the data using the same method described in Section 4.3.1. After re-weighting, the 325μm and 500μm samples consist of around $22,500$ and $31,500$ events respectively.

By using three independent Monte Carlo samples, with different Λ_b^0 lifetimes, one can probe the sensitivity of the fitting method to the value of the input Monte Carlo lifetime. The expectation, from previous lifetime analyses [1] is that the efficiency should be independent of the lifetime of the Monte Carlo from which it is derived.

The lifetime fit on signal Monte Carlo is much simpler than the fit on real data because it only includes signal events. The fit likelihood consists of one, signal component;

$$\mathcal{L}(ct,\sigma_{ct}) = P^1_{ct}(ct|\sigma_{ct}) \cdot P^s_{\sigma_{ct}}(\sigma_{ct}) \cdot \varepsilon_{TTT}(ct).$$

Because there are no backgrounds competing with the signal events, the signal mass window is relaxed slightly to $m(\Lambda_c^+\pi^-) \in [5.54,5.72]\mathrm{GeV/c^2}$ to include nearly all of the available events.

$P^s_{\sigma_{ct}}$ is obtained from the σ_{ct} distribution in the signal mass window for each of the three samples (Figure 5.23). Similarly, an TTT efficiency is computed from each Monte Carlo sample using Equation 3.9 where $c\tau^{MC}$ corresponds to the Λ_b^0 lifetime with which the sample was generated. The efficiency computed from the $ct(\Lambda_b^0) = 368\mu$m sample is the default efficiency used when fitting the data. The efficiencies from each sample are shown in Figure 5.24 and shown overlaid in Figure 5.25.

Using the three Monte Carlo samples and the three TTT efficiency functions, the 9 possible lifetime fit combinations are constructed and executed. The results of each fit are given in Table 5.4 and shown graphically in Figure 5.26. In all cases, the fits are consistent with the generated Monte Carlo values. The largest exceptions are seen when fitting the 368μm sample. Because this sample is so large, the statistical error in each fit is very small. The 325 and 500μm TTT efficiencies are generated from much fewer events than 368μm. Because they are based on fewer events, these models describe the underlying physics less accurately than the efficiency generated from more events. When used to fit the smaller, 325 and 500μm samples, even the low statistics models provide an accurate fit. When applied to the large 368μm sample though, the shortcomings of the model are accentuated resulting in fit results that are further from the generated lifetime than in the other samples.

Most importantly, the fits using the TTT model based on the 368μm sample return values for $ct(\Lambda_b^0)$ that are consistent with the generated value in all cases. The lifetime fit projections to the 325, 368, and 500μm samples, using the default, 368μm efficiency are shown in Figure 5.27. The results based on the 368μm efficiency are also shown in Figure

5.28. This cross-check demonstrates that the default TTT efficiency distribution serves as a sufficient model over the range of values where we expect to measure $c\tau(\Lambda_b^0)$.

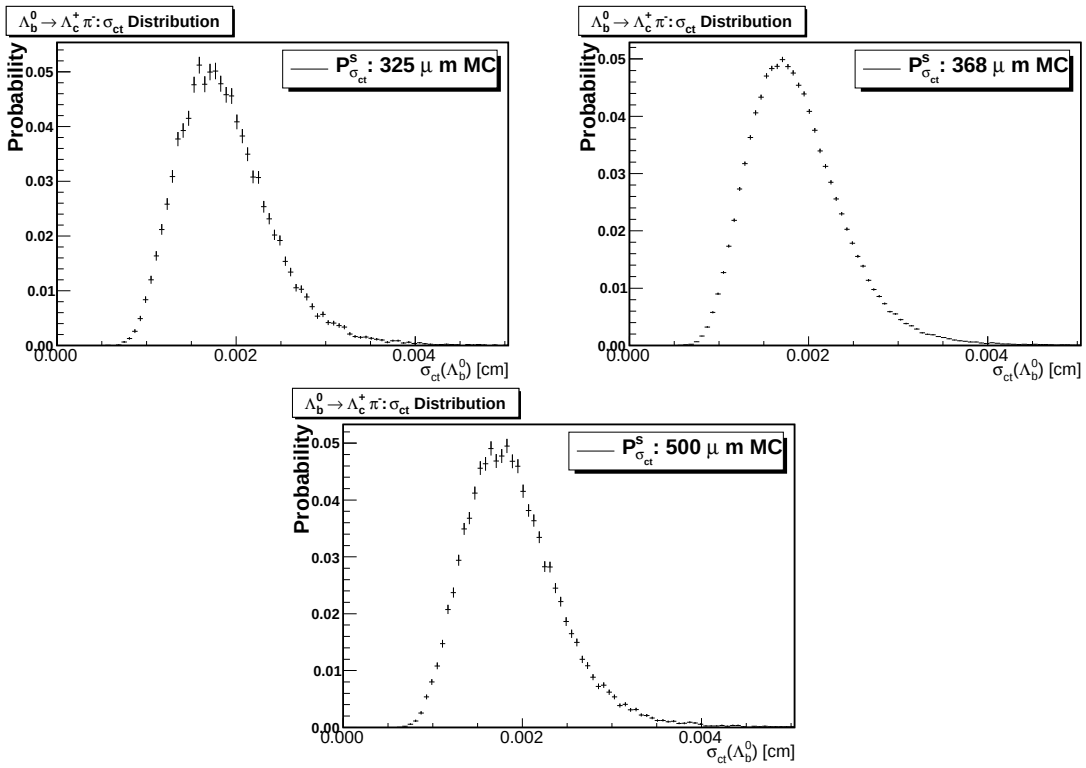

Figure 5.23: Distribution of σ_{ct} in the signal window from the realistic Monte Carlo samples; 325μm (top Left), 368μm (top Right), and 500μm (bottom). This distribution of errors is $P^S_{\sigma_{ct}}$ in the signal Monte Carlo likelihood.

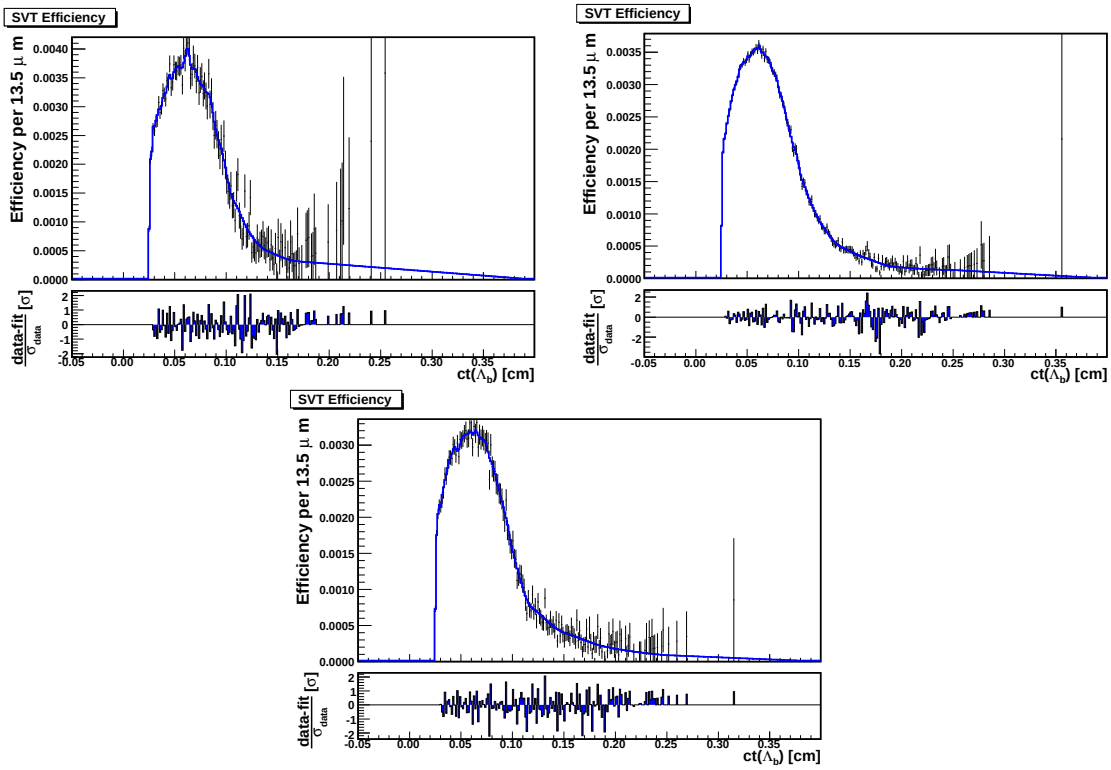

Figure 5.24: The TTT efficiency distributions, $\varepsilon_{TTT}(ct)$, obtained from the three realistic Monte Carlo samples; 325μm (top Left), 368μm (top Right), and 500μm (bottom).

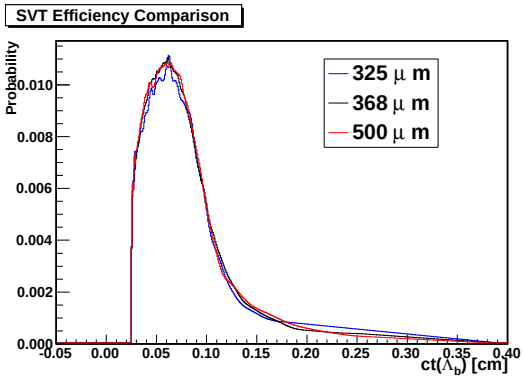

Figure 5.25: The TTT efficiency distributions from Figure 5.24 shown overlaid. The Blue, Black, and Red curves correspond to efficiencies computed from the 325, 368, and 500μm samples respectively.

Input Sample	**Fit Model**	**Fit Result**
325μm	325μm	328.3 $\pm$ 3.3μm
	368μm	326.9 $\pm$ 3.3μm
	500μm	329.3 $\pm$ 3.4μm
368μm	325μm	371.1 $\pm$ 1.2μm
	368μm	368.7 $\pm$ 1.2μm
	500μm	372.8 $\pm$ 1.2μm
500μm	325μm	495.0 $\pm$ 5.4μm
	368μm	497.6 $\pm$ 5.4μm
	500μm	500.8 $\pm$ 5.4μm

Table 5.4: Comparison of fit results on HQGen Monte Carlo samples generated with $c\tau'(\Lambda_b^0)$ = 325, 368 and 500μm. Efficiency distributions are calculated from each of the three samples to create three unique fit models. Each sample is then fit three times; once with the TTT efficiency obtained from the 325μm sample, again with the default efficiency calculated from the 368μm sample, and finally with the efficiency derived from the 500μm sample. The results show that the measured $c\tau(\Lambda_b^0)$ is independent of the lifetime used to generate the Monte Carlo from which the efficiency is calculated.

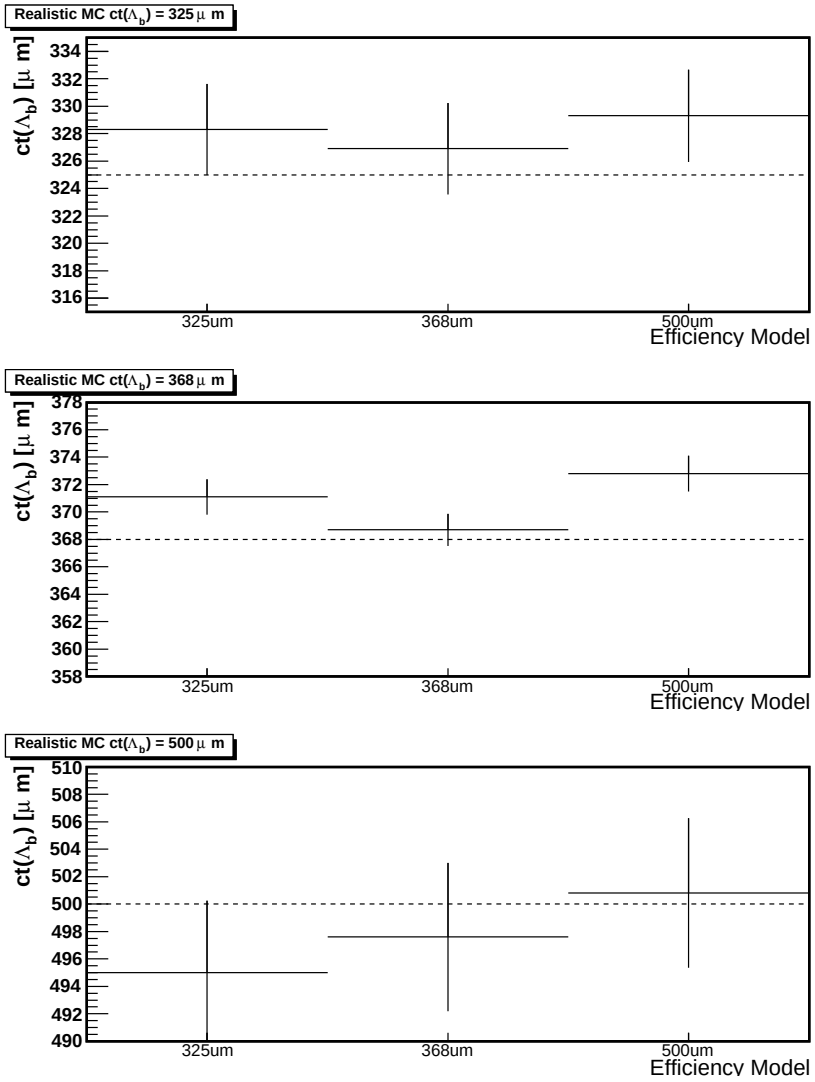

Figure 5.26: Graphical representation of the fit results listed in Table 5.4. Each panel represents the fits to a realistic Monte Carlo sample with a given Λ_b^0 lifetime (shown by the dashed horizontal line). The *x*-axis of each panel shows the TTT efficiency model that is used when fitting. The error shown on each fit point represents the statistical error returned by the fit.

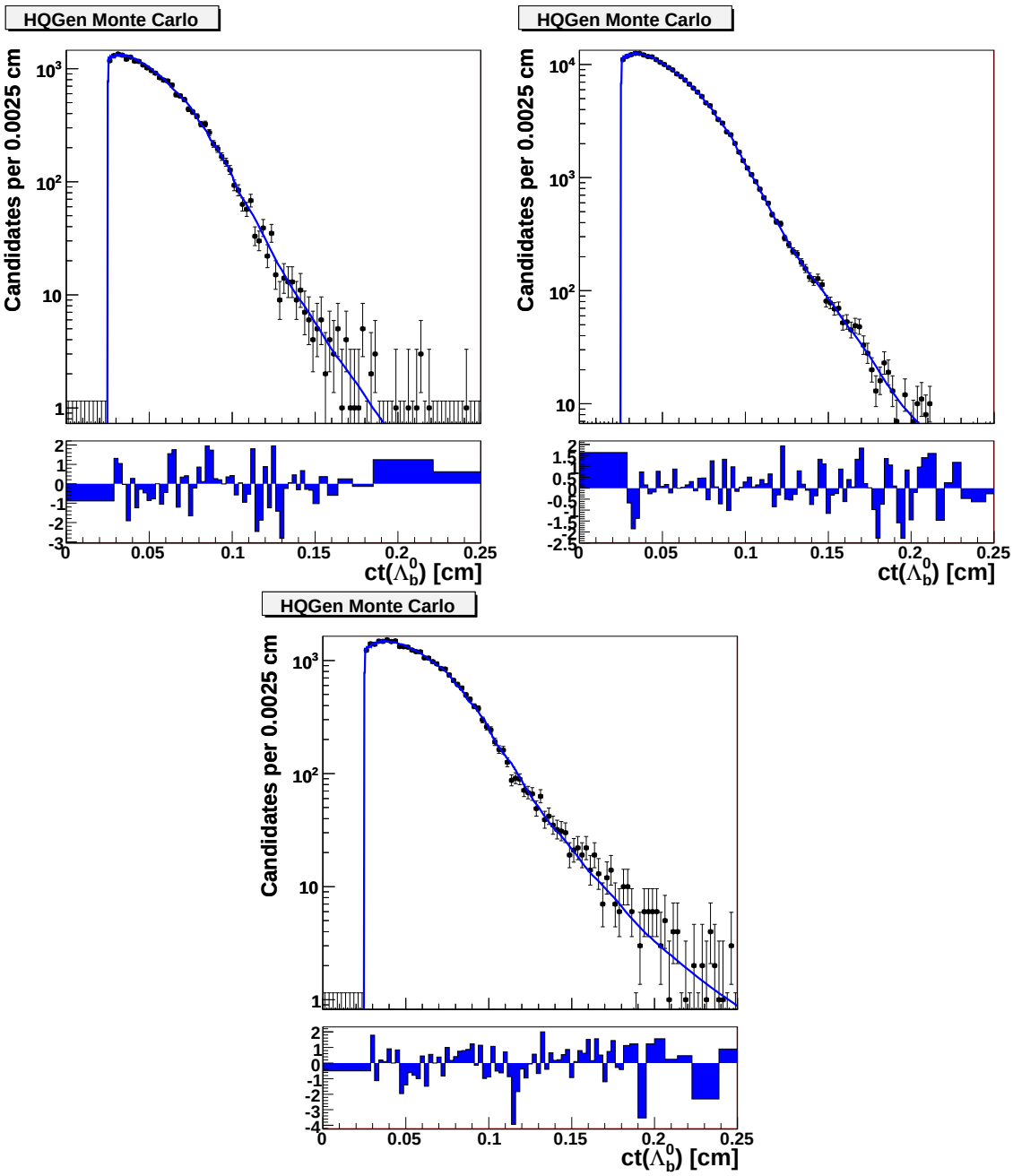

Figure 5.27: Signal Monte Carlo lifetime fit projections when fit with the TTT efficiency computed using the 368μm Monte Carlo. The fits to 325 (top Left), 368 (top Right), and 500μm (bottom) realistic Monte Carlo samples are shown.

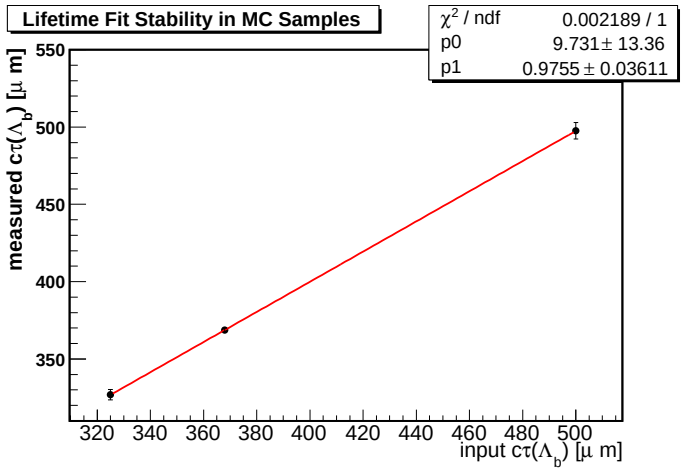

Figure 5.28: Lifetime fit results based on the default, 368μm efficiency. The *x*-axis shows the generated lifetime of the sample being fit. The *y*-axis shows the measured lifetime. The slope is consistent with 1 and indicates no bias over the nearly 200μm region tested.

5.5.5 Lifetime Fit Cross-Check III: Trigger Codes

As a third, and more important, cross check of the Λ_b^0 lifetime fit, we fit different parts of the $c\tau'(\Lambda_b^0) = 368\mu$m realistic signal Monte Carlo sample based on the pairs of stable tracks that satisfy the requirements of the TTT. This check is particularly powerful because it exercises our fit method (in particular the generation of the trigger efficiency) in decays with very different kinematics.

For this cross-check, the large realistic $\Lambda_b^0 \to \Lambda_c^+\pi^-$ Monte Carlo sample is used. The events are required to only satisfy the trigger and analysis cut requirements. None of the reweighting described in Section 4.3.1 is applied in order to maximize statistics.

In a $\Lambda_b^0 \to \Lambda_c^+\pi_2^-; \Lambda_c^+ \to p^+K^-\pi_1^+$ decay, there are four stable tracks that may satisfy the reqiurements of the two displaced track trigger in pairs. For each event, all possible pairs of stable tracks are tested to determine if the requirements of the TTT are met. If a given track-pair satisfies the trigger, a bit is set. More than one track-pair may satisfy the trigger in a given event. The `trigCode` is the value obtained when all confirmed track pair bits are anded together. The resulting set of possible trigger codes, track-pair bits, and the abundance of each trigger code in the Monte Carlo is summarized in Table 5.5.

Because many of the trigger codes have very few events, we decide to consider only the six distinct types listed in Table 5.6. For each of the six `trigCodes`, a separate efficiency is computed using the prescription outlined in Section 3.3. The efficiency for each `trigCode` is shown in Figures 5.29 through 5.31. The efficiency for each `trigCode` are also overlaid for comparison in Figure 5.32.

Code	Bits	Description	N events
1	00001	pK	65,419
2	00010	$K\pi_1$	8,014
3	00011	$pK + K\pi_1$	3,431
8	01000	$p\pi_1$	569,215
9	01001	$p\pi_1 + pK$	70,639
10	01010	$p\pi_1 + K\pi_1$	128
11	01011	$p\pi_1 + pK + K\pi_1$	372
16	10000	$\pi_1\pi_2$	40,493
17	10001	$\pi_1\pi_2 + pK$	52
18	10010	$\pi_1\pi_2 + K\pi_1$	6,346
19	10011	$\pi_1\pi_2 + pK + K\pi_1$	56
24	11000	$p\pi_1 + \pi_1\pi_2$	38,175
25	11001	$p\pi_1 + \pi_1\pi_2 + pK$	2,903
26	11010	$p\pi_1 + \pi_1\pi_2 + K\pi_1$	1,122
27	11011	$p\pi_1 + \pi_1\pi_2 + pK + K\pi_1$	4,032

Table 5.5: Definition of `trigCodes`; pairs of tracks that satisfy the requirements of the Two Track Trigger.

The signal Monte Carlo lifetime fit is performed in each `trigCode` sample using the corresponding efficiency function. The resulting $ct(\Lambda_b^0)$ from each fit is plotted in Figure 5.33. The result of each fit is consistent with the generated lifetime of $c\tau(\Lambda_b^0) = 368.0\mu$m.

The `trigCode` cross-check is an important verification that our method is robust across various kinematic situations. The check also builds confidence that the fit to data will be correct. As described in Section 4.3.1, the HQGen Monte Carlo sample is re-weighted such that the `trigCode` distribution matches that observed in sideband-subtracted data. Because the independent `trigCode` lifetime fits in Monte Carlo are consistent with the generated lifetime value, we can be confident that the combined efficiency, based on the re-weighted Monte Carlo, is an accurate representation of the decay kinematics present in Data and will give an accurate value for the Λ_b^0 lifetime.

Code	Description	N events
1	pK	$65,419$
8	$p\pi_1$	$569,215$
9	$p\pi_1 + pK$	$70,639$
16	$\pi_1\pi_2$	$40,493$
24	$p\pi_1 + \pi_1\pi_2$	$38,175$
99	All other combinations	$26,456$

Table 5.6: Because the statistics in several of the `trigCode` categories is low, only six categories are used in the cross-check.

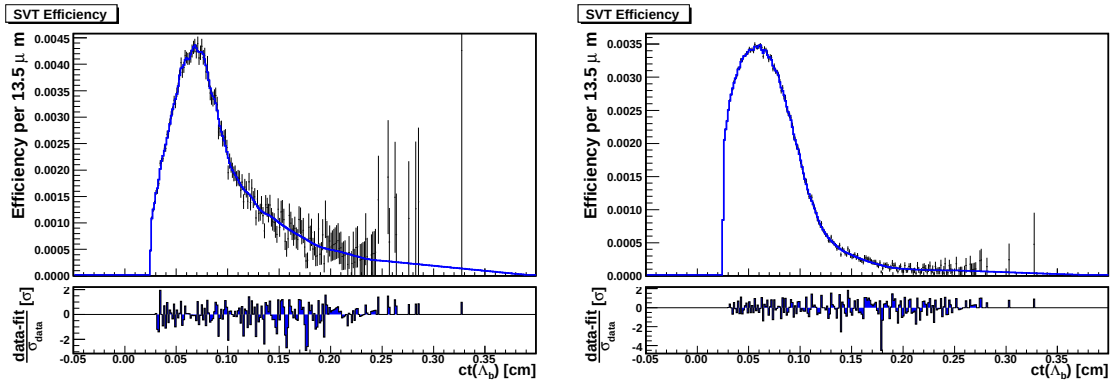

Figure 5.29: TTT efficiencies generated for trigger codes 1 (Left) and 8 (Right).

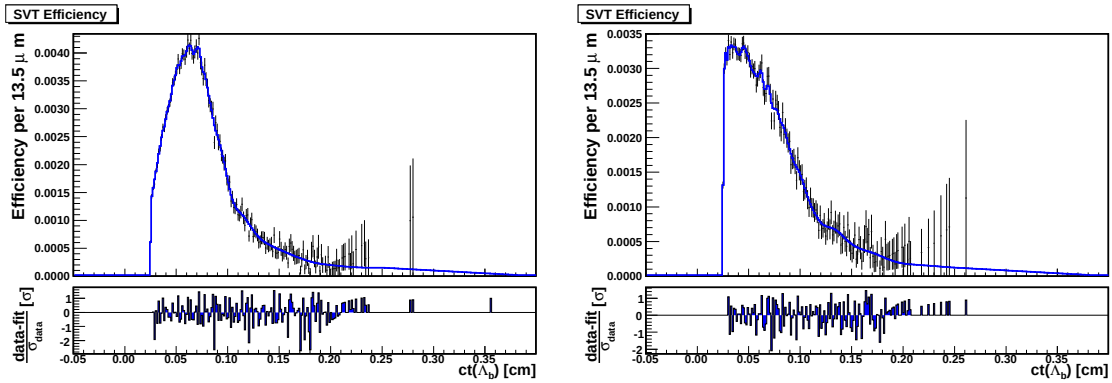

Figure 5.30: TTT efficiencies generated for trigger codes 9 (Left) and 16 (Right).

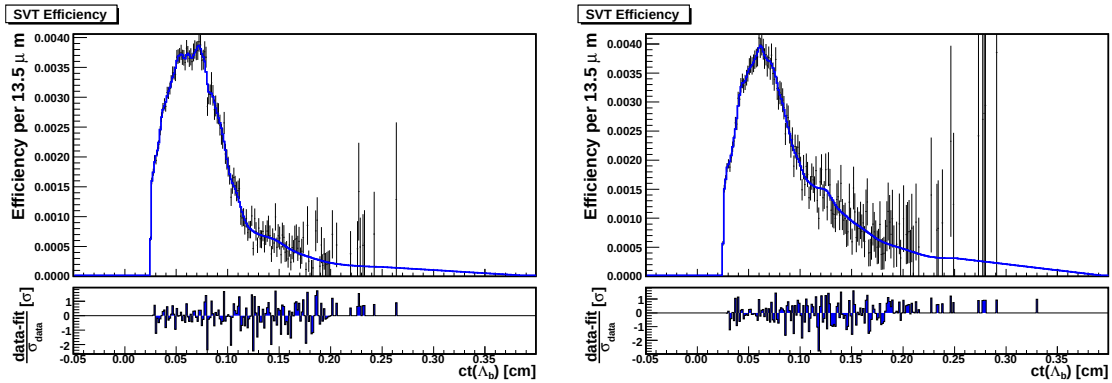

Figure 5.31: TTT efficiencies generated for trigger codes 24 (Left) and 99 (Right).

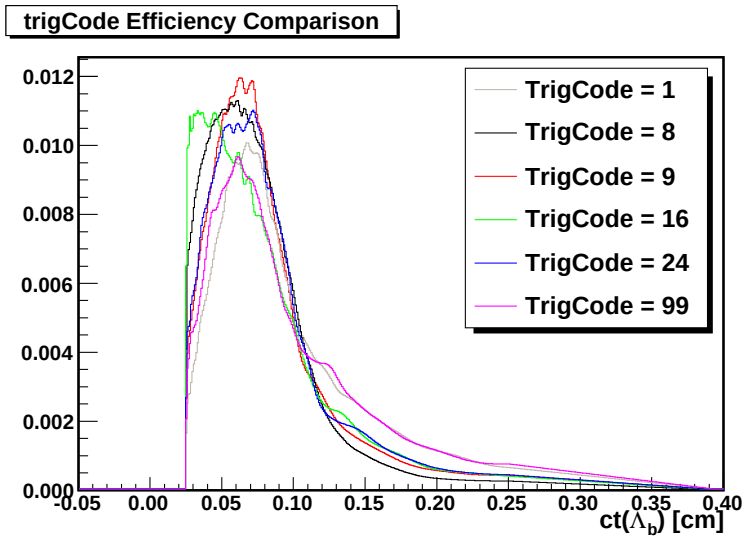

Figure 5.32: A comparison of TTT efficiencies from all of the different trigger codes.

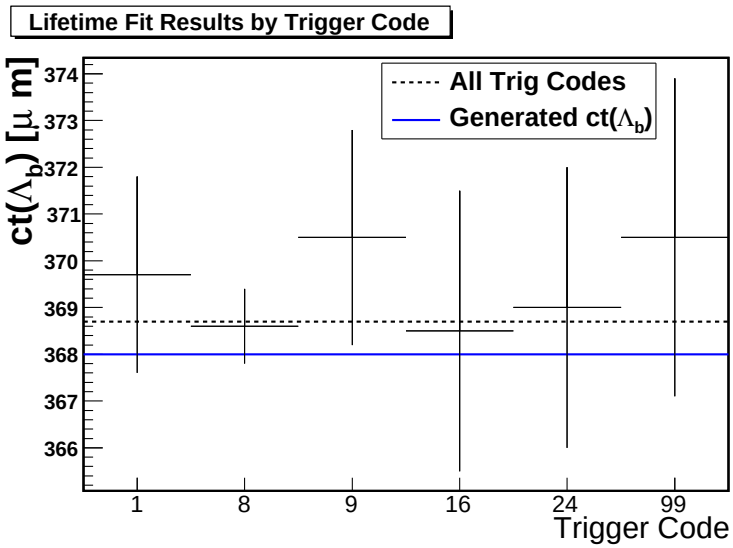

Figure 5.33: Λ_b^0 lifetime fit results from independent fits in different `trigCode` sub-samples of the HQGen Monte Carlo. The x-axis is an index for a particular trigger code (see Table 5.6). The y-axis is the resulting value of $ct(\Lambda_b^0)$ from the lifetime fit in a given index. The horizontal black line represents the value of the lifetime when all trigger codes are fit simultaneously. The horizontal blue line represents the generated $c\tau(\Lambda_b^0)$ value of 368.0μm. Each trigger code fit is consistent with the generated lifetime.

5.6 Lifetime Fit in $B^0 \to D^{*+}\pi^-$ Decays

As an additional cross-check of the fit method developed for measuring the Λ_b^0 lifetime, one can fit the lifetime of another *b*-hadron whose lifetime is known well. One such hadron is the B^0, that has been measured to have a lifetime of 1.530 ± 0.009ps (or expressed in microns as $458.7 \pm 2.7\mu$m) [8]. The $B^0 \to D^{*+}\pi^-$ decay mode is chosen as a cross-check because it is an extremely clean sample, with a signal to background ratio similar to that found in the Λ_b^0 sample. The lifetime fit that we use for the cross-check of the method is a very simple model compared to other analyses that are dedicated to accurately measuring the the B^0 lifetime in this channel [30]. Because the cross-check is intended only to build confidence in the fit method developed for the Λ_b^0, a simple B^0 lifetime model is sufficient.

The same two-step fit approach described in Section 5 for the Λ_b^0 fits is also used here for the B^0. The first step is a binned mass fit followed by an unbinned maximum likelihood fit in ct and σ_{ct}.

The signal and upper-sideband regions for the fit are defined as $m(D^{*-}\pi^+) \in [5.225, 5.331]\text{GeV}/\text{c}^2$ and $m(D^{*-}\pi^+) \in [5.4, 6.6]\text{GeV}/\text{c}^2$ respectively.

The σ_{ct} models, $P^s_{\sigma_{ct}}$ and $P^b_{\sigma_{ct}}$ are histograms derived directly from sideband-subtracted signal and upper sideband respectively. The distributions are shown in Figure 5.34.

The TTT efficiency distribution is computed from a B-Generator sample of pure $B^0 \to D^{*-}\pi^+$ decays. Approximately $23,300$ events are used to compute the efficiency using Equation 3.9. The $ct(B^0)$ distribution and the calculated TTT efficiency are shown in Figure

5.35.

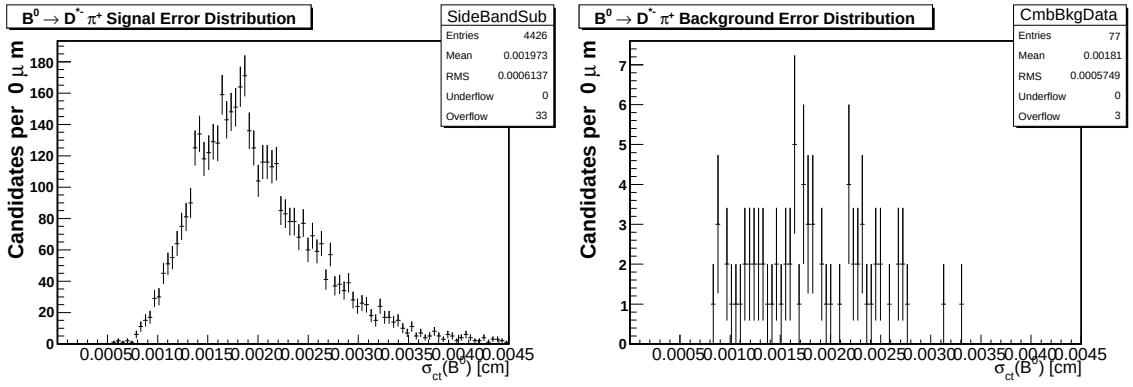

Figure 5.34: Left: The $P^{s}_{\sigma_{ct}}$ error distribution from sideband-subtracted data. Right: The $P^{b}_{\sigma_{ct}}$ distribution from the upper sideband. The statistics here are low because there are very few combinatorial events in the upper sideband.

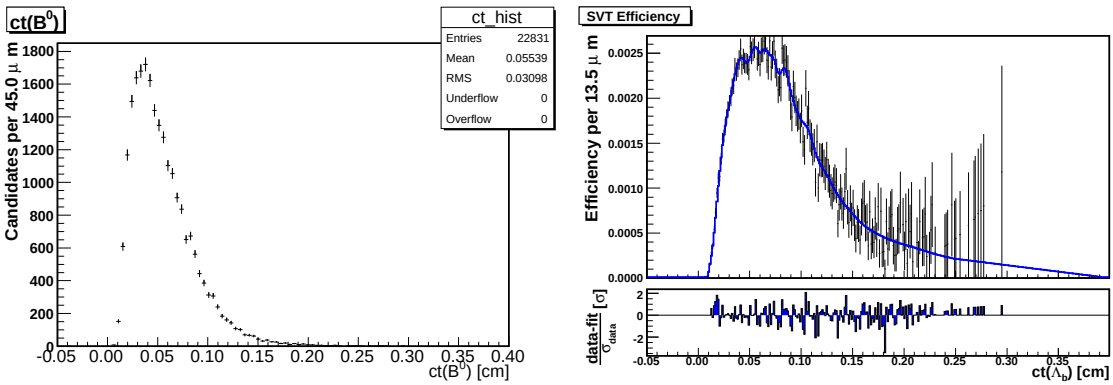

Figure 5.35: Left: The *ct* distribution from the B^0 signal Monte Carlo. Right: the efficiency distribution computed from the Monte Carlo using Equation 3.9.

Only three components are considered in the $B^0 \to D^{*-}\pi^+$ mass and lifetime fits. The fit components and templates used for each shape are listed below;

1. $B^0 \to D^{*-}\pi^+$ Signal: B^0 events that decay into D^* and a pion, with the D^{*-} decaying (eventually) into a kaon and two pions.

   - P^1_m: Parametric smeared Gaussian model.

- P^1_{ct}: The same parametric proper decay length model used to describe the Λ^0_b signal.

$$P^1_{ct}(ct|\sigma_{ct}) = exp(ct, c\tau) \otimes R(ct, \sigma_{ct}) \cdot \varepsilon_{TTT}(ct).$$

  Here, τ represents the B^0 lifetime and is the only parameter left floating in the lifetime fit.

- $P^1_{\sigma_{ct}}$: $P^s_{\sigma_{ct}}$ from sideband-subtracted data.

2. $B^0 \to D^{*-}K^+$ Background: B^0 events that decay into D^{*-} and a kaon, with the K^{*-} decaying (eventually) into a kaon and two pions.

   - P^2_m: Parametric Gaussian model.
   - P^2_{ct}: Since this background is comprised of true B^0 decays, the same model is used here as in the $B^0 \to D^{*-}\pi^+$ mode.
   - $P^2_{\sigma_{ct}}$: $P^s_{\sigma_{ct}}$ from sideband-subtracted data.

3. Combinatorial Background: B^0 events reconstructed with a true D^{*-} and a fake pion.

   - P^3_m: Parametric exponential model.
   - P^3_{ct}: Events in the upper sideband of data are fit with a Landau distribution to obtain the template shown in Figure 5.36.
   - $P^3_{\sigma_{ct}}$: $P^s_{\sigma_{ct}}$ from sideband-subtracted data.

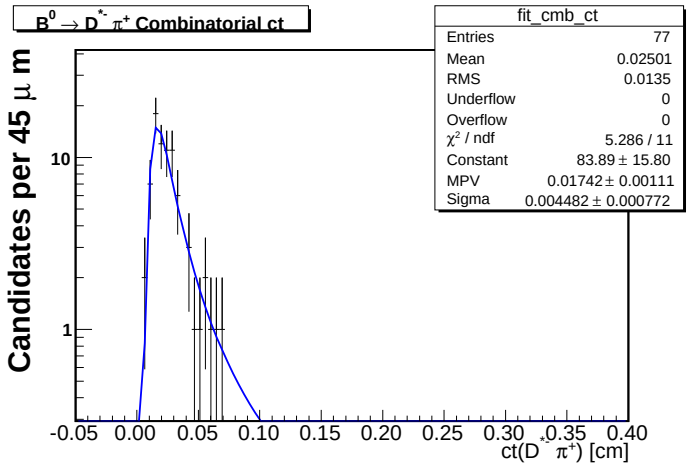

Figure 5.36: The combinatorial lifetime template is taken directly from a Landau fit to events in the upper sideband of data. The fit probability is 0.917.

5.6.1 $B^0 \to D^{*-}\pi^+$ Fit Results

The B^0 lifetime results presented here are compared to those reported in Reference [30]. The measurement made in the reference is a dedicated B^0 lifetime measurement and uses much more sophisticated mass and lifetime fits than those described in Section 5.6. Most importantly the reference measurement uses 6-component mass and lifetime fits as well as fitting for the lifetime using both fully and partially reconstructed B^0 candidates. By including partially-reconstructed candidates, the total statistical error on the lifetime measurement can be decreased. However, the lifetime fit becomes much more complicated for these events.

For the purpose of this cross check it is sufficient to compare results only with the fully-reconstructed events. In this case, our fit and the reference fit both fit exactly the same data and the fit results from both measurements are expected to agree very well. The fully-reconstructed B^0 region is defined as $m(D^{*-}\pi^+) \in [5.225, 5.331]\mathrm{GeV/c^2}$.

In addition, two results are quoted for our cross-check fit. In the first fit, the fit fractions, f_3, from our simple, three-component, mass fit are used in the subsequent lifetime fit. It is clear that this mass fit, shown in Figure 5.37, is a poor description of the data, especially at low values of $m(D^{*-}\pi^+)$. Therefore, a second lifetime fit is constructed using the sample composition, from the more sophisticated, 6-component reference mass fit described in [29]. The fractions from the reference mass fit, f_6, are transformed to our 3-component basis, these fractions are referred to as f_3'. The fractions for all of the mass fits are listed in Table 5.7.

Norm	f_3	f_6	f_3'
$B^0 \to D^*\pi$	0.9053	0.9063	0.9063
$B^0 \to D^*K$	0.0898	0.0670	0.0750
$B^0 \to D^*\rho$	-	0.0015	-
$B^0 Other$	-	0.0064	-
B^+	-	0.0036	-
real D	0.0049	0.0151	0.0187

Table 5.7: Fractions used in the $B^0 \to D^{*-}\pi^+$ lifetime fits. f_3 is the fraction of each component obtained from the 3-component mass fit. f_6 is the fraction of each component as reported in [30]. f_3' is obtained by applying the f_6 fractions to the 3 component basis in our fit model. In all cases, the normalizations represent the fraction of each component in the region, $m(D^{*-}\pi^+) \in [5.225, 5.331]\mathrm{GeV/c^2}$.

The results of the un-binned, maximum likelihood, B^0 lifetime fits on the data, using both f_3 and f_3' normalizations, are listed in Table 5.8. The likelihood projection onto the ct-axis, for both the f_3 and f_3' normalizations, is shown in Figure 5.38.

Normalization	$c\tau(B^0)[\mu\mathrm{m}]$
f_6	442.8 ± 12.8
f_3	434.0 ± 9.9
f_3'	440.3 ± 9.9

Table 5.8: Results of the B^0 lifetime fits in $D^{*-}\pi^+$ decays. The f_6 result is quoted directly from [30]. The f_3 and f_3' results are obtained by running the 3-component fit described in Section 5.6 with the normalizations described above.

The B^0 lifetime obtained using the f_3 normalizations is statistically compatible with

the f_6 result. Since the cross-check fits the same data as the reference fit, we expect much better agreement than just statistical compatibility. When the improved mass fit fractions, f_3', are applied, the agreement between the fit results improves dramatically.

Because the cross-check fit result is very close to the results reported in Reference [30], this cross-check serves as further validation that the methods developed for measuring the Λ_b^0 lifetime are reliable.

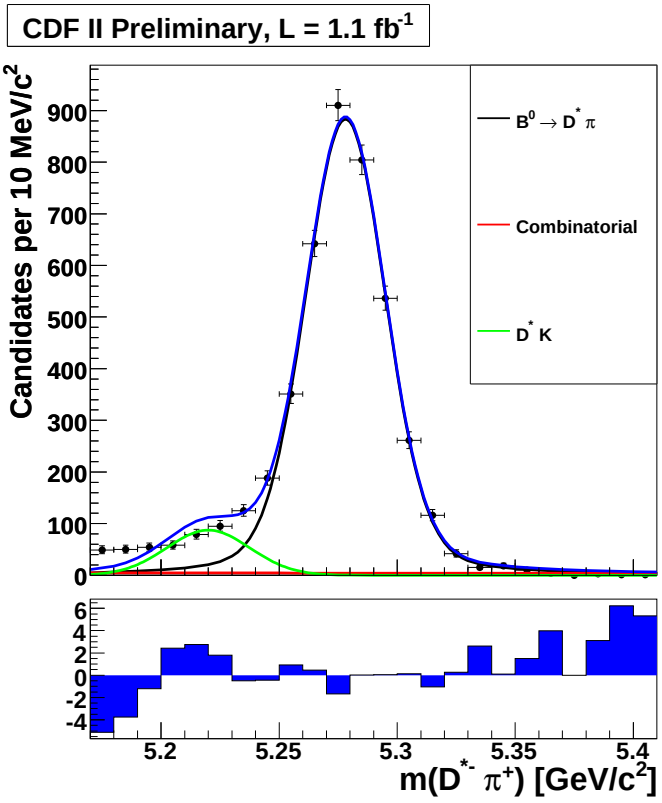

Figure 5.37: Mass fit result for the $B^0 \to D^{*-}\pi^+$ cross-check mode. From this fit, the f_3 normalizations are obtained.

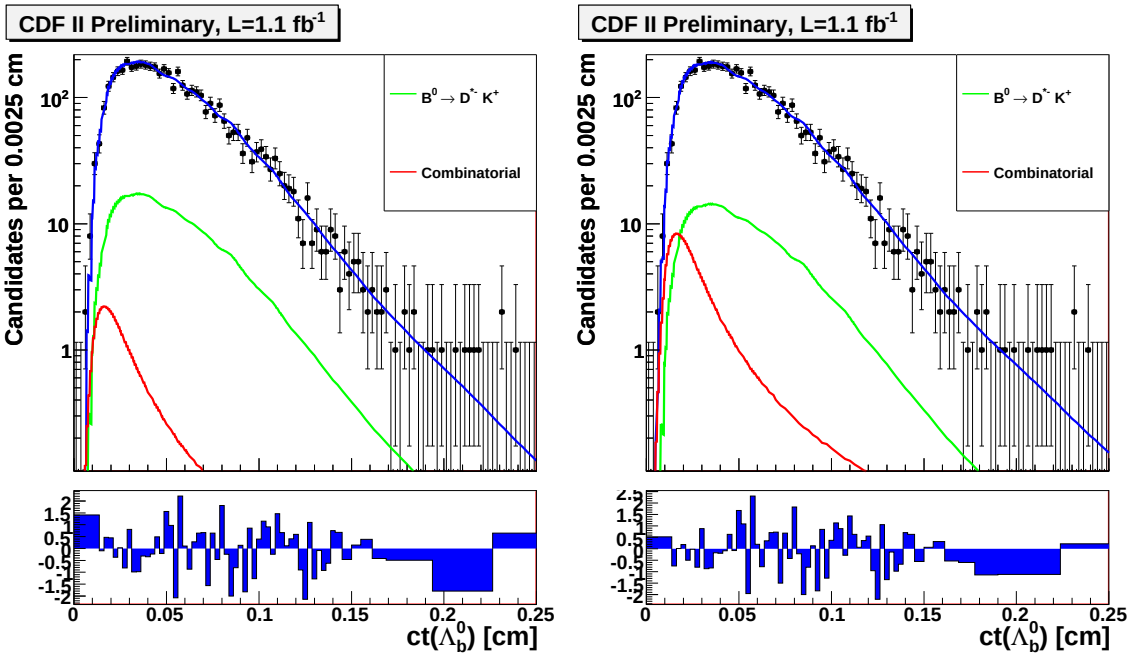

Figure 5.38: The projection of the 3-dimensional likelihood of the fit for $c\tau(B^0)$ on the *ct* axis. The green and red lines represent the contribution from the $B^0 \to D^{*-}K^+$ and combinatorial backgrounds respectively. The projection, using the f_3 normalizations is shown on the Left while the f_3' fit is shown on the Right.

Chapter 6

$\Lambda_b^0 \to \Lambda_c^+ \pi^-$ Fit Result

Using the likelihood and shapes described in Section 5.5.2 and the mass fit normalizations listed in Table 5.3 , the result of the un-binned, maximum likelihood, Λ_b^0 lifetime fit on data is

$$c\tau(\Lambda_b^0) = 422.8 \pm 13.8 \ \mu\text{m} \tag{6.1}$$

The resulting likelihood projected onto the ct-axis is shown in Figure 6.1.

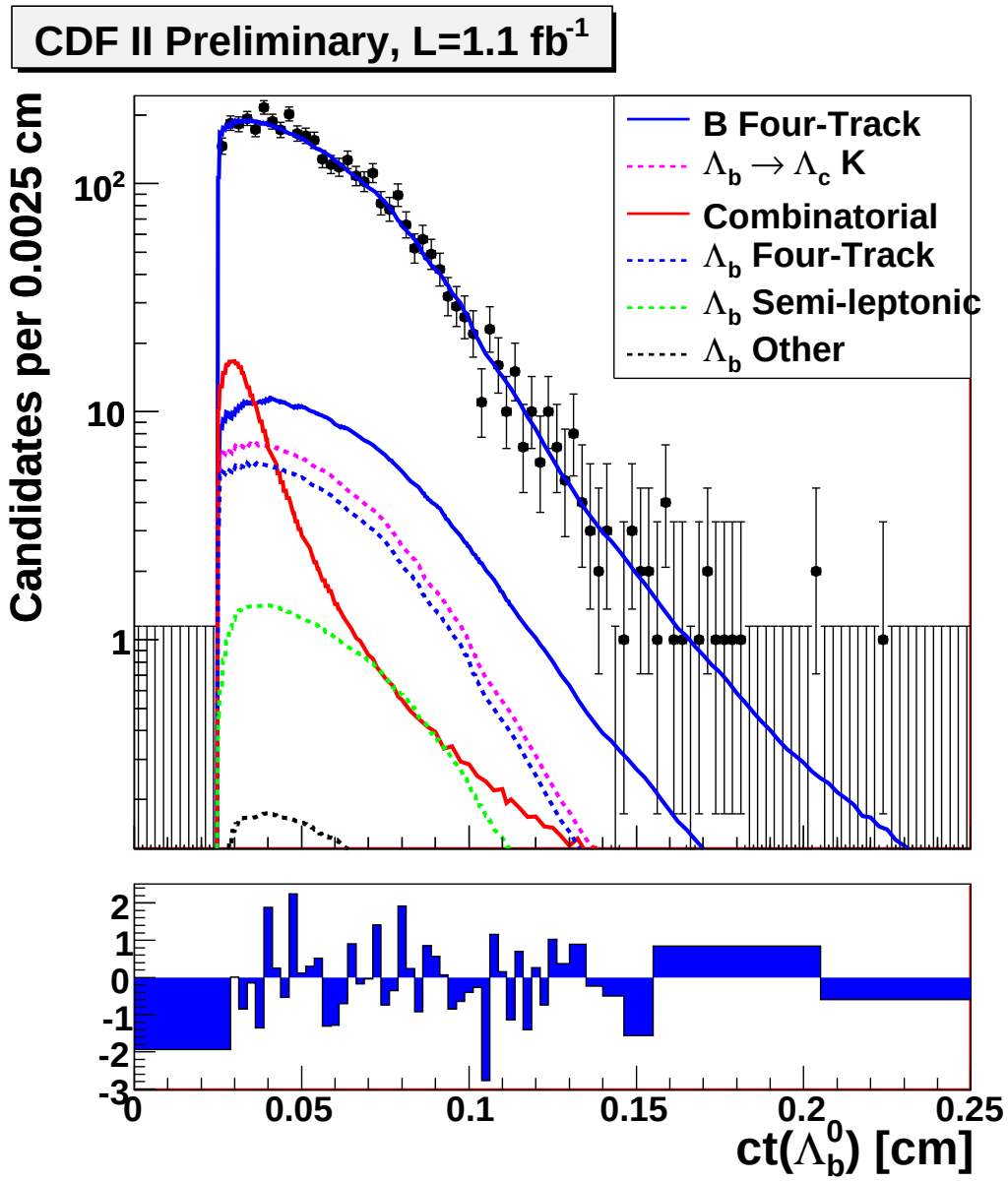

Figure 6.1: Λ_b^0 lifetime fit on data. The projection of the 3-dimensional likelihood of the fit for $\tau(\Lambda_b^0)$ on the *ct* axis.

6.1 $\Lambda_b^0 \to \Lambda_c^+\pi^-$ Result Cross-Checks

In order to gain confidence in the result, several additional cross checks have been performed.

6.1.1 Definition of the Signal Region

The baseline, $m(\Lambda_c^+\pi^-)$, signal window is modified by moving the lower edge up by 15MeV/c^2; cutting into some Λ_b^0 signal but also significantly reducing the contribution from many of the backgrounds. The mass fit remains the same as that used in the default fit but the fit normalizations change with the re-definition of the signal window. The efficiency distribution is recalculated from the HQGen Monte Carlo sample using the new mass window definition. Additionally, the $P^s_{\sigma_{ct}}$ distribution is also recreated to reflect the change in the signal mass window while $P^b_{\sigma_{ct}}$ remains unchanged.

The normalizations and lifetime fit results are listed in Table 6.1. The lifetime fit projection is shown in Figure 6.2. The lifetime result with the new normalizations is $429.0 \pm 14.4 \mu m$ for a shift of about $6 \mu m$ compared to the baseline fit result.

6.1.2 Split the Signal Region

The default $m(\Lambda_c^+\pi^-)$ signal window is split in half; a low ($5.565 \leq m(\Lambda_c^+\pi^-) \leq 5.617$) and high ($5.617 \leq m(\Lambda_c^+\pi^-) \leq 5.670$) mass window. The mass fit remains unchanged, but the normalizations are re-defined for each of the signal mass windows. Efficiency

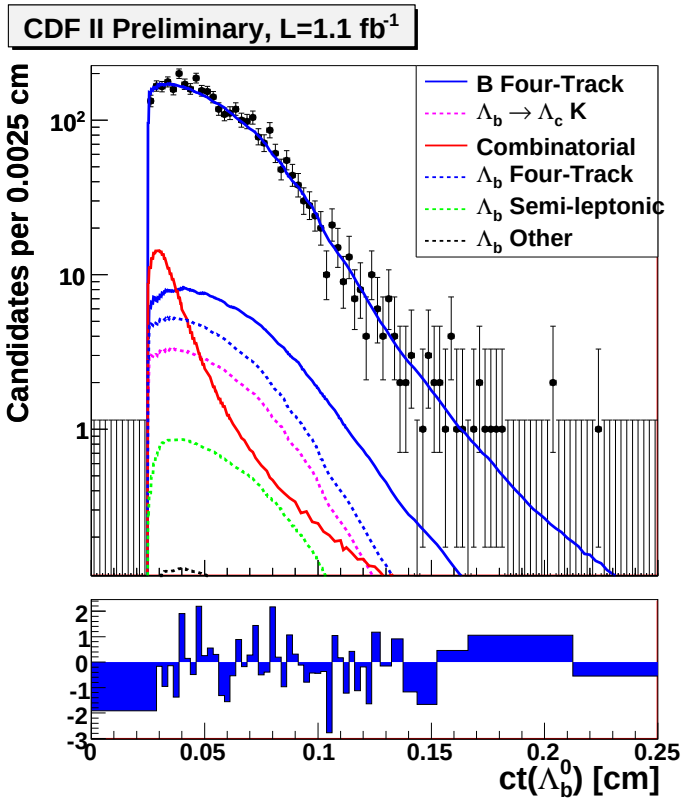

Figure 6.2: Lifetime fit projection with a revised mass signal window. The lower edge of the baseline mass window is moved 15MeV/c^2 from 5.565 to 5.580GeV/c^2.

Normalization	Value
$N_{\Lambda_b^0\to\Lambda_c^+\pi^-}$	2789.4 ± 55.6 (86%)
$N_{BFour-Track}$	181.2 ± 11.1 (6%)
$N_{\Lambda_b^0 Four-Track}$	101.6 ± 14.2 (3%)
$N_{Combinatoric}$	98.9 ± 4.3 (3%)
$N_{\Lambda_b^0\to\Lambda_c^+K}$	63.8 ± 7.3 (2%)
$N_{\Lambda_b^0 Semi-leptonic}$	16.3 ± 4.7 (1%)
N_{BOther}	5.6 ± 5.3 ($< 1\%$)
$c\tau(\Lambda_b^0)$	$429.0 \pm 14.4 \mu m$

Table 6.1: Normalizations for all backgrounds in the modified signal window; $5.580 \leq m(\Lambda_c^+\pi^-) \leq 5.670$.

distributions are recalculated from the signal Monte Carlo sample for both the low and high mass windows. Additionally, $P^s_{\sigma_{ct}}$ distributions are also recalculated to reflect the changes in the low and high signal windows. The same $P^b_{\sigma_{ct}}$ distribution is used in both the high and low mass window fits.

The normalizations and Λ_b^0 lifetime result from each fit are listed in Table 6.2. The projection of the fits on the proper time axis are shown in Figure 6.3. Both fits are consistent with each other and with the default Λ_b^0 lifetime fit result.

Quantity	Low Mass Window	High Mass Window
$N_{\Lambda_b^0\to\Lambda_c^+\pi^-}$	1650.0 ± 32.9 (79%)	1245.8 ± 25.0 (86%)
$N_{B^0\ Four-track}$	177.1 ± 10.9 (8%)	73.3 ± 4.5 (5%)
$N_{\Lambda_b^0\to\Lambda_c^+K^-}$	131.8 ± 15.1 (6%)	6.7 ± 0.8 ($< 1\%$)
$N_{Combinatoric}$	58.8 ± 2.5 (3%)	57.4 ± 2.5 (4%)
$N_{\Lambda_b^0\ Four-track}$	50.0 ± 7.0 (2%)	63.7 ± 8.9 (4%)
$N_{\Lambda_b^0\to l\bar{\mu_l}X}$	23.3 ± 6.7 (1%)	3.7 ± 1.1 ($< 1\%$)
$N_{\Lambda_b^0\ Other}$	2.4 ± 0.2 ($< 1\%$)	1.0 ± 0.1 ($< 1\%$)
$c\tau(\Lambda_b^0)$	$428.2 \pm 18.3\mu m$	$414.8 \pm 21.0\mu m$

Table 6.2: Comparison of normalizations and resulting lifetimes when the mass and lifetime fit are run separately on a low, $5.565 \leq m(\Lambda_c^+\pi^-) \leq 5.617$, and high, $5.617 \leq m(\Lambda_c^+\pi^-) \leq 5.670$, mass windows. mass window.

6.1.3 Lifetime Fit by Run Ranges

As a final cross-check, the lifetime fit is run independently on data from different run periods; `xbhd0d`, `xhbd0h`, and `xhbd0i`. The `xbhd0i` dataset only consists of runs up to 212133 (instead of the standard 233111) because only those runs were available when the data sample was stripped. In each of the three run ranges, the two-step mass and lifetime fit is performed. The same default lifetime fit model is used when fitting each sample. The normalizations from the mass fits and lifetime fit results in each run range are given in Table 6.3 with the fit projections shown in Figure 6.4. In each of the three samples, the fit results are consistent with one another and with the baseline fit result.

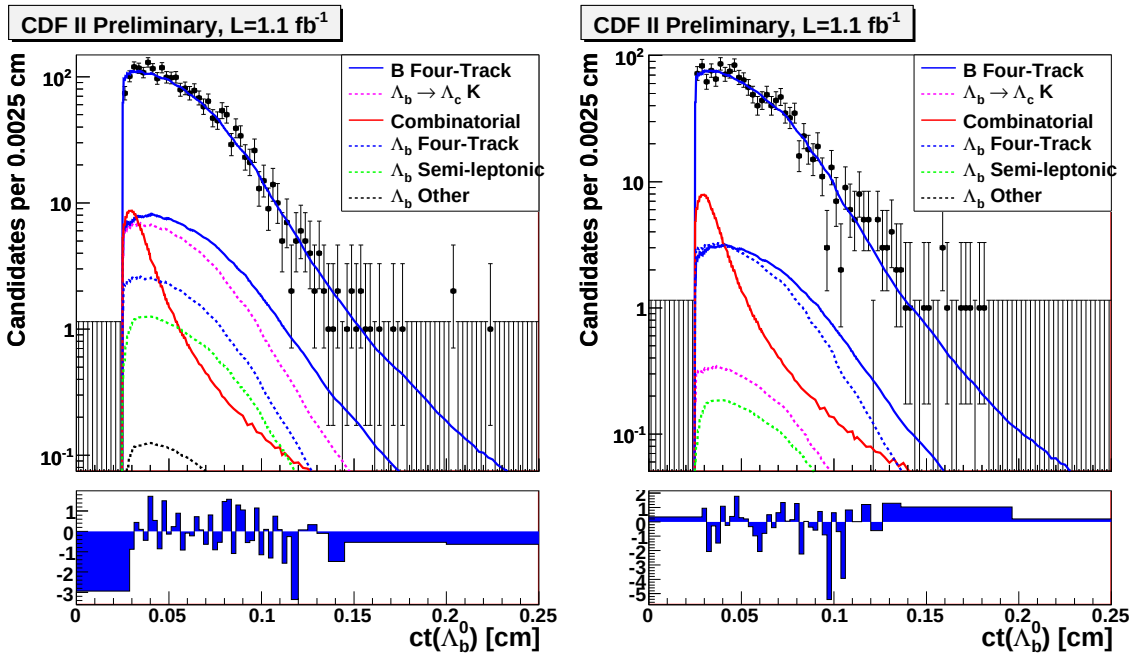

Figure 6.3: Lifetime fit results on two mass windows. Left: the low mass window, $5.565 \leq m(\Lambda_c^+ \pi^-) \leq 5.617 \mathrm{GeV/c^2}$ and Right: the high mass window, $5.617 \leq m(\Lambda_c^+ \pi^-) \leq 5.670 \mathrm{GeV/c^2}$.

Quantity	0d	0h	0i
$N_{\Lambda_b^0 \to \Lambda_c^+ \pi^-}$	946.3 ± 33.3 (81%)	1199.6 ± 37.3 (82%)	768.1 ± 30.0 (81%)
$N_{BFour-Track}$	108.7 ± 10.5 (9%)	121.1 ± 11.3 (8%)	86.4 ± 8.6 (9%)
$N_{Combinatoric}$	42.1 ± 2.8 (4%)	46.7 ± 3.1 (3%)	29.9 ± 2.4 (3%)
$N_{\Lambda_b^0 Four-Track}$	21.2 ± 6.2 (2%)	36.7 ± 7.5 (3%)	20.6 ± 5.3 (2%)
$N_{\Lambda_b^0 \to \Lambda_c^+ K}$	38.4 ± 7.0 (3%)	36.8 ± 8.4 (3%)	21.6 ± 5.8 (2%)
$N_{\Lambda_b^0 Semi-leptonic}$	11.7 ± 3.4 (1%)	16.2 ± 4.0 (1%)	9.0 ± 2.8 (1%)
$N_{\Lambda_b^0 Other}$	1.2 ± 0.1 ($< 1\%$)	1.4 ± 0.1 ($< 1\%$)	1.0 ± 0.1 ($< 1\%$)
$c\tau(\Lambda_b^0)$	$398.2 \pm 22.6 \mu m$	$448.1 \pm 24.3 \mu m$	$406.5 \pm 25.8 \mu m$

Table 6.3: Comparison of normalizations and resulting lifetimes from fits on data from separate run periods.

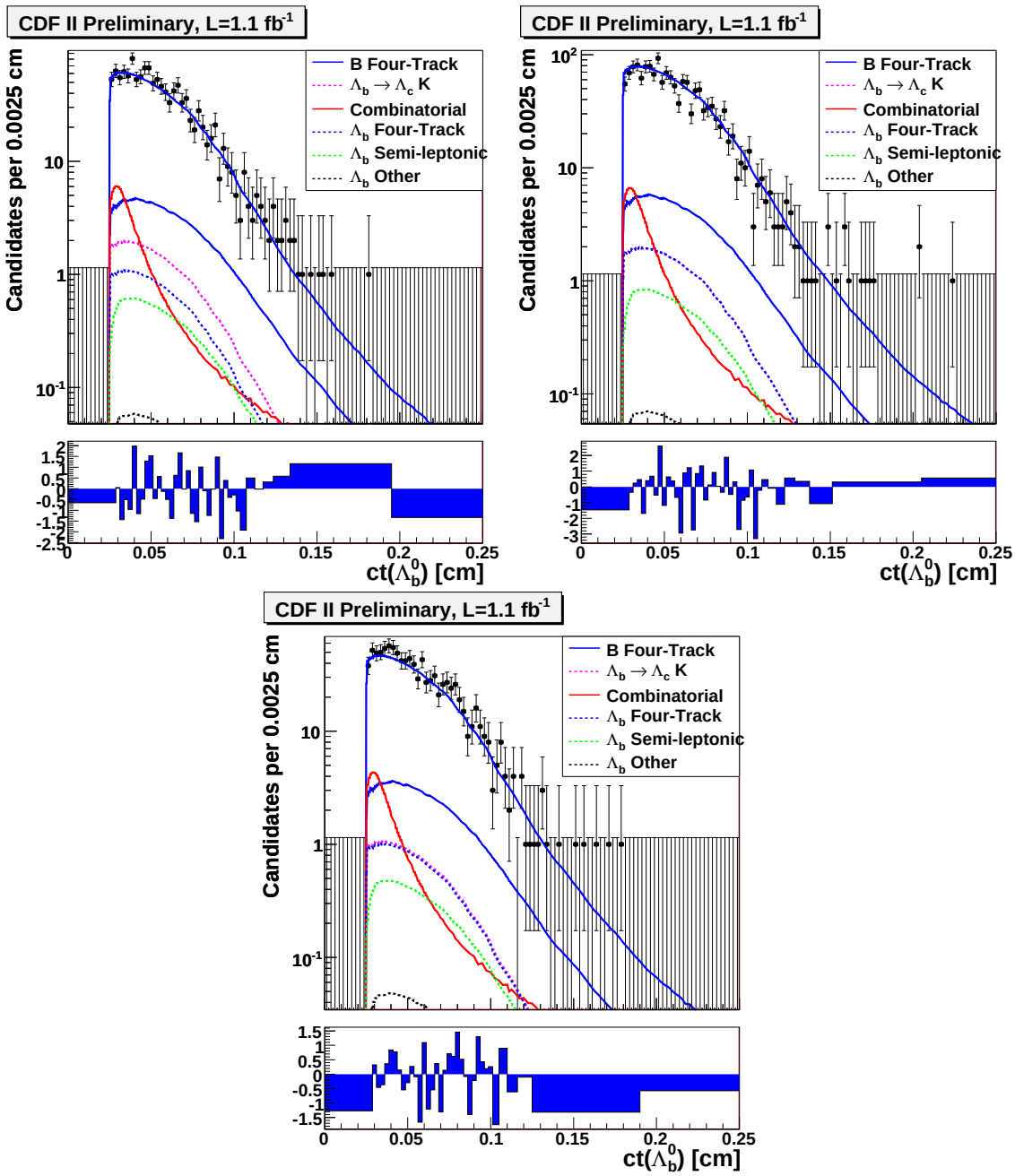

Figure 6.4: Lifetime fit results for `xbhd0d` (Top Left), `xbhd0h` (Top Right), and `xbhd0i` (Bottom).

Chapter 7

Estimated Systematic Error

According to their effect on calculating the SVT efficiency, we divide the systematic error estimates into two groups: those that bias the SVT efficiency, and those that do not.

As described in Section 5, we first execute a binned likelihood fit of the $m(\Lambda_c^+\pi^-)$ axis (the mass fit), followed by a two-dimensional unbinned maximum likelihood fit of *ct* and σ_{ct} (the lifetime fit) on a restricted mass range. All of the parameters that are floating in the mass fit are fixed in the lifetime fit so each fit can be considered independently. In other cases, especially when testing for bias in the procedure, we generate distributions, from the full 2-D PDF, on the entire mass region ($4.8\mathrm{GeV/c^2} < \mathrm{m}(\Lambda_c^+\pi^-) < 7.0\mathrm{GeV/c^2}$), and then fit using the previously described two-step procedure.

Most of the systematic errors in the Λ_b^0 lifetime measurement are evaluated using a modified Toy Monte Carlo technique. For the parameters associated with an individual systematic, we generate Toy Monte Carlo samples where these parameters are varied. The

sample is fit with both the default fit and the fit with varied parameters. We take the difference between the values of Λ_b^0 lifetime in the 'varied' (a.k.a. 'rigged') fit and the 'default' fit. This difference, caused by the systematic variation, constitutes the associated systematic error. After generating and fitting 1000 Toy Monte Carlo samples, the resulting distribution is fit with a Gaussian, and the mean is taken as the systematic shift due to that particular systematic.

7.1 Non-SVT-Biased Systematics

First we treat the systematic uncertainties that are common to any fully reconstructed CDF lifetime measurement, regardless of whether that measurement is biased by the SVT trigger.

7.1.1 Alignment

A 2.0 μm systematic error is quoted from a previous CDF lifetime analysis [1].

7.1.2 Fitter bias

The fitter bias can be evaluated by running a sufficiently large set of Toy Monte Carlo experiments. The fitter bias has been discussed previously in Section 5.5.3 and found to be negligible.

Description	**Value**
Absolute smearing of the blinded lifetime	$0.31\mu m$
Fractional smearing of the blinded lifetime	0.08%
Fractional smearing of the $N_{\Lambda_b^0 \to \Lambda_c^+ \pi^-}$	0.82%
Fractional smearing of the $N_{B\ Four-track}$	2.5%

Table 7.1: Summary of results from 1000 fluctuations of the $B \to$ four-track mass template.

7.1.3 Background mass template shapes

The shape of various templates in the background depend on the relative amounts of different modes in the background Monte Carlo samples. These shapes affect the relative contributions of each background mode to the total shape. The most significant source of background in the Λ_b^0 signal window is the contribution from the $B \to$ four track template. By far the biggest contribution to this component comes from $B^0 \to D^+\pi^-$ decays (approximately half). Therefore the $B \to$ four track template is modified by fluctuating the number of $B^0 \to D^+\pi^-$ decays according to the 1 sigma PDG uncertainty.

An ensemble of 1000 experiments with fluctuated $B^0 \to D^+\pi^-$ contributions was performed. The result of the experiments are summarized in Table 7.1, and the Λ_b^0 lifetime distribution is shown in Figure 7.1. Based on this result, the systematic uncertainty due to the shape of the mass templates in the signal window is negligible.

Four examples from these experiments of the fluctuation of the $B \to$ four track background component are given in Figure 7.2.

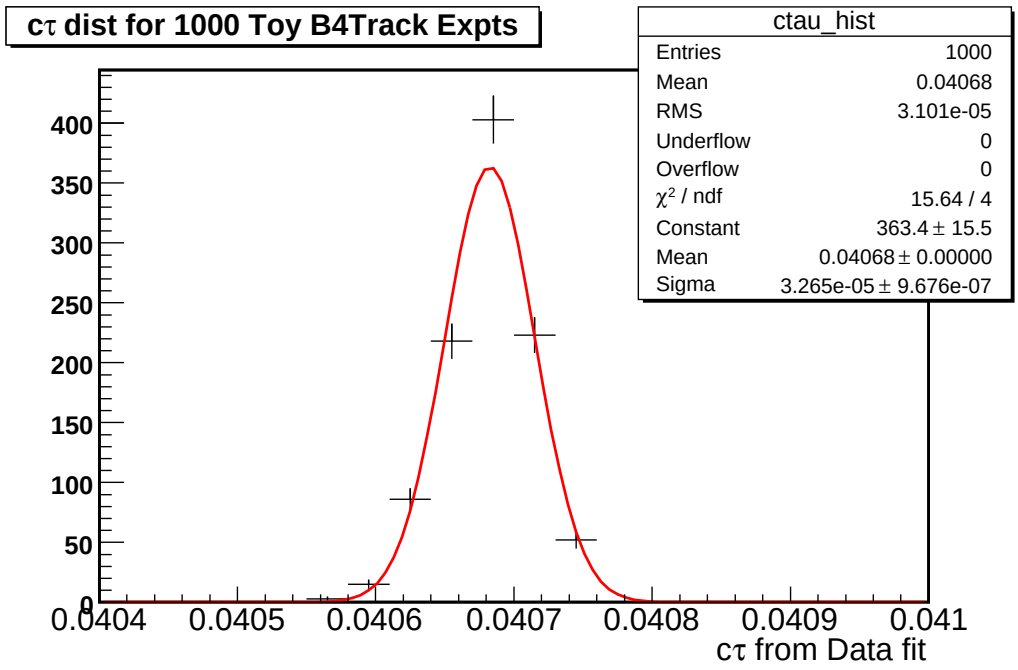

Figure 7.1: The distribution of Λ_b^0 lifetimes from 1000 toy experiments where the amount of $B^0 \to D^+\pi^-$ decays is fluctuated. For each toy experiment, the blinded lifetime fit is repeated on the data.

7.1.4 Background normalizations

The normalization of each background component is obtained from the binned mass fit that is run before the lifetime fit (see Table 5.3). The mass normalizations are all parameters obtained from the mass fit; and therefore come with some uncertainty. The normalizations fix the fraction of each type of background allowed in the final lifetime fit.

In order to evaluate the systematic effect of this uncertainty, an ensemble of 5 sets of mass normalizations was generated. Each normalization is fluctuated according to a Gaussian (where the mean is the baseline value from the mass fit, and the width is the uncertainty from the mass fit). For each set of normalization parameters, the baseline lifetime

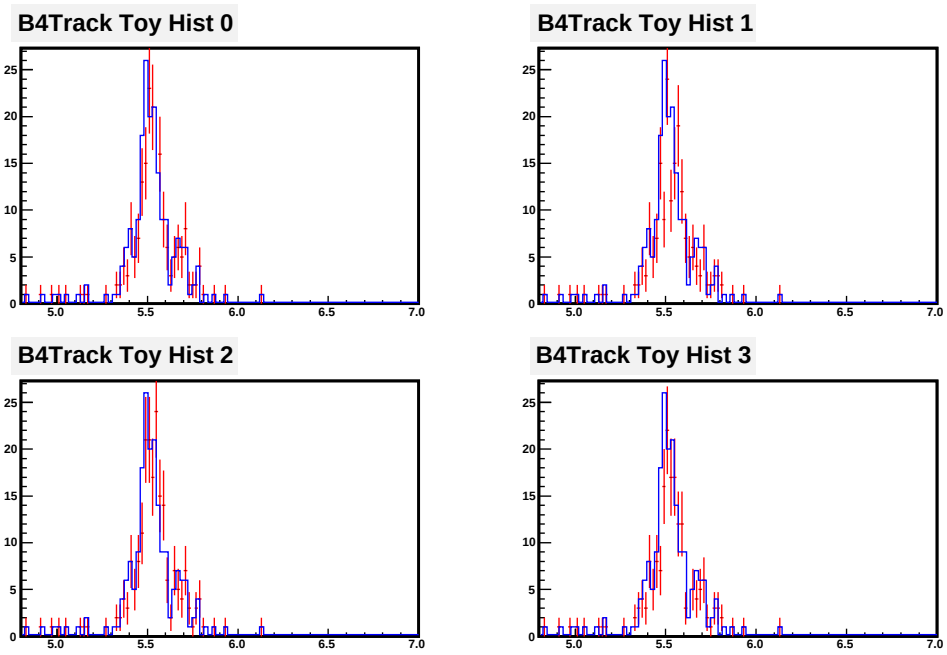

Figure 7.2: Four examples of the fluctuated versions of the $B \rightarrow$ four track background component. Blue: baseline un-fluctuated background component; Red: fluctuated background component

fit is repeated, and the resulting PDFs are fed into the Toy Monte Carlo ($\sim$ 500 iterations). The distribution of the resulting Toy lifetime fits and their pull distribution for one ensemble are shown in Figure 7.3. The estimated systematic uncertainty due to the background normalization uncertainty is 1.0μm as listed in Table 7.2.

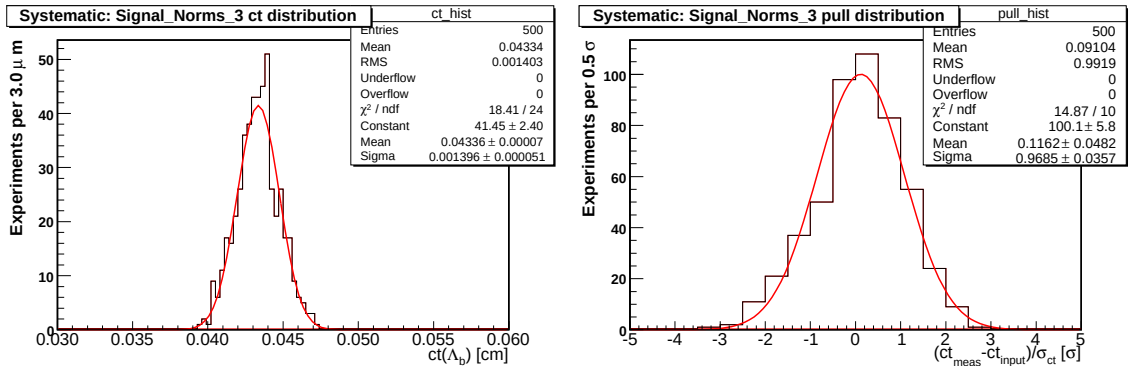

Figure 7.3: Left: The distribution of lifetime fit results from the baseline lifetime fit on Toy events generated from Signal_Norms_3 rigged PDF's. The results are fit with a Gaussian distribution shown in red. Right: the pull distribution for the Toy fits. The pull is defined as fit *ct* - rigged *ct* / fit σ_{ct}.

Sample	$\overline{ct_{Rig}}$ $[\mu m]$	$\overline{ct_{Toy}}$ $[\mu m]$	$\overline{ct^i_{Rig} - ct^i_{Toy}}[\mu m]$
Signal_Norms_1	431.6	432.7	-0.9
Signal_Norms_2	430.5	432.1	-1.9
Signal_Norms_3	432.9	433.5	-0.2
Signal_Norms_4	433.7	433.3	0.2
Signal_Norms_5	433.8	433.8	0.0
		Quoted Systematic (RMS):	0.9

Table 7.2: Summary of the Toy Monte Carlo experiments to estimate the systematic error due to the uncertainty in the normalizations obtained from the mass fit.

7.2 SVT-Biased Systematics

All of the systematic uncertainties listed below are due to uncertainties in parameters or distributions which are fixed in the lifetime fit. Most important of these is the efficiency function.

The systematic errors are estimated using the following Toy Monte Carlo procedure:

- A maximum or minimum fluctuation (or an ensemble of possible fluctuations) is constructed for a given source of systematic error. If the fluctuation affects the signal Monte Carlo sample, a new, *rigged* efficiency function is calculated.

- The blinded lifetime fit is repeated using the *rigged* efficiency function or other fluctuation. The lifetime from the resulting fit is $ct_{Rig}(\Lambda_b^0)$. The resulting PDF's are those that we would have measured if the data **really was** different by the amount assumed by the fluctuation in the first step.

- 1000 Toy Monte Carlo datasets are generated based on the *rigged* PDF's.

- Each Toy dataset, is fit with the *baseline* blinded fit. Here, we attempt to fit the *rigged* data with our "wrong" *baseline* likelihood. The mean lifetime from the *baseline* fit to *rigged* Toy samples is $\overline{ct_{Toy}}(\Lambda_b^0)$.

- The systematic is the difference between $ct_{Rig}(\Lambda_b^0)$ and $\overline{ct_{Toy}}(\Lambda_b^0)$.

7.2.1 Preliminary remarks on the SVT simulation

The crux of the Λ_b^0 lifetime measurement is the determination of the efficiency of the TTT. This efficiency function is evaluated from a carefully crafted realistic Monte Carlo simulation. The systematics below fall into two groups:

1. systematic uncertainties arising from the simulation of the CDF II detector and the TTT trigger

2. systematic uncertainties arising from the lack of knowledge of the Λ_b^0 baryon production and its decay into $\Lambda_c^+\pi^-$.

As it is shown below, the second group of systematics dominates over the first one. The first group (systematic errors on the TTT efficiency that arises from the incorrect or incomplete description of the hardware) can be divided into two parts:

(a) Monte Carlo simulation of the CDF events

(b) simulation of the SVT reconstruction and TTT

We will address these two in the reverse order. We use the program `svtsim`, which is an *emulator* of the trigger hardware. When the data are fed into it, it produces bitwise identical results as the SVT crates. We apply the TTT selection criteria offline, but use the SVT information (p_T, d_0, ϕ_0) produced by `svtsim`.

Therefore, in **(b)** there is no room for a systematic error, as the computations are exact. The only source of the systematic uncertainty in this case is **(a)** – potentially incorrect simulated data that are fed into the trigger simulation.

The way we generate and simulate events using the B group's realistic Monte Carlo simulation is described in Section 4.3.1. In brief, the GEANT3 tracing engine calls the silicon charge deposition model which has been tuned on data. In the `SiClusteringModule`, the run-by-run calibration constants are downloaded and all dead and noisy channels are masked away (including whole SVX3d chips and occasionally dead half-ladders). We are using luminosity-weighted simulation, and the dead channel map is downloaded run by run. The misalignment could impact the TTT rates, and its effect is quoted as a source of systematic error (the main source being the uncertainty on the radial scale of the SVXII as a whole, and primarily impacts the meaning of L_{xy} rather than the TTT efficiency). We estimate a systematic error due to the source **(a)** explained above using a data sample collected with an independent (di-muon) trigger path. The only remaining effect that can impact the behavior of SVT is the location of the primary vertex, which is also obtained run-by-run in the simulation, and which is studied and quoted as a separate source of the systematic uncertainty.

7.2.2 Data-Monte Carlo Agreement: simulation of SVX II and SVT

Nevertheless, we wish to set an upper limit on how discrepant the Monte Carlo simulation of SVX II and SVT could be from the data, and assign a systematic error which thus covers several of the areas described above.

In order to separate the physics effects arising from the lack of knowledge of the Λ_b^0 baryon production and its decay into $\Lambda_c^+\pi^-$ (which are handled separately and yield several sources of the systematic error), we 'fake' the Monte Carlo simulation by feeding the four vectors of muons from a $J/\psi \to \mu^+\mu^-$ decay, simulate those events and then compare them to the original data.

We reconstruct $J/\psi \to \mu\mu$ events in the `xpmm0d` sample, collected with the di-muon trigger. To reduce the data size we apply loose cuts of $p_T(\mu) > 2$ GeV and $L_{xy}(J/\psi) > 100$ μm. The resulting J/ψ mass distribution fitted to a Gaussian (signal) and a second-order polynomial (background) is shown in Fig. 7.4. We define $m(J/\psi) \pm 3\sigma$ as the signal

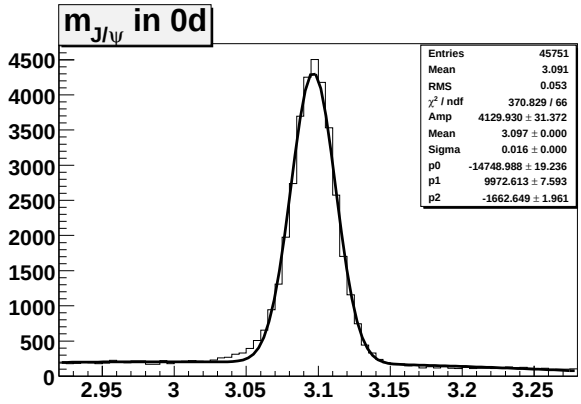

Figure 7.4: $J/\psi \to \mu\mu$ mass fitted to a Gaussian (signal) and a second-order polynomial (background).

region and [-10σ,-5σ], [5σ,10σ] as the sideband regions.

Following the prescription of a previous work [47] we calculate J/ψ sideband subtracted TTT efficiencies, $\varepsilon = N^{trig}/N^{tot}$, in $p_T(\mu)$, $|d_0(\mu)|$ and $L_{xy}(J\psi)$ bins, where N^{tot} is the total number of muons (J/ψ candidates) in a given bin, and N_i^{trig} is the corresponding

number of muons (J/ψ candidates) passing the SVT/offline track matching and TTT cuts. Fig. 7.5 shows the sideband subtracted N^{trig} (red) and N^{tot} (black) histograms (top) and the corresponding efficiencies, ε, (bottom).

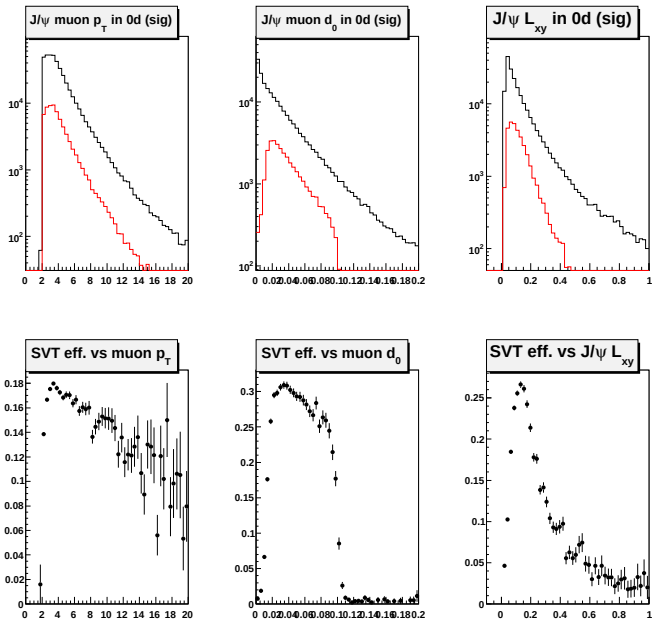

Figure 7.5: Sideband subtracted N^{trig} (red) and N^{tot} (black) histograms in $p_T(\mu)$, $|d_0(\mu)|$ and $L_{xy}(J\psi)$ bins (top) and the corresponding efficiencies, ε, (bottom).

To ensure maximum possible compatibility between physics events in data and Monte Carlo, we generate HEPG banks from the reconstructed momenta and production vertices from the data events and pass them through the same series of detector and trigger simulations and reconstruction algorithm as our Λ_b^0 signal realistic MC. The efficiencies from the resulting "Fake MC" is shown in Fig. 7.6. Note that since we use real data events for MC simulation, the MC distributions are sideband subtracted the same way as data. Finally we calculate a correction factor, $CF = \varepsilon^{data}/\varepsilon^{MC}$, in the bins of $L_{xy}(J/\psi)$. Fig. 7.7 shows

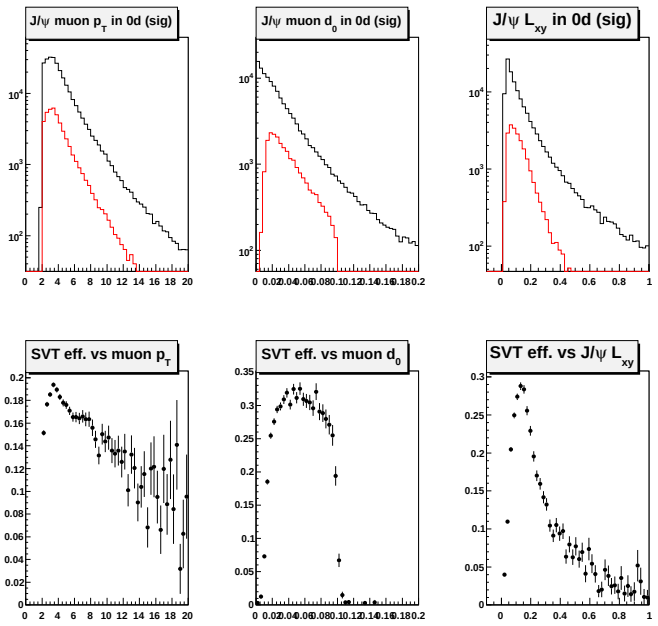

Figure 7.6: Sideband subtracted N^{trig} (red) and N^{tot} (black) histograms in $p_T(\mu)$, $|d_0(\mu)|$ and $L_{xy}(J\psi)$ bins (top) and the corresponding efficiencies, ε (bottom) in "Fake MC".

the $CF(L_{xy})$ distribution fitted to a linear function. The resulting slope, 0.037 ± 0.102, is consistent with zero.

However, given the available statistics of $J/\psi \rightarrow \mu\mu$ data available for this check, one cannot rule out a slight deviation of the slope of the correction factor $CF(L_{xy})$ from zero. Therefore we evaluate the upper limit on a possible source of a systematic error due to the simulation of the SVX II detector and SVT by changing the slope of $CF(L_{xy})$ by 1σ (0.102) up and down from the central value of 0.037, and evaluate the effect. Note, however, that this is the *upper limit* on a presence of a systematic error from this source. The actual error is likely smaller – but we have no ability to tell by how much.

In order to evaluate the effect of moving the slope of $CF(L_{xy})$ by $\pm 1\sigma$, we take both

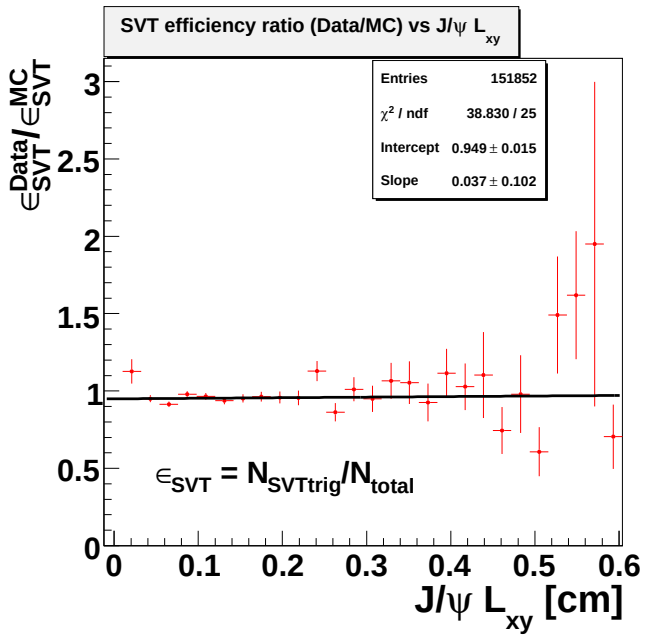

Figure 7.7: Sideband subtracted SVT efficiency correction factor distribution in $L_{xy}(J\psi)$ bins. Shown also is the result of its fit to a 1st-order polynomial.

shifts and reweight the large realistic Monte Carlo sample, thus obtaining two additional 'rigged' TTT efficiency distributions, which are used to estimate the systematic error by

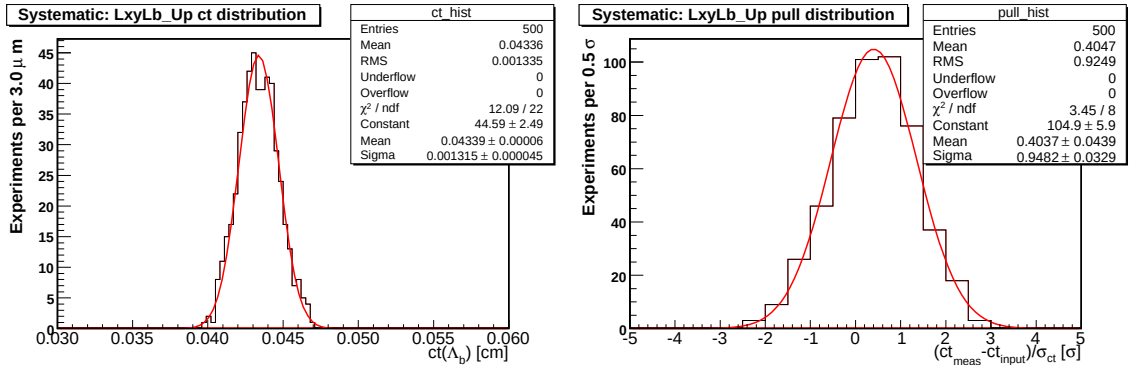

Figure 7.8: Left: The distribution of lifetime fit results from the baseline lifetime fit on Toy events generated from rigged $L_{xy}(\Lambda_b^0)$ PDF's. The results are fit with a Gaussian distribution shown in red. Right: the pull distribution for the Toy fits. The pull is defined as (fit *ct* - rigged *ct*) / fit σ_{ct}.

Sample	$\overline{ct_{Rig}}$ $[\mu m]$	$\overline{ct_{Toy}}$ $[\mu m]$	$\overline{ct^i_{Rig} - ct^i_{Toy}}[\mu m]$
$L_{xy}(\Lambda_b^0) + \sigma$	427.2	433.9	-6.3
$L_{xy}(\Lambda_b^0) - \sigma$	433.8	433.5	0.5
Estimated Systematic Error			6.3

Table 7.3: Summary of the results from Toy Monte Carlo experiments to estimate the systematic error due to the uncertainty in the SVT model.

the usual Toy MC method. Fig. 7.8 (left) shows a distribution of lifetime fit results from the baseline lifetime fit on Toy events generated from a rigged $L_{xy}(\Lambda_b^0)$ PDF. Also shown is its fit (red) to a Gaussian. The corresponding pull distribution is shown on the right. The results from the $+1\sigma$ and -1σ experiments are summarized in Table 7.3. The estimated systematic error due to uncertainties in the SVT simulation inputs is 6.3 μm.

7.2.3 Data-Monte Carlo Agreement: Primary Vertex Position

The `5.3.4` version of the B group's Monte Carlo production package that was used to generate the HQGen sample of $\Lambda_b^0 \to \Lambda_c^+ \pi^-$ decays only includes SVT beamline information up to and including run number 186586. The $1.1\, fb^{-1}$ data sample that we fit to obtain the Λ_b^0 lifetime result includes runs up to run number 212133. As a result, the primary vertex position is not well reproduced in runs beyond run number 186586 (see Appendix C.4).

To estimate the systematic error due to the difference in primary vertex positions, the Monte Carlo was split into four samples; low and high primary vertex *x* position and low and high primary vertex *y* position samples. Each sample has approximately the same number events, roughly splitting the sample in half in *x* and *y* primary vertex position respectively. Rigged efficiency functions were computed from each of the four samples. Toy experiments are again used to generate events according to the rigged PDFs which are fit with the baseline model. The Toy lifetime fit results and the pull distribution for one of the samples are shown in Figure 7.9. The results from each of the four samples are given in Table 7.4. The estimated uncertainty due to the primary vertex position is $\sim 1.2 \mu m$.

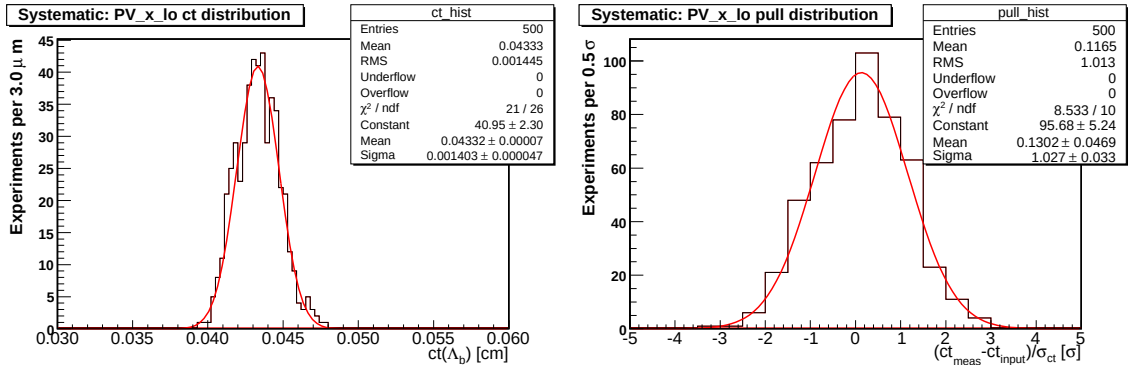

Figure 7.9: Left: The distribution of lifetime fit results from the baseline lifetime fit on Toy events generated from rigged primary vertex low *x* position PDF's. The results are fit with a Gaussian distribution shown in red. Right: the pull distribution for the Toy fits. The pull is defined as fit *ct* - rigged *ct* / fit σ_{ct}.

Sample	$\overline{ct_{Rig}}$ $[\mu m]$	$\overline{ct_{Toy}}$ $[\mu m]$	$\overline{ct^i_{Rig} - ct^i_{Toy}}[\mu m]$
High PV_x	432.6	431.5	0.8
Low PV_x	432.8	433.2	-0.7
High PV_y	432.1	432.2	-0.5
Low PV_y	433.4	432.5	1.2
Estimated Systematic Error			1.2

Table 7.4: Summary of the results from Toy Monte Carlo experiments to estimate the systematic error due to the uncertainty in the primary vertex position.

7.2.4 Data-Monte Carlo Agreement: Primary Vertex Errors

When reconstructing $\Lambda_b^0 \to \Lambda_c^+ \pi^-$ events, we reconstruct the primary vertices event-by-event using the PrimeVertexFinder algorithm which iteratively clusters prompt tracks along z axis.

In the the process of realistic Monte Carlo simulation, we thus need to reproduce the errors on the primary vertex finding that is seen in data. Since our realistic samples are produced with HQGen, there are no prompt tracks and these errors are parametrically simulated by generating random numbers from the sideband-subtracted distributions of primary vertex errors σ_x and σ_y. Thus the agreement of the primary vertex errors is excellent by construction.

Any kind of systematic that can be associated to this process is to include the fluctua-

tions on the sideband-subtracted data distributions. However, any kind of disagreement that could be artificially manufactured is much smaller than the disagreement that is brought with the data-to-MC *ct* scale factor, S_{ct}, which effectively stretches and compresses the whole distribution along the abcissa. So one expects that this systematics is much smaller than the systematics due to S_{ct} scale factor. However the latter is negligible, so thus the systematics due to primary vertex error data-MC (dis)agreement is also taken to be negligible.

7.2.5 Data-Monte Carlo Agreement: Λ_c^+ Dalitz Structure

The contributions of the different sub-components of the $\Lambda_c^+ \to pK^-\pi^+$ are uncertain in the Monte Carlo. The four dominant Λ_c^+ decays are considered; $\Lambda_c^+ \to pK^*$, $\Lambda_c^+ \to \Delta^{++}K^-$, $\Lambda_c^+ \to \Lambda(1520)\pi^+$, and non-resonant $\Lambda_c^+ \to pK^-\pi^+$. In the baseline analysis, the branching fractions are fixed to the PDG [8] values as described in Section 4.3.1.2. The Λ_c^+ branching fractions are poorly measured, with large uncertainty. Furthermore, our efforts to match the Monte Carlo Λ_c^+ branching fractions to those observed in data, were met with limited success (see Appendix D).

The systematic error, due to the Dalitz fractions, is therefore estimated very conservatively. Several random ensembles are generated; the value of each fraction is fluctuated, between $\pm 3\sigma$ of the PDG error, using a flat prior distribution. The fractions generated for each of the ensembles are listed in Table 7.5. The systematic is computed using Toy Monte Carlo as described above. The RMS of the resulting shifts from the baseline lifetime result

is quoted as the systematic. The distribution of the Toy lifetime fit results and the pull distribution for one ensemble are shown in Figure 7.10. The estimated uncertainty due to the Dalitz fraction uncertainty is $\sim 3.7 \mu m$.

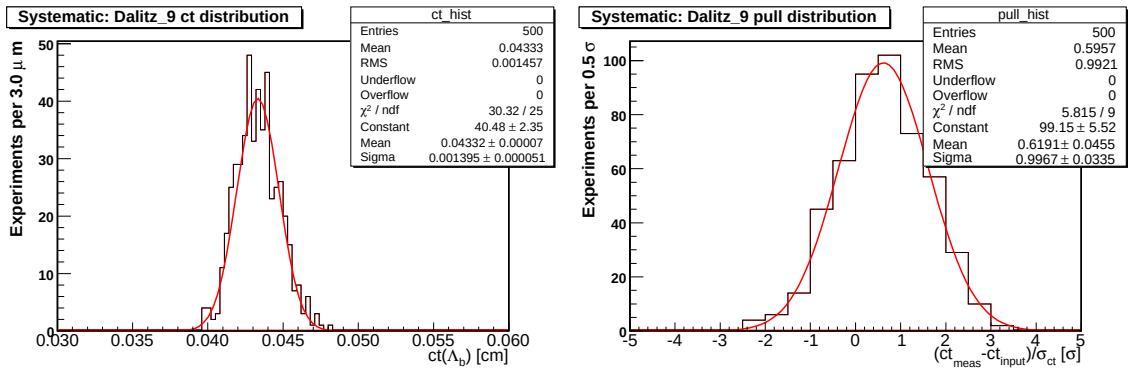

Figure 7.10: Left: The distribution of lifetime fit results from the baseline lifetime fit on Toy events generated from rigged Dalitz_9 PDF's. The results are fit with a Gaussian distribution shown in red. Right: the pull distribution for the Toy fits. The pull is defined as fit *ct* - rigged *ct* / fit σ_{ct}.

7.2.6 Data-Monte Carlo Agreement: Λ_b Polarization

The Λ_b^0 polarization in the signal Monte Carlo is re-weighted to match the angular distributions as described in Section 4.3.1.3. Only the production angle of the proton in the Monte Carlo is re-weighted. The re-weighting is done by computing the ratio of the distributions of the angle Θ_p in data and Monte Carlo, and fitting with a straight line to obtain the relative weight. The slope of the re-weighting fit is varied up and down by 1σ. The systematic is then computed using Toy Monte Carlo as described above. The distribution of the Toy lifetime fit results and their pull distribution for one -1σ test are shown in Figure 7.11. The results from both the $+$ and -1σ experiments are summarized

Sample	pK^*	$\Delta^{++}K$	$\Lambda(1520)\pi$	$pK\pi$	$\overline{ct_{Rig}}$ $[\mu m]$	$\overline{ct_{Toy}}$ $[\mu m]$	$\overline{ct^i_{Rig} - ct^i_{Toy}}[\mu m]$
PDG [8]	0.227 ± 0.071	0.122 ± 0.054	0.255 ± 0.085	0.397 ± 0.113	-	-	-
Dalitz_1	0.120	0.124	0.360	0.395	432.1	432.3	-0.9
Dalitz_2	0.174	0.109	0.262	0.455	430.1	433.0	-3.1
Dalitz_3	0.169	0.269	0.002	0.560	428.8	432.8	-4.3
Dalitz_4	0.204	0.085	0.316	0.394	433.2	433.4	0.0
Dalitz_5	0.099	0.240	0.101	0.560	430.2	434.0	-3.4
Dalitz_6	0.050	0.304	0.459	0.187	433.6	433.0	0.4
Dalitz_7	0.105	0.071	0.036	0.788	430.9	433.1	-2.5
Dalitz_8	0.309	0.199	0.259	0.233	429.8	432.9	-3.3
Dalitz_9	0.275	0.258	0.015	0.452	425.7	433.2	-7.6
Dalitz_10	0.243	0.285	0.205	0.267	429.3	434.2	-4.9
						Estimated Systematic Error (RMS)	3.7

Table 7.5: Λ_c^+ decay fractions used to evaluate the systematic error due to the Dalitz branching fraction uncertainty. The branching fraction of each mode is chosen between $\pm 3\sigma$ using a flat distribution to estimate the systematic error. The Right column lists the Λ_b^0 lifetime difference from the baseline when the listed fractions are used. The systematic is taken from the calculated RMS from the 10 Dalitz fraction ensembles.

in Table 7.6. The estimated systematic error due to the uncertainty in the polarization re-weighting is $1.4 \mu m$.

7.2.7 Data-Monte Carlo Agreement: Tracks firing the TTT

The signal Monte Carlo was re-weighted to match the distribution, found in data, of track-pairs satisfying the TTT as described in Section 4.3.1.4. The uncertainty in this re-weighting is evaluated as a source of systematic error. The central value assigned to each

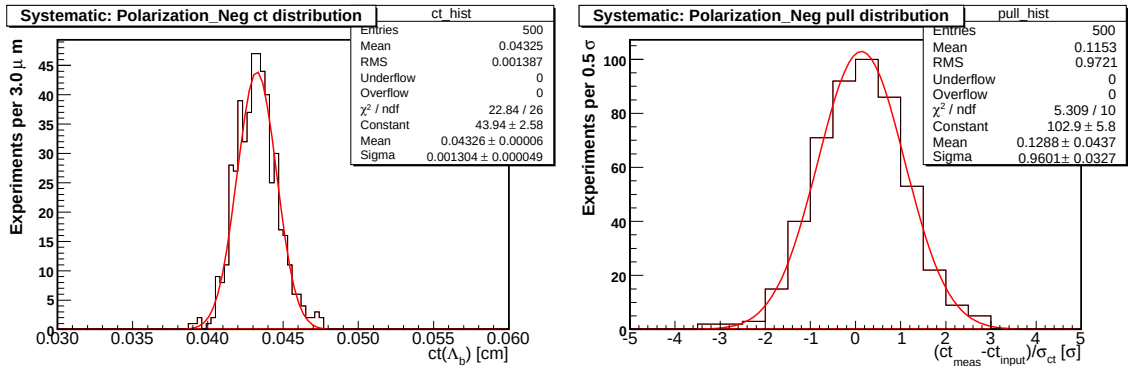

Figure 7.11: Left: The distribution of lifetime fit results from the baseline lifetime fit on Toy events generated from rigged Polarization -1σ PDF's. The results are fit with a Gaussian distribution shown in red. Right: the pull distribution for the Toy fits. The pull is defined as fit *ct* - rigged *ct* / fit σ_{ct}.

Sample	$\overline{ct_{Rig}}$ $[\mu m]$	$\overline{ct_{Toy}}$ $[\mu m]$	$\overline{ct^i_{Rig} - ct^i_{Toy}}[\mu m]$
Polarization $+1\sigma$	434.7	432.9	1.4
Polarization -1σ	430.9	432.6	-1.3
		Estimated Systematic Error	$1.4\mu m$

Table 7.6: Summary of the results from Toy Monte Carlo experiments to estimate the systematic error due to the uncertainty in the re-weighting of the proton production angle.

trigger track-pair is fluctuated using a Gaussian distribution with a width equal to the error on the track-pair. An example of one such fluctuation is shown in Figure 7.12. The results from the Toy experiment using this fluctuation are shown in Figure 7.13. A summary of all experiments is given in Table 7.7. The systematic error due to the uncertainty in the trigger track-pair re-weighting is $2.0\mu m$.

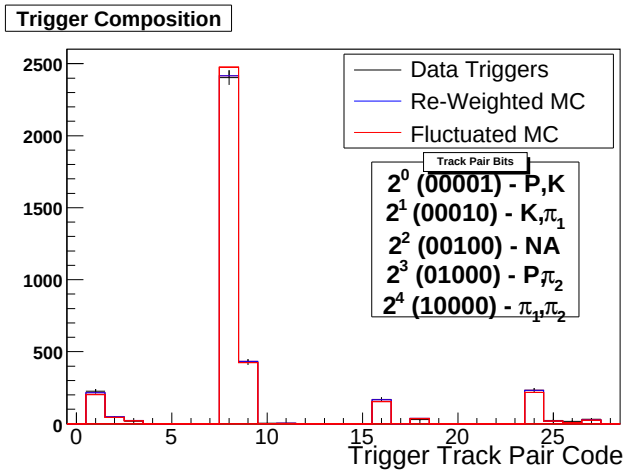

Figure 7.12: An example fluctuated trigger code distribution used to evaluate the systematic error.

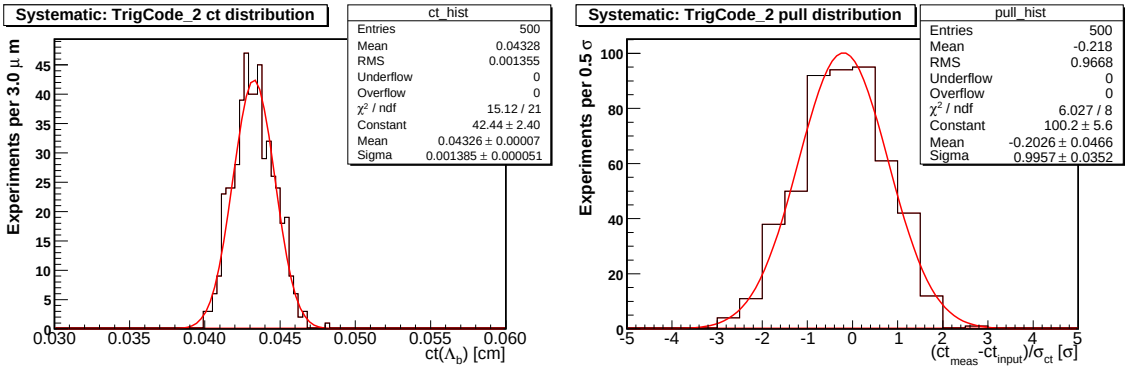

Figure 7.13: Left: The distribution of lifetime fit results from the baseline lifetime fit on Toy events generated from rigged TrigCode_2 PDF's. The results are fit with a Gaussian distribution shown in red. Right: the pull distribution for the Toy fits. The pull is defined as fit *ct* - rigged *ct* / fit σ_{ct}.

7.2.8 Data-Monte Carlo Agreement: $p_T(\Lambda_b)$ spectrum

The initial p_T spectrum of the Λ_b is not known precisely. In fact the best measurement comes from our own data sample. We re-weight the $p_T(\Lambda_b^0)$ of the Monte Carlo as described in Section 4.3.1.5. The fit used to re-weight the p_T spectrum is uncertain. We change the slope of this fit up and down by 1σ to evaluate the systematic error. The Toy

Sample	$\overline{ct_{Rig}}$ $[\mu m]$	$\overline{ct_{Toy}}$ $[\mu m]$	$\overline{ct^i_{Rig} - ct^i_{Toy}}[\mu m]$
TrigCode_1	431.8	432.4	-1.2
TrigCode_2	436.6	432.6	3.8
TrigCode_3	432.5	432.9	-0.6
TrigCode_4	433.4	432.8	0.5
TrigCode_5	430.4	431.6	-1.6
Quoted Systematic: (RMS)			2.0

Table 7.7: Summary of the Toy Monte Carlo experiments to estimate the systematic error due to the uncertainty in the re-weighting of the trigger track-pair distribution.

results from the experiment with the fit weighted down by 1σ are shown in Figure 7.14. The Results from both Toy experiments are summarized in Table 7.8. The systematic error due to the uncertainty in the p_T re-weighting is negligible.

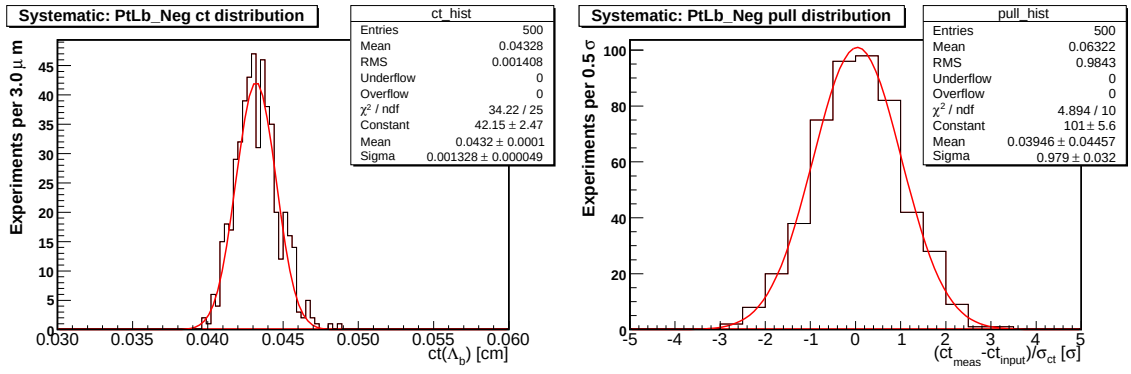

Figure 7.14: Left: The distribution of lifetime fit results from the baseline lifetime fit on Toy events generated from rigged $p_T(\Lambda_b^0) - 1\sigma$ PDF's. The results are fit with a Gaussian distribution shown in red. Right: the pull distribution for the Toy fits. The pull is defined as fit ct - rigged ct / fit σ_{ct}.

Sample	$\overline{ct_{Rig}}$ [μm]	$\overline{ct_{Toy}}$ [μm]	$\overline{ct^i_{Rig} - ct^i_{Toy}}$[$\mu m$]
$p_T(\Lambda_b^0) + 1\sigma$	431.2	432.0	0.4
$p_T(\Lambda_b^0) - 1\sigma$	434.1	433.3	-0.4
		Quoted Systematic:	negligible

Table 7.8: Summary of the Toy Monte Carlo experiments to estimate the systematic error due to the uncertainty in the re-weighting of the $p_T(\Lambda_b^0)$ spectrum.

7.2.9 Combinatorial *ct* template

The shape of the combinatorial background *ct* is modeled, in the baseline fit, with a Landau distribution to fit the *ct* distribution found in candidates from the upper sideband of data. We evaluate the sensitivity of the lifetime fit to this shape by using a different *ct* shape. The shape that is used for the systematic is a smoothed histogram of the *ct* of the same candidates in the upper sideband of data. The baseline and rigged combinatorial *ct* templates are shown overlayed in Figure 7.15. The Toy result is shown in Figure 7.16. The systematic error due to the shape of the combinatorial *ct* template is 2.9μm.

Sample	$\overline{ct_{Rig}}$ [μm]	$\overline{ct_{Toy}}$ [μm]	$\overline{ct^i_{Rig} - ct^i_{Toy}}$[$\mu m$]
Combinatorial *ct* Template	434.5	431.0	2.9
		Quoted Systematic:	2.9

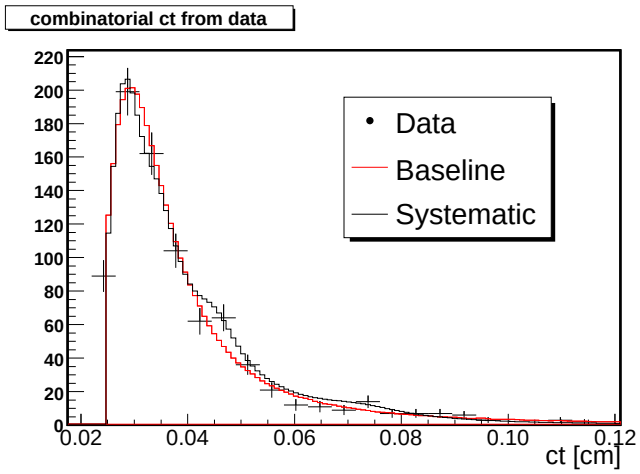

Figure 7.15: A comparison of the baseline (red) and systematic (black) combinatorial *ct* template shapes.

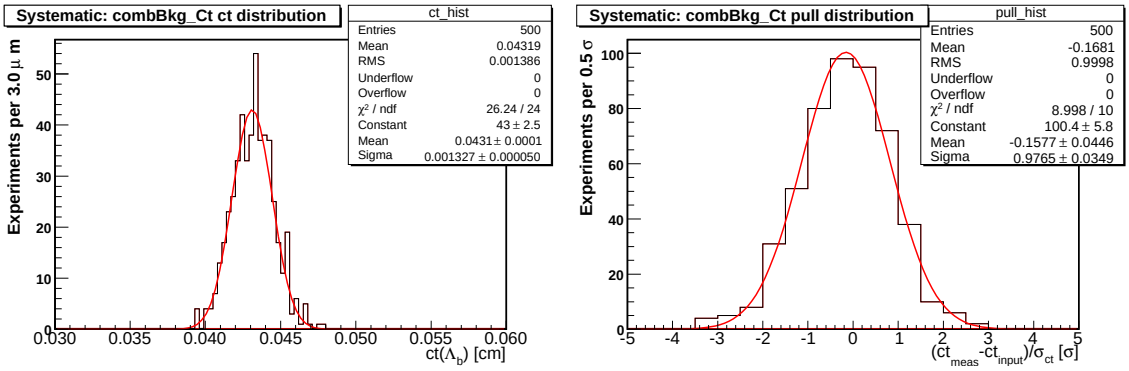

Figure 7.16: Left: The distribution of lifetime fit results from the baseline lifetime fit on Toy events generated from rigged combinatorial background template PDF. The results are fit with a Gaussian distribution shown in red. Right: the pull distribution for the Toy fits. The pull is defined as fit *ct* - rigged *ct* / fit σ_{ct}.

7.2.10 B^0 SVT Efficiency

The default B^0 background efficiency is computed using a sample of about $80,000$ $B^0 \to D^+\pi^-$ decays reconstructed as $\Lambda_b^0 \to \Lambda_c^+\pi^-$ as described in Section 5.5.2. The systematic error associated with the shape of the B^0 efficiency is estimated by computing a rigged efficiency from a subset of the $B^0 \to D^+\pi^-$ Monte Carlo events that pass much tighter mass cuts on the reconstructed $D^+\pi^-$ track pair. The resulting sample consists of about $9,000$ events. The Toy results are shown in Figure 7.17. The systematic error quoted due to the uncertainty in the B^0 efficiency is 1.0μm.

Sample	$\overline{ct_{Rig}}$ $[\mu m]$	$\overline{ct_{Toy}}$ $[\mu m]$	$\overline{ct^i_{Rig} - ct^i_{Toy}}[\mu m]$
Rigged B^0 Efficiency	431.7	432.9	-1.0
		Quoted Systematic:	1.0

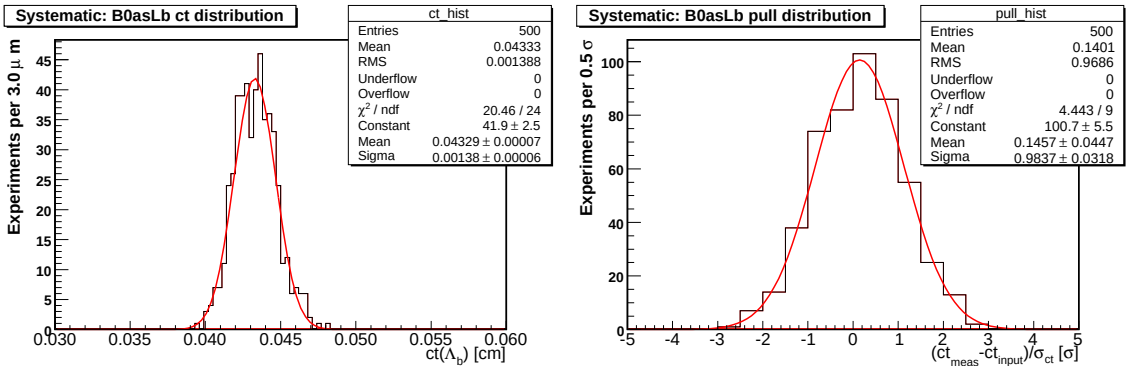

Figure 7.17: Left: The distribution of lifetime fit results from the baseline lifetime fit on Toy events generated from the rigged B^0 efficiency PDF. The results are fit with a Gaussian distribution shown in red. Right: the pull distribution for the Toy fits. The pull is defined as fit ct - rigged ct / fit σ_{ct}.

7.2.11 True B^0 lifetime

The value of the true B^0 lifetime is set to a constant ($c\tau(B^0) = 460 \pm 10\mu m$ [8]) for the B meson background ct templates. In order to evaluate the sensitivity of the fit to the value of the B^0 lifetime, Toy experiments are run with $c\tau(B^0)$ set to 450 and 470μm (*i.e.* $\pm 1\sigma$ of the PDG central value). The result from the $c\tau(B^0) = 450\mu m$ experiment is shown in Figure 7.18. The results of both Toy experiments are summarized in Table 7.9. The systematic error due to the value of the true B^0 lifetime is $\sim 1.0\mu$m.

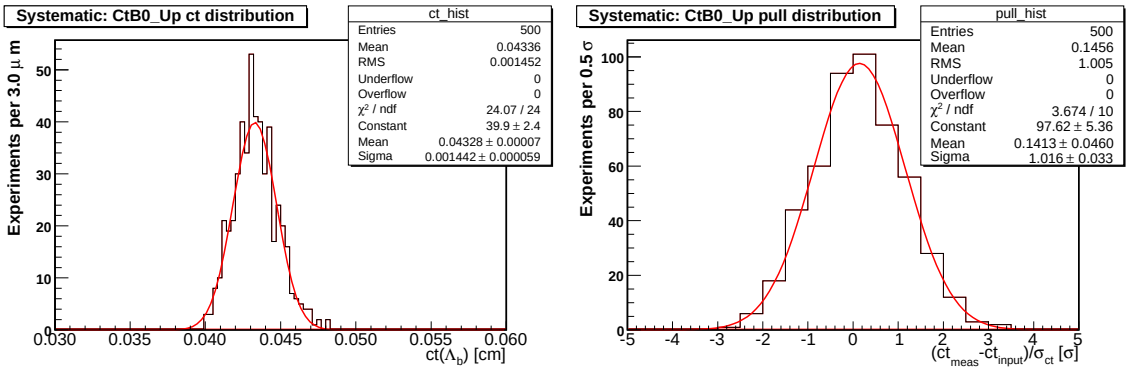

Figure 7.18: Left: The distribution of lifetime fit results from the baseline lifetime fit on Toy events generated from rigged $c\tau(B^0) = 470\mu$m PDF's. The results are fit with a Gaussian distribution shown in red. Right: the pull distribution for the Toy fits. The pull is defined as fit ct - rigged ct / fit σ_{ct}.

Sample	$\overline{ct_{Rig}}$ $[\mu m]$	$\overline{ct_{Toy}}$ $[\mu m]$	$\overline{ct^i_{Rig} - ct^i_{Toy}}[\mu m]$
$c\tau(B^0) = 470\mu m$	430.8	432.8	-0.8
$c\tau(B^0) = 450\mu m$	432.3	433.1	0.9
		Quoted Systematic:	1.0

Table 7.9: Summary of the Toy Monte Carlo experiments to estimate the systematic error due to the uncertainty on the true B^0 lifetime.

7.2.12 Λ_c^+ lifetime

The lifetime of the Λ_c^+ is set to 60μm in the default HQGen sample. To estimate the systematic error due to the assumed Λ_c^+ lifetime, the sample is re-weighted such that $c\tau(\Lambda_c^+) = 66\mu$m. Based on this re-weighted sample, an efficiency is generated and Toy experiments are run. The rigged Λ_c^+ lifetime efficiency results in a shift of $< 1\mu$m in the $c\tau(\Lambda_b^0)$ fit. The systematic error due to the Λ_c^+ lifetime is negligible.

7.2.13 Si simulation effects: Scale factor

As has been previously described, a global scale factor was introduced to correct for underestimated *ct* errors. To evaluate the sensitivity of the lifetime fit to the value of this scale factor, the value used in the fit is changed by $\pm$20%. The scale factors, S_1 and S_2, used to scale the the narrow and the broad Gaussians in our resolution function are varied. The results from the Toy experiments used to evaluate this effect are summarized in Table 7.10. Variation of the global σ_{ct} scale factor produce negligible changes in the final result of the Λ_b^0 lifetime.

7.2.14 Impact Parameter Correlation

We quote a systematic of 1.0 μm from Ref. [1].

Sample	$\overline{ct_{Rig}}$ $[\mu m]$	$\overline{ct_{Toy}}$ $[\mu m]$	$\overline{ct^i_{Rig} - ct^i_{Toy}}[\mu m]$
$S+20\%$	431.5	433.0	0.1
$S-20\%$	431.5	432.5	0.1
		Quoted Systematic:	negligible

Table 7.10: Summary of the Toy Monte Carlo experiments to estimate the systematic error due to the uncertainty on global scale factor.

7.2.15 Summary of systematic uncertainties

The sources of systematic uncertainty described above are listed in Table 7.11. The total systematic uncertainty is computed by adding all sources of systematic error in quadrature. Our total systematic error, thus obtained, is 8.8 μm.

Description	**Value** $[\mu m]$
Alignment	2.0
SVT-SVX d0 correlation	1.0
Background Normalizations	1.0
Mass Template Shapes	negligible
SVT Model	6.3
Data-MC Agreement: Λ_c^+ Dalitz structure	3.7
Combinatorial *ct* Template	2.9
Data-MC Agreement: TrigCode re-weighting	2.0
Data-MC Agreement: Λ_b^0 polarization	1.4
Data-MC Agreement: Primary Vertex Position	1.2
B^0 Efficiency	1.0
B^0 Lifetime	1.0
Data-MC Agreement: $pt(\Lambda_b^0)$ spectrum	negligible
σ_{ct} Scale Factor	negligible
Fitter Bias	negligible
σ_{ct} Binning	negligible
Λ_c^+ Lifetime	negligible
Data-MC Agreement: Primary Vertex Error	negligible
Total Systematic Uncertainty	8.8

Table 7.11: Summary of the systematic uncertainties. The first group listed in the table are non-SVT-biased sources of systematic error. The total systematic uncertainty is obtained by adding the result of all systematics in quadrature.

Chapter 8

Conclusion

Analyzing a sample of ∼3,000 fully reconstructed $\Lambda_b^0 \to \Lambda_c^+ \pi^-$ decays from $1070 \pm 60 pb^{-1}$ of data, collected with CDF's two displaced track trigger, we measure the lifetime of the Λ_b^0 baryon to be;

$$c\tau(\Lambda_b^0) = 422.8 \pm 13.8 \text{ (stat)} \pm 8.8 \text{ (syst) } \mu\text{m}.$$

Or, expressed in picoseconds as;

$$\tau(\Lambda_b^0) = 1.410 \pm 0.046 \text{ (stat)} \pm 0.029 \text{ (syst) ps}.$$

Using the current world average for B^0 lifetime [48] we obtain:

$$\tau(\Lambda_b^0)/\tau(B^0) = 0.922 \pm 0.039.$$

In Figure 8.1 this result is compared with the current world average [48] and previous measurements of $\tau(\Lambda_b^0)$. This is the world's single most precise measurement of the Λ_b^0

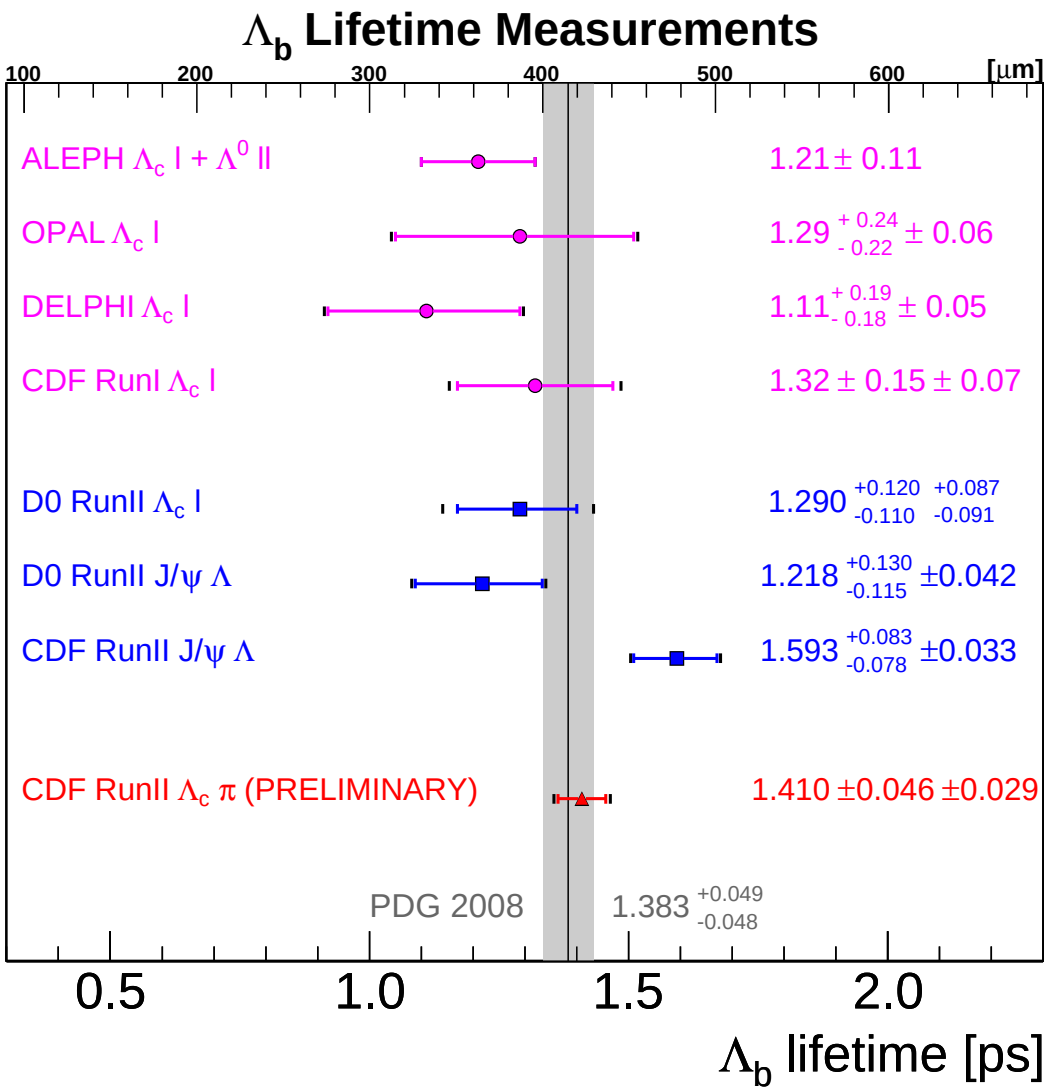

Figure 8.1: Our Λ_b^0 lifetime measurement is compared with the current world average (PDG 2007) and all measurements contributing to it.

lifetime. We see excellent agreement between our result and the current world average and good agreement with the HQE predictions of $\tau(\Lambda_b^0)/\tau(B^0)$ between 0.88 and 0.94 as described in Section 1.3.2.

Precise measurements of hadronic masses and lifetimes are the most effective way to constrain the predictions of QCD. In particular, the non-perturbative effects of QCD are important because without a sound theoretical model, it may be impossible to identify physics beyond the Standard Model in indirect searches. Although this measurement is still statistically limited, it is the best of its kind – better than all of the previous measurements combined. This measurement conclusively resolves the apparent discrepancy between the previous Λ_b^0 lifetime measurements and the 2006 CDF measurement. Furthermore, it also agrees with the latest theory predictions, confirming the HQE model of the decays of beautiful baryons.

Appendix A

CDF Calorimeter and Muon Systems

A.1 Calorimeter Systems

The calorimeter systems are located outside of the solenoid and encapsulate the entire tracking volume. The calorimeters are separated into two main physical systems; central calorimeters that are configured cylindrically around the beam line, and plug calorimeters that are located forward of the tracking region, at high pseudorapidity. Each system is comprised of two types of calorimeters; an inner, electro-magnetic calorimeter and an outer, hadronic calorimeter. Both types of calorimeters consist of alternating layers of scintillator and absorber (lead for the electro-magnetic and iron in the case of the hadronic calorimeter). A third, end-wall, hadronic calorimeter fills the coverage gap between the central and plug calorimeters.

All of the calorimeters are segmented in azimuth and pseudorapidity to form towers

that point back towards the interaction point on the beamline. Calorimeter data is matched to tracks and jets found in the tracking system, and used to measure the track energy. The calorimeters cover the region $|\eta| < 3.64$ and the full 2π aziumuthlly. In addition, drift chambers embeded in the electromagnetic calorimeters provide position and profile information on the point of shower maximum. Similar pre-shower detectors are also located between the solenoid and the electro-magnetic calorimeters to help match tracks to towers.

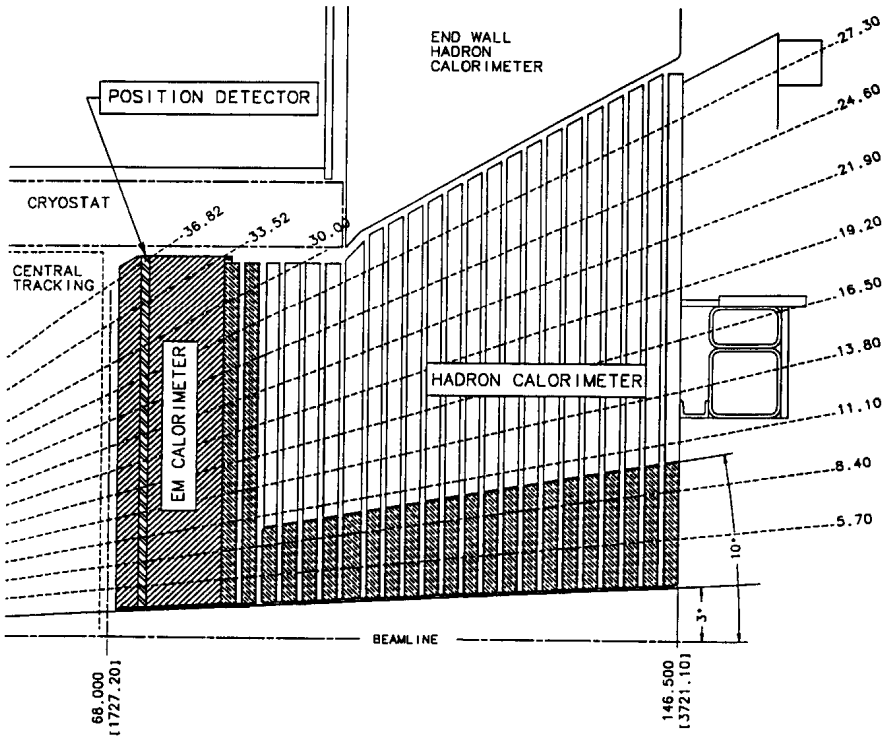

Figure A.1: CDF plug calorimeter upgrade.

A.2 Muon Detectors

The muon detectors are made up of scintillators and drift chambers located on the perimeter of the other detector systems. The muon detectors are comprised of four detector sub-systems that provide coverage at different places on the detector. The Central Muon Detector (CMU) covers the central region ($|\eta| < 0.6$) and is embeded in the outer edge of the calorimeter wedges. The Central Muon Upgrade (CMP) also covers the central region, but is separated from the CMU by an additional two feet of steel to reduce the noise from non-muon events.

The Central Muon Extension (CMX) consists of arches arranged at each end of the central detector, extending in polar angle from 42^0 to 55^o. The CMX provides some overlap with the CMU and CMP and extends the coverage in pseudorapidity to $|\eta| = 1.0$. The CMX has a 30^o gap at the top of the CDF detector. Furthermore, on the bottom of CDF, the CMX is interrupted by the floor of the collision hall, here, the CMX coverage is patched with a fan-shaped section called the “miniskirt”.

The Intermediate Muon System (IMU) is a barrel of CMP-like chambers that surround the beamline on either side of the detector. Counters on the endplate and inside the IMU barrel help to reject background in order to more reliably track only muons. The IMU can trigger on muons up to $|\eta| = 1.5$ and can be used in conjunction with the tracking systems to track muons up to $|\eta| = 2.0$.

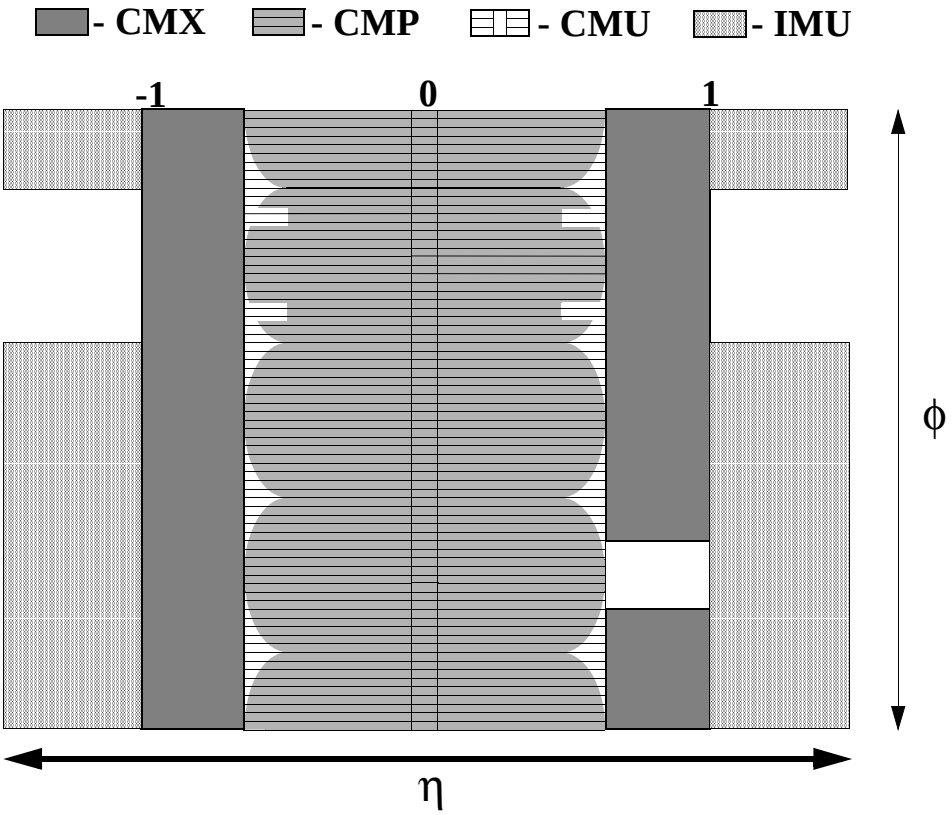

Figure A.2: CDF Muon coverage.

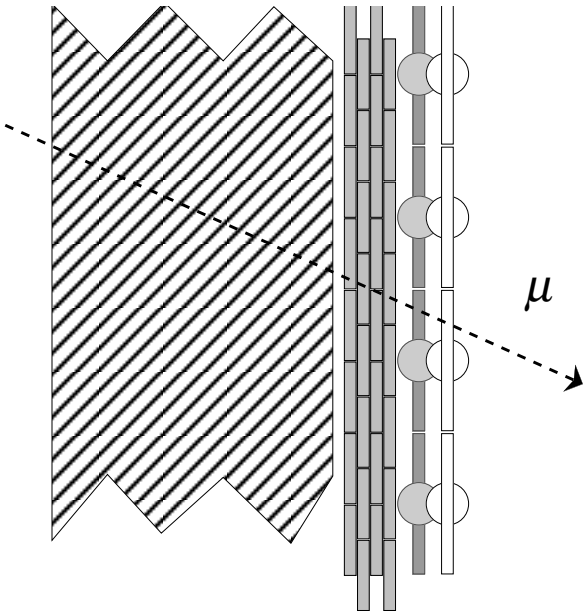

Figure A.3: CDF Muon counter schematic.

Appendix B

Universal Finder Reconstruction

```
if { $UFIND_DO_PID == 1 } {
  mod enable  CT_TrackingModule
  talk CT_TrackingModule
       NoTracking set t
  exit

  module enable TofModule
  set UFIND_PID_MODULES "CT_TrackingModule TofModule"
} else {
  mod disable CT_TrackingModule
  mod disable TofModule
  set UFIND_PID_MODULES ""
}

talk CalibrationManager
  ProcessName set PROD_PHYSICS_CDF
      PassName set 16
exit

talk PuffModule
   puffOnly set StorableRun2SiStripSet SiClusterSet SiHitSet
exit

mod enable  Prereq
```

```
talk        Prereq
   if { $UFIND_IS_REALMC == 1 } {
      bankType set "Simulated Trigger Bank"
   }
   bankType list
   L1Accept       set true
   L2Accept       set true
   L3Accept       set false
   L3TriggerNames set B_CHARM B_CHARM_L1_DPS
   show
exit

talk GeometryManager
   #  TOF geometry model set to Survey
   TofGeometryMenu
     # Other options: Nominal, Naive
     GeometryModel set Survey
   exit

   #--- Misalignment in MC set in SiliconGeometryMenu
   SiliconGeometryMenu
     L00Alignment       set true
     AlignmentPrint     set 3
     AlignmentSource set default
     #--- Simulation of Si passive material
     BuildPassive set t
     CreatePhantomLayer set true
     PhantomLayerRmin set 14.8  14.8  14.8  14.8  14.8  20.5   20.5   20.8  20.5  2
     PhantomLayerZmin set -100  -45   -15   15.1  46    -100   -45   -15    15.1  4
     PhantomLayerZmax set -46   -15.1 15    45    100   -46    -15.1  15    45    1
     PhantomLayerThickness set 2.8 0.9 0.8 0.9 2.8 0.38 0.524  0.232  0.524  0.38
     PhantomLayerMaterial set BERYLLIUM BERYLLIUM BERYLLIUM BERYLLIUM BERYLLIUM
BERYLLIUM BERYLLIUM BERYLLIUM BERYLLIUM BERYLLIUM
     PhantomLayerContainer set SVCC SVCC SVCC SVCC SVCC ISLC ISLC ISLC ISLC ISLC
  exit
exit


#--- No use for TrackSelectorModule in QuickSim
talk TrackSelectorModule
   #--- Cuts for the Std track views
   trackCutManager
```

```
      cut errCut  = HasHelixFit && PhysicalError
      cut ptCutL  = Pt > 1.3
      cut myptCut = Pt > 0.5
      cut etaCut  = AbsEta < 2.0
      # 2 SL AX (5 hits), 2 SL ST (5 hits)
      cut cotCut  = HasCOTHits 0 0 2 2 5 5
      # 3 AX Si hits
      cut svxCut  = HasSVXIIHitLayers 3 0 0 0
      #
      cut K_std   = etaCut && svxCut && cotCut && myptCut && errCut
      cut pi_std  = etaCut && svxCut && cotCut && myptCut && errCut
      cut pi_soft = etaCut && errCut
      cut p_std   = errCut && svxCut && cotCut && Pt > 2.0 && AbsEta < 1.3
      cut mu_std  = etaCut && svxCut && cotCut && ptCutL  && errCut
   exit

   inputTracks set defTracks

   #--- Track Refitting
   trackRefit
      refitTracks set true
      if { $USEL00 == 1 } {
  dropL00     set false
  L00Refit    set true
      } else {
  dropL00     set true
  L00Refit    set false
      }
      dropISL              set false
      #--- Refit method (KAL vs G3X)
      refitMethod          set KAL
      #--- Rescale COT covariance matrix
      rescaleCOTCov        set true
      curvCOTFactor        set 21.72
      d0COTFactor          set 11.57
      phi0COTFactor        set 14.64
      lambdaCOTFactor      set 1.544
      z0COTFactor          set 1.71
      show
   exit
exit
```

```
if { $UFIND_DO_PID == 1 } {
    set doPid true
} else {
    set doPid false
}

talk TrackAssocModule
   #--- Pions
   pi_Std_Assoc
     enabled     set t
     doSvt       set t
     doDedx      set $doPid
     doTof       set $doPid
     correctDedx set $doPid
   exit

   #--- Soft pions
   pi_Soft_Assoc
     enabled     set t
     doSvt       set t
     doDedx      set $doPid
     doTof       set $doPid
     correctDedx set $doPid
   exit

   #--- Kaons
   K_Std_Assoc
     enabled     set t
     doSvt       set t
     doDedx      set $doPid
     doTof       set $doPid
     correctDedx set $doPid
   exit

   #--- Protons
   p_Std_Assoc
     enabled     set t
     doSvt       set t
     doDedx      set $doPid
     doTof       set $doPid
     correctDedx set $doPid
   exit
```

```
   #--- Muons
   mu_Std_Assoc
      doMuons set true
      doSvt   set true
      doDedx  set false
      doTof   set false
   exit

exit
```

Appendix C

Data vs. Monte Carlo Kinematic Comparison

The following plots show the agreement between the side-band subtracted data (blue data points) and the re-weighted, realistic signal Monte Carlo (red histograms).

C.1 Λ_b^0 Quantities

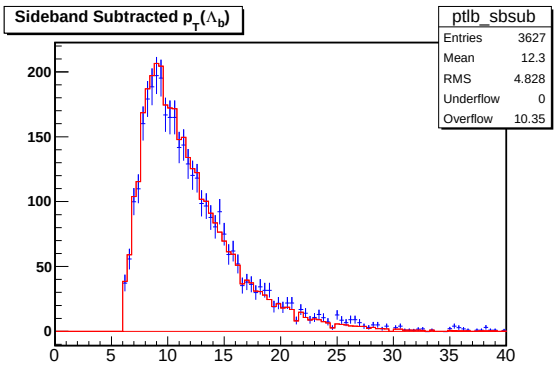

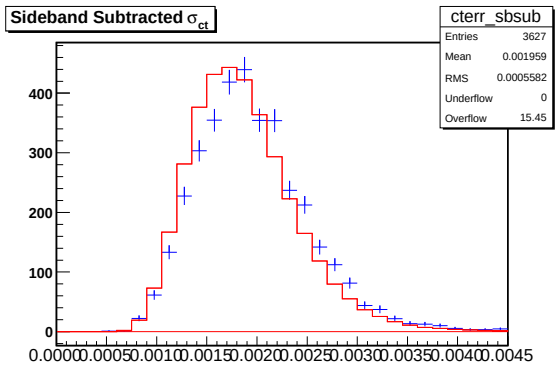

APPENDIX C. DATA VS. MONTE CARLO KINEMATIC COMPARISON

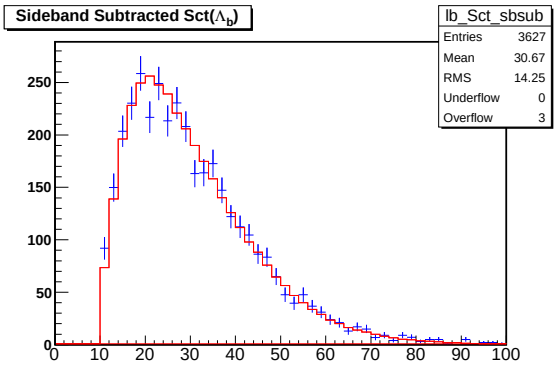

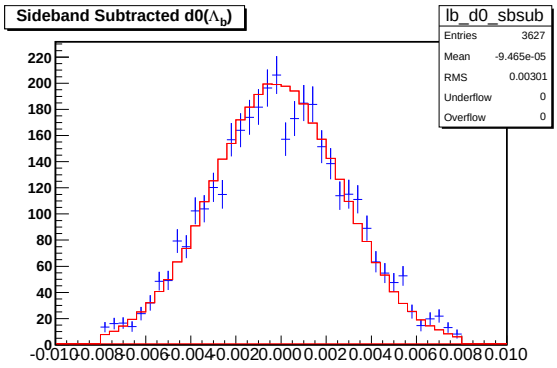

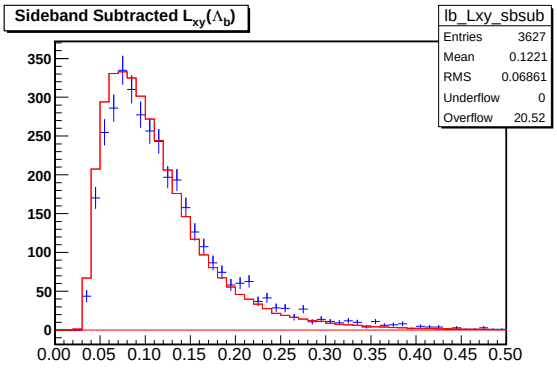

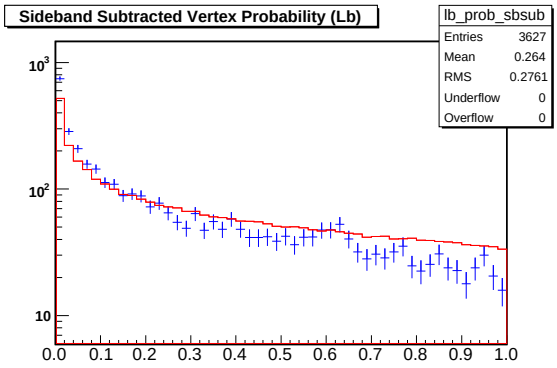

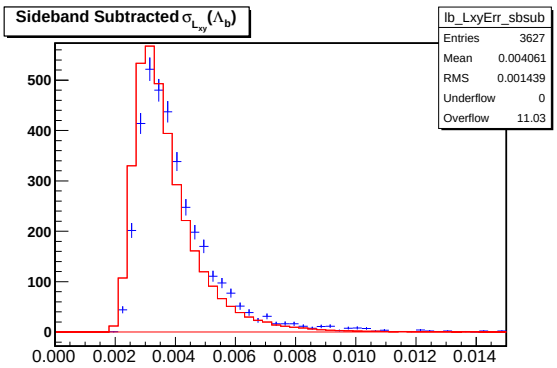

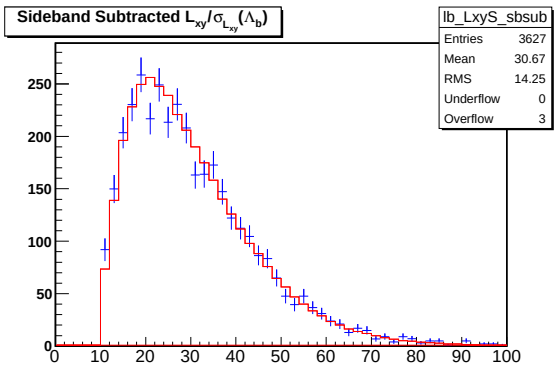

C.2 Λ_c^+ Quantities

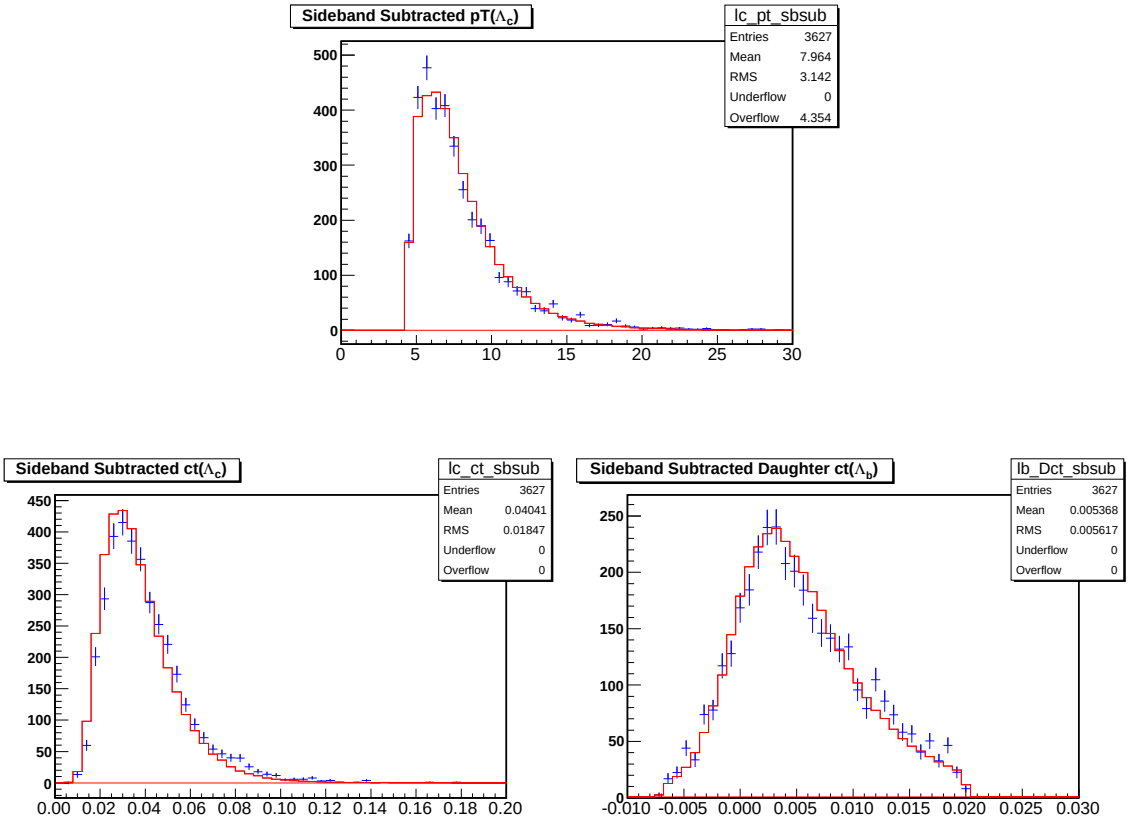

Figure C.1: Left: $ct(\Lambda_c^+)$ calculated w.r.t the primary vertex. Right: $ct(\Lambda_c^+)$ calculated w.r.t the decay of the Λ_b^0 . The Λ_c^+ lifetime is $\sim 60\mu$m and so we include the negative resolution tail up to -70μm.

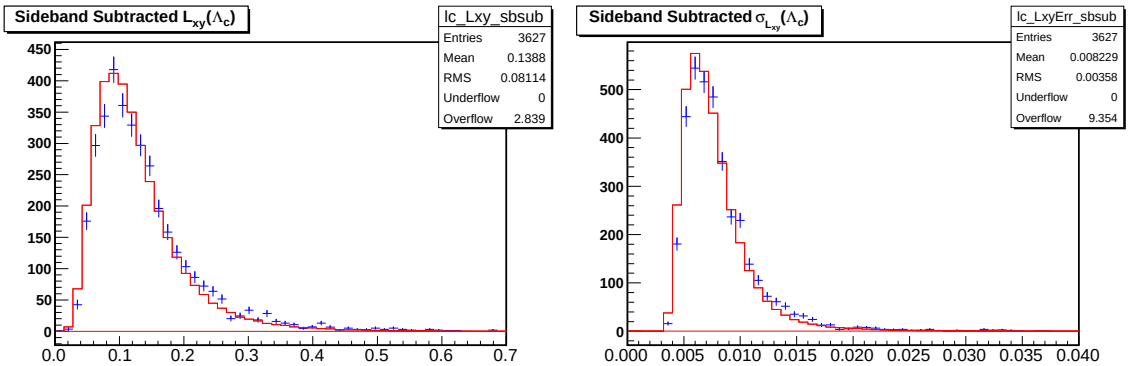

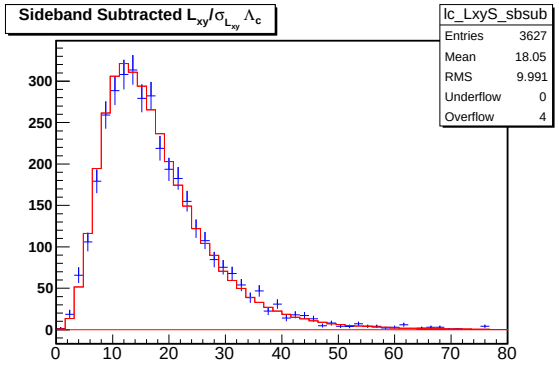
Sideband Subtracted $L_{xy}/\sigma_{L_{xy}}$ Λ_c
lc_LxyS_sbsub
Entries 3627
Mean 18.05
RMS 9.991
Underflow 0
Overflow 4
300
250
200
150
100
50
0
0
10
20
30
40
50
60
70
80

C.3 Track Quantities

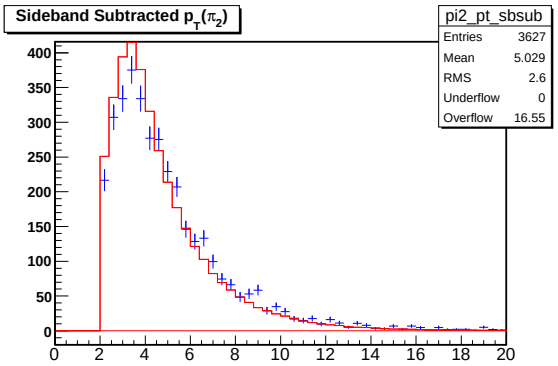

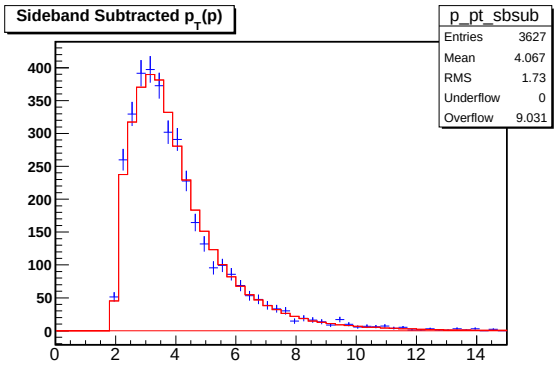

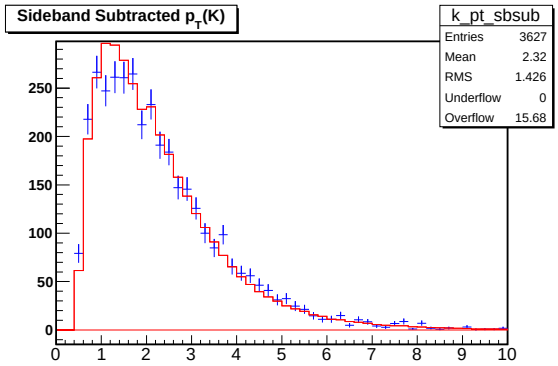

C.4 Primary Vertex Quantities

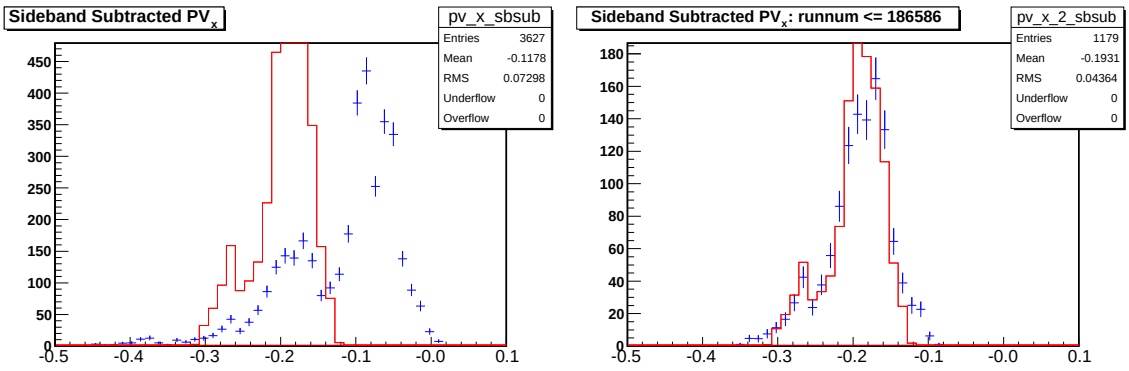

Figure C.2: Version `5.3.4` of the B group Monte Carlo package only includes SVT beamline information up to and including run number 186586. The data includes runs numbers as high as 212133. As a result, the data and Monte Carlo agreement is poor (Left). If we compare only up to run number 186586, the agreement is much better (Right).

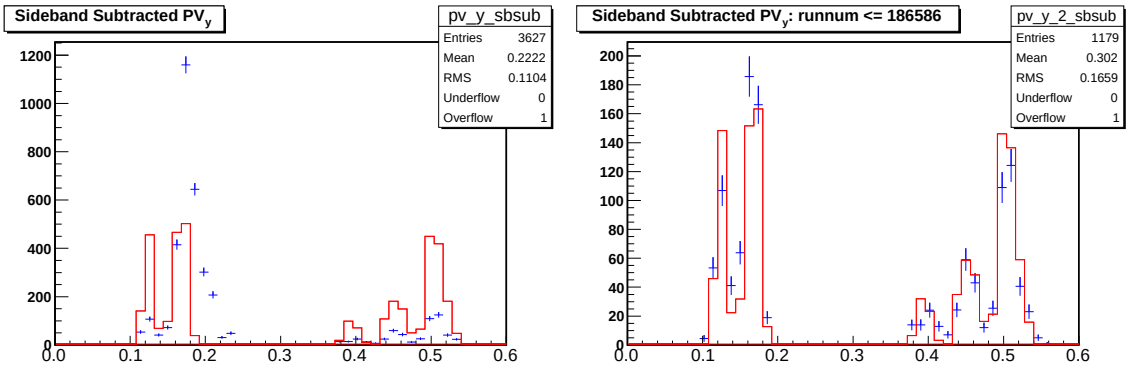

Figure C.3: Comparison of the Primary Vertex *y* position for all runs (Left). The agreement is poor because the Monte Carlo does not simulate the beam position properly for run numbers above 186586. The same comparison when data below run number 186586 is used is shown on the Right.

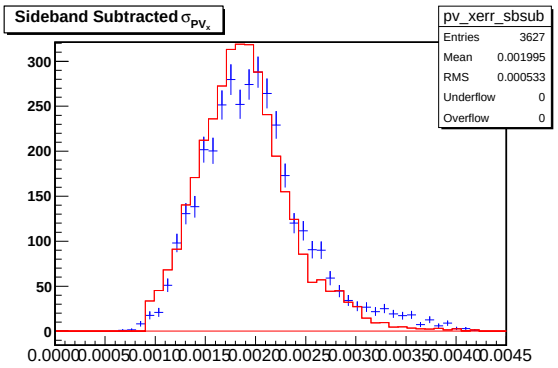
Sideband Subtracted σ_{PV_x}
pv_xerr_sbsub
Entries 3627
Mean 0.001995
RMS 0.000533
Underflow 0
Overflow 0
300
250
200
150
100
50
0
0.0000 0.0005 0.0010 0.0015 0.0020 0.0025 0.0030 0.0035 0.0040 0.0045

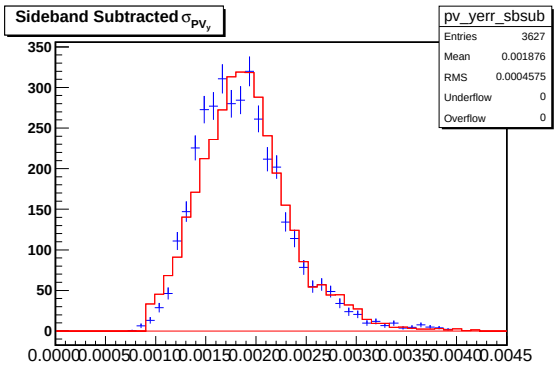
Sideband Subtracted σ_{PV_y}
pv_yerr_sbsub
Entries 3627
Mean 0.001876
RMS 0.0004575
Underflow 0
Overflow 0
350
300
250
200
150
100
50
0
0.0000 0.0005 0.0010 0.0015 0.0020 0.0025 0.0030 0.0035 0.0040 0.0045

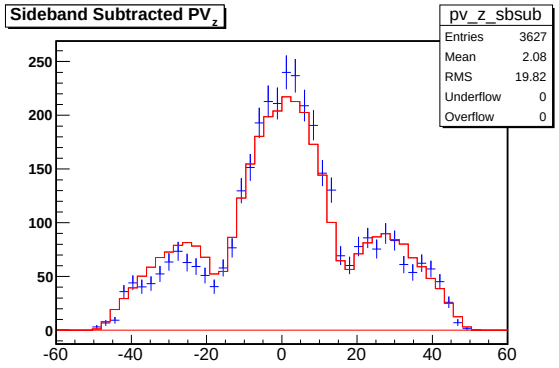
Sideband Subtracted PV_z
pv_z_sbsub
Entries 3627
Mean 2.08
RMS 19.82
Underflow 0
Overflow 0
250
200
150
100
50
0
-60 -40 -20 0 20 40 60

Appendix D

Studies on Λ_c^+ 3-body Decay Dalitz Structures

The current knowledge on Λ_c^+ 3-body decays, compiled by PDG [8], comes from a resonance amplitude analysis [49] by the E791 Collab., Fermilab. Making use of a sample of about 950 Λ_c^+ decays they extract the branching fractions for the 3 resonant modes, $\Lambda_c^+ \to pK^*(890)$, $\Lambda_c^+ \to \Delta^{++}K^-$ and $\Lambda_c^+ \to \Lambda(1520)\pi^+$, and the non-resonant $\Lambda_c^+ \to pK^-\pi^+$ mode from a likelihood fit. The measured fractions add up close to unity, while no such constraint is imposed in the fit. From this they infer a negligible contribution of interferences among the resonant amplitudes.

We use EvtGen decay package to generate Λ_c^+ 3-body decays, where the $\Lambda_c^+ \to pK^*(890)$ and $\Lambda_c^+ \to \Delta^{++}K^-$ decays are handled by the JETSET model, while the $\Lambda_c^+ \to \Lambda(1520)\pi^+$ and the non-resonant decays are handled by a generic phase space (PHSP)

model. We mix these modes according to the results from the E791 results [49] to make our realistic MC sample for Λ_b^0 lifetime analysis. Shown in Fig. D.1 a comparison of Λ_c^+ decay Dalitz plots between sideband subtracted data and realistic MC, mixed according to PDG fractions. As seen in the projection (bottom) plots, several structures are different

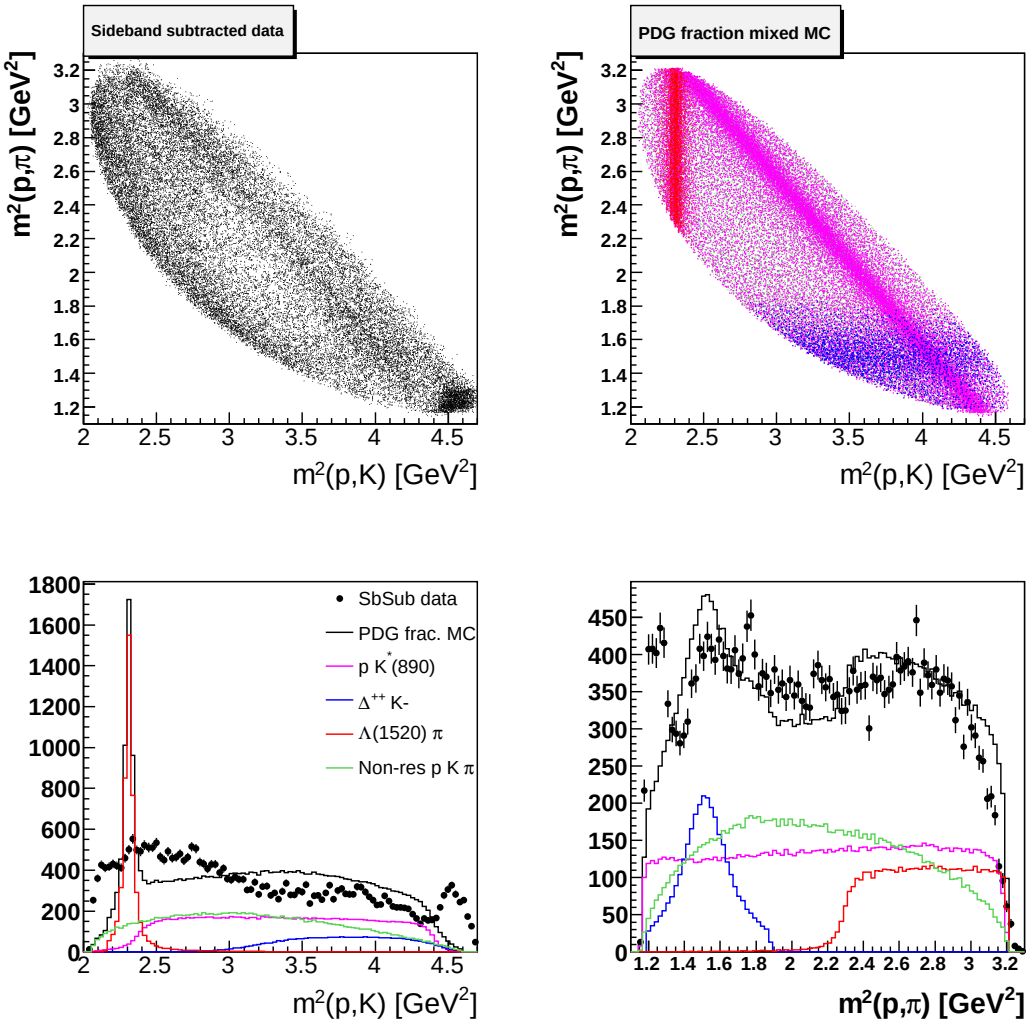

Figure D.1: Comparison of Λ_c^+ decay Dalitz plots of sideband subtracted data (top left) and realistic MC, mixed according to PDG fractions (top right). Also shown in the bottom plots are projections along x (bottom left) and y (bottom right) axes.

between data and MC. Especially, the bump at $m^2(p,K) = 4.5\ GeV^2$ and $m^2(p,\pi) = 1.3$

GeV^2 seen in the data scatter plot is missing entirely from MC. Also, the contribution for $\Lambda_c^+ \to \Lambda(1520)\pi^+$ seems to be way too large in realistic MC compared to the data. These discrepancies may arise due to two broad reasons; if the models used in EvtGen for the resonant modes are inadequate, and/or if contrary to the E791 findings, the interferences between the resonant modes are important. These issues are too complicated to be resolved without a complete helicity amplitude analysis, which is beyond the scope of our analysis.

Due to the apparent problem of the $\Lambda_c^+ \to \Lambda(1520)\pi^+$ contribution the first thing we attempted is to extract relative fractions of the 4 modes by a simple 2-D χ^2 fit to the sideband subtracted data. Assuming E791's result we constrained the fractions to add up to unity. Also we imposed a $m^2(p,K)$ ¡ 4.4 GeV^2 cut to remove the bump discussed in the previous paragraph. The resulting distributions are shown in Fig. D.2. As seen, the fit prefers the non-resonant mode fraction to be very large (85%). Although the fitted fractions improve the data and MC comparison significantly, the distributions are still quite different and unacceptable.

Next we explored reweighting the non-resonant mode to the sideband subtracted data, assuming that all the kinematic info. about Λ_c^+ decays, relevant to our analysis, are contained in the Dalitz plots. Fig. D.3 shows a comparison between Dalitz plots for sideband subtracted data and the non-resonant MC reweighted to it. Note that we imposed a $m^2(p,K)$ ¡ 4.4 GeV^2 cut to remove the bump in the bottom-right corner of the data Dalitz plot from the reweighting procedure, although it is displayed in the plots for completeness. Starting from a 180 K non-resonant events we reduce to about 34 K events after Dalitz reweighting.

APPENDIX D. STUDIES ON Λ_C^+ 3-BODY DECAY DALITZ STRUCTURES

With the rest of the reweightings imposed this sample reduces to about 19 K events, which are not sufficient to produce a stable SVT efficiency histogram. To continue pursuing this method, we are currently considering to multiply our non-resonant MC sample, which unfortunately requires significant CAF resources. If this method becomes usable the relevant systematic is expected to be significantly smaller than its current value of 9 μm.

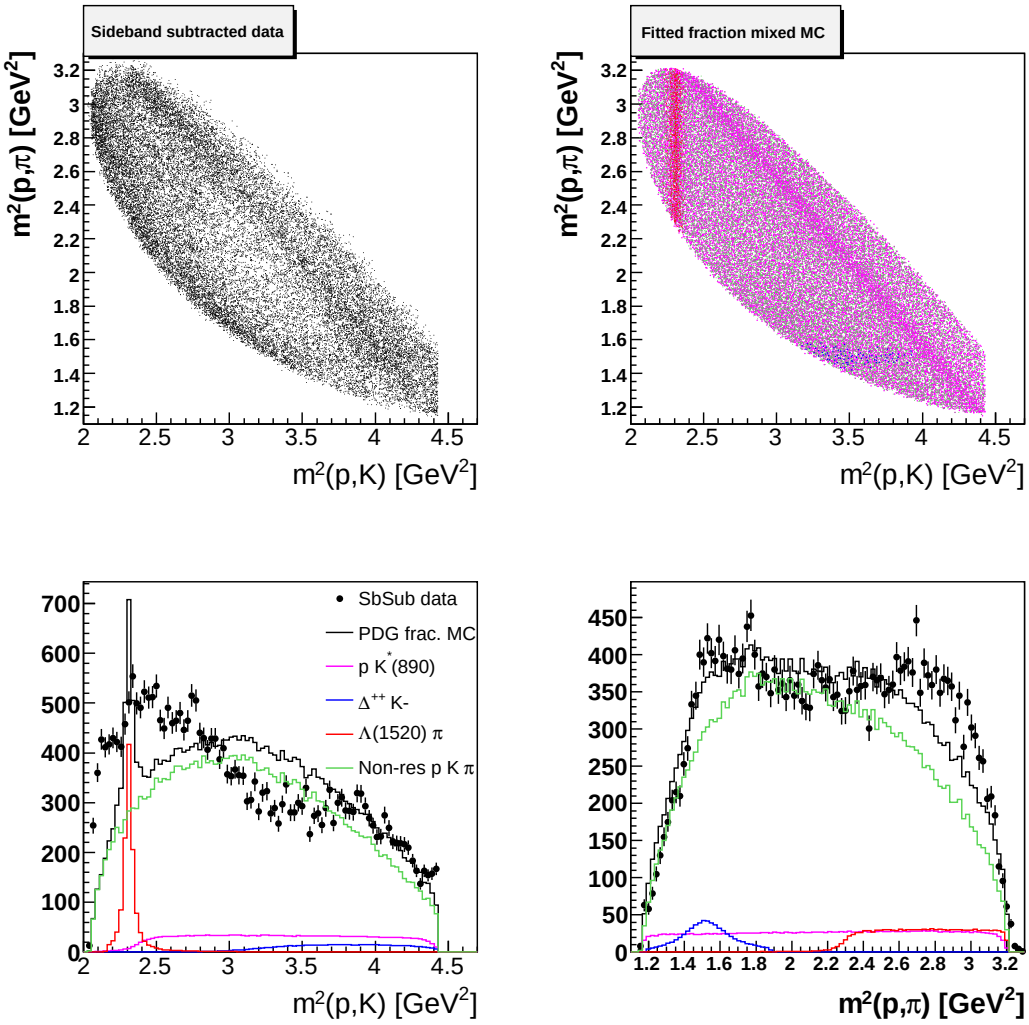

Figure D.2: Comparison of Λ_c^+ decay Dalitz plots of sideband subtracted data (top left) and realistic MC, mixed according to fractions extracted from a 2-D χ^2 fit (top right). Also shown in the bottom plots are projections along x (bottom left) and y (bottom right) axes.

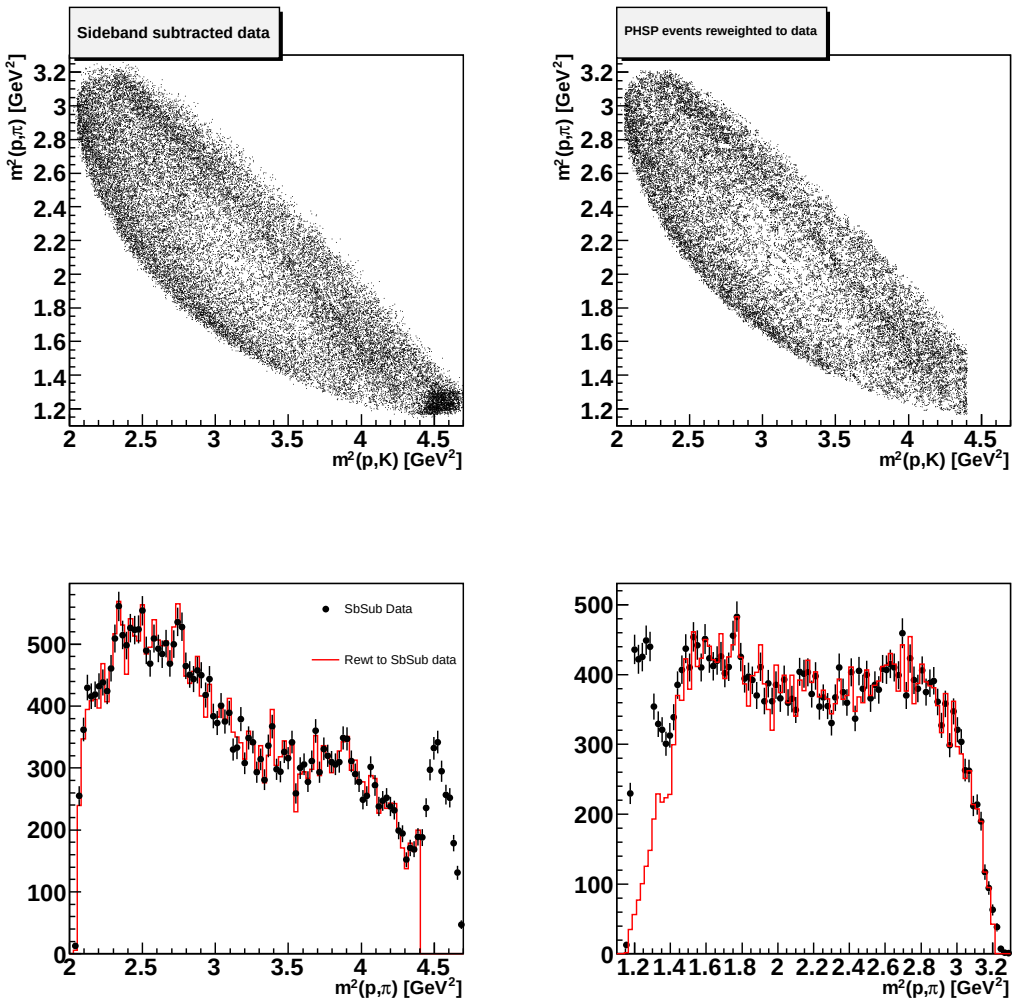

Figure D.3: Comparison of Λ_c^+ decay Dalitz plots of sideband subtracted data (top left) and non-resonant decays reweighted to data (top right). Also shown in the bottom plots are projections along x (bottom left) and y (bottom right) axes. Note that the bump in the data Dalitz plot on the bottom-right corner is left out from the reweighting procedure.

Bibliography

[1] F. Azfar *et.al.* (The CDF B_s mixing working group), "B mesons lifetime determination in fully hadronic decays", CDF Note 7386.

[2] W. S. C. Williams (1991) *Nuclear and Particle Physics*.

[3] David Griffiths (1987) *Introduction to Elementary Particles*.

[4] Donald H. Perkins (2000) *Introduction to High Energy Physics*.

[5] F. Halzen & A. D. Martin (1984) *Quarks and Leptons*

[6] I. I. Y. Bigi, M. A. Schifman and N. Uraltsev, Ann.Rev.Nucl.Part.Sci. **47** (1997) 591.

[7] C. Tarantino *et al.*, arXiv:hep-ph/**0310241**

[8] W. M. Yao *et al.*, J. Phys. G **33**, 1(2006).

[9] A. Abulencia, *et al.* (hep-ex/0609021)

[10] C. L. Cowan *et al.*, Science 20 July 1956: Vol. 124. no. 3212, pp. 103 - 104

BIBLIOGRAPHY

[11] F. Gabbiani *et al.*, arXiv:hep-ph/**0303235v3**

[12] I. I. Bigi, The lifetimes of Heavy Flavour Hadrons - A Case Study in Quark-Hadron Duality, UND-HEP-99-BIG 07 (1999).

[13] I. I. Bigi, Lifetimes of Heavy-Flavour Hadrons - Whence and Whither, UND-HEP-95-BIG 06 (1995).

[14] I. I. Bigi, and P. J. Dornan, Lifetimes of Charm and Beauty Hadrons, UND-HEP-96-BIG 02 (1996).

[15] K. Anikeev *et. al.*, "B Physics at the Tevatron: Run II and Beyond", hep-ph/0201071.

[16] I. I. Bigi, Purdue University, Personal communication, July 2008.

[17] C. Amsler *et. al.*, Physics Letters B667, 1 (2008).

[18]] The CDF Collaboration, "Measurement of B Hadron Relative Fragmentation Fractions," CDF Note 8140 (2006). To be submitted to Phys. Rev. D. Available at `http://www-cdf.fnal.gov/physics/new/bottom/060216.blessed-fqFractions/`.

[19] Fermilab Beams Division, Run II Handbook, `http://www-bd.fnal.gov/lug/runII_handbook/RunII_index.html`.

[20] The CDF II Collaboration, "The CDF II Detector Technical Design Report", FERMILAB-Pub-96/390-E CDF.

BIBLIOGRAPHY

[21] Accelerators - Fermilab's Chain of Accelerators, http://www.fnal.gov/pub/inquiring/physics/accelerators/chainaccel.html

[22] H. Wenzel, "Tracking in the SVX", CDF Note 1790 (1992).

[23] S. Menzemer, "TrackingKal - A Tracking and Alignment Software Package for the CDF II Silicon Detector" CDF Note 5968 Rev 4. (2003).

[24] M. Campanelli and E. Gerchtein, "Calibration of the Momentum Scale for Kalman Fitter Using J/ψ Events," CDF Note 6905 (2004).

[25] A. Belloni *et. al.*, "Scale Factors for Proper Time Uncertainties at CDF," CDF Note 7944 (2005).

[26] "Kernel Estimation in High-Energy Physics", K. Cranmer, Comput.Phys.Commun. 136 (2001) 198-207, hep-ex/0011057

[27] D.Litvinsev *et.al.*, "Measurement of the Λ_b^0 p_T spectrum in the TTT data using fully reconstructed decay $\Lambda_b^0 \to \Lambda_c^+ \pi^-$" CDF Note 8156.

[28] Good Run List Version 13: http://www-cdf.fnal.gov/internal/dqm/goodrun/v13/goodv13.html

[29] A. Cerri *et. al.*, "Measurement of B^0 Branching Fractions Using Combined Mass and dE/dx Fits", CDF Note 8705.

[30] A. Cerri *et. al.*, "Determination of B^0 and B^+ Lifetimes in Hadronic Decays Using Partially and Fully Reconstructed Modes", CDF Note 8778.

BIBLIOGRAPHY

[31] A. Cerri *et. al.*, "Measurement of the B_s Lifetime in Hadronic Decays Using Partially and Fully Reconstructed Modes", CDF Note 9140.

[32] I.Gorelov *et.al.*, "Λ_b Data Sample and Mass Fit with Two Displaced Track Trigger Using 1 fb^{-1}", CDF Note 8395.

[33] T. Sjostrand, P. Eden, C. Friberg, L. Lonnblad, G. Miu, S. Mrenna, and E. Norrbin, "High-energy-physics event generation with PYTHIA 6.1," Comput. Phys. Commun. 135, 238 (2001) [arXiv:hep-ph/0010017].

[34] P. Sphicas, "A $b\bar{b}$ Monte Carlo Generator," CDF Note 2655 (1994). K. Anikeev, C. Paus, and P. Murat, "Description of Bgenerator II: Bgenerator in its Run II Incarnation," CDF Note 5092 (1999).

[35] S.Gromoll, Ch.Paus, "A Heavy Quark Generator", CDF Note 5985 (2002).

[36] W. Bell, J. Pablo Fernandez, L. Flores, F. Wuerthwein, and R. J. Tesarek, "User Guide for EvtGen CDF," CDF Note 5618 (2001). J. Beringer et al., "User Guide for the New EvtGen CDF," CDF Note 7917 (2005).

[37] J. Lewis and P. Avery, "CLEOMC: The CDF Interface to the CLEO Monte Carlo (QQ)," CDF Note 2724 (1994).

[38] S. Agostinelli *et. al.* [GEANT4 Collaboration], "GEANT4A Simulation Toolkit," Nucl. Instrum. Meth. A 506, 250-303 (2003). R. Brun and F. Carminati, GEANT

Detector Description and Simulation Tool, CERN Program Library Long Write-up W5013; see also http://wwwasd.web.cern.ch/wwwasd/geant/.

[39] Shin-Shan Yu, *et al.* , "Ratio of $\mathcal{B}(\Lambda_b^0 \to \Lambda_c^+ \mu^- \overline{\nu}_\mu)$ to $\mathcal{B}(\Lambda_b^0 \to \Lambda_c^+ \pi^-)$ in the two track trigger," CDF/PHYS/BOTTOM/CDFR/7559 (2005).

[40] M.Martin, *et al.*, "Estimation of Λ_b^0 Exclusive Non-Leptonic Branching Ratios", CDF/PUB/BOTTOM/PUBLIC/7765 (2005), revision #2.

[41] "The Universal Finder", http://cdfcodebrowser.fnal.gov/CdfCode/source/Sin2BetaMods

[42] "JpsiXMods", http://cdfcodebrowser.fnal.gov/CdfCode/source/JpsiXMods

[43] "BStntuples", http://www-cdf.fnal.gov/htbin/twiki/bin/view/BStntuples/DataSetsSpring2006

[44] Yi Le *et.al.*, "Observation of Λ_b^0 to $\Lambda_c^+ \pi^-$ and the measurement of $f_{\Lambda_b}/f_d)(BR(\Lambda_b)/BR(B^0))$" CDF Note 6396

[45] Yi Le *et.al.*, "Observation of Λ_b^0 to $\Lambda_c^+ \pi^-$ and the measurement of $f_{\Lambda_b}/f_d)(BR(\Lambda_b)/BR(B^0))$" CDF Note 6396, p39-40, and the Refs. 13 and 14 therein.

[46] W. Verkerke, D. Kirkby, "RooFit Users Manual v2.07", http://roofit.sourceforge.net/docs/RooFit_Users_Manual_2.07-29.pdf.

[47] S. De Cecco *et.al.*, "A Measurement of the Relative Branching Fractions $\Gamma(D^0 \to K^+K^-)/\Gamma(D^0 \to K\pi)$ and $\Gamma(D^0 \to \pi^+\pi^-)/\Gamma(D^0 \to K\pi)$.", CDF Note 6018, Section 2.3.

[48] W. M. Yao *et al.*, J. Phys. G **33**, 1(2006) and 2007 partial update for the 2008 edition.

[49] E. M. Aitala *et. al.*, "Multidimensional Resonance Analysis of $\Lambda_c^+ \to pK^-\pi^+$", Phys.Lett. **B471** (2000) 449-459 and arXiv:hep-ex/**9912003v1**.

Vita

Jonathan Reid Mumford [redacted]. He enrolled as an undergraduate at the University of Utah in Salt Lake City, UT where he graduated with an Honors Bachelor of Science degree in Physics in 2000. As an undergraduate, he worked as a member of the High Resolution Fly's Eye Cosmic Ray experiment.

Reid then attended The Johns Hopkins University, in Baltimore, MD, as a graduate student in experimental high-energy particle physics. He worked as a teaching assistant for two years and was awarded the Rowland Prize for Innovation and Excellence in Teaching in 2001. In 2002 he moved to Illinois to conduct research at the Collider Detector at Fermilab. Reid was awarded a Master of Art degree in Physics in 2004. Reid completed the requirements for a Doctor of Philosophy degree in Physics in 2008.